Accurate RTA-Based Non-Quasi-Static Compact MOSFET Model for RF and Mixed-Signal Simulations

by

Zeqin Zhu

A Dissertation Presented in Partial Fulfillment
of the Requirements for the Degree
Doctor of Philosophy

Approved December 2011 by the
Graduate Supervisory Committee:

Gennady Gildenblat, Chair
Bertan Bakkaloglu
Hugh Barnaby
Colin C. McAndrew

ARIZONA STATE UNIVERSITY

May 2012

ABSTRACT

The non-quasi-static (NQS) description of device behavior is useful in fast switching and high frequency circuit applications. Hence, it is necessary to develop a fast and accurate compact NQS model for both large-signal and small-signal simulations.

A new relaxation-time-approximation based NQS MOSFET model, consistent between transient and small-signal simulations, has been developed for surface-potential-based MOSFET compact models. The new model is valid for all regions of operation and is compatible with, and at low frequencies recovers, the quasi-static (QS) description of the MOSFET. The model is implemented in two widely used circuit simulators and tested for speed and convergence. It is verified by comparison with technology computer aided design (TCAD) simulations and experimental data, and by application of a recently developed benchmark test for NQS MOSFET models. In addition, a new and simple technique to characterize NQS and gate resistance, R_{gate}, MOS model parameters from measured data has been presented.

In the process of experimental model verification, the effects of bulk resistance on MOSFET characteristics is investigated both theoretically and experimentally to separate it from the NQS effects.

TO MY GRANDPARENTS, PARENTS AND WIFE

ACKNOWLEDGMENTS

I would like to express my deepest gratitude to my advisor, Professor Gennady Gildenblat, for the guidance, financial support, and assistance in the generation of research topics during my Ph.D. study. The conception, maintenance, and completion of this research is all attributed to his continuous dedication to research and education.

Special thanks are also due to Dr. Colin C. McAndrew, whose technical support and guidance were crucial to the completion of the research. I would also like to thank Professor Bertan Bakkaloglu, Professor Hugh Barnaby and Professor Bahar Jalali-Farahani in the electrical engineering department for their constant encouragements and helpful discussions during the course of this work.

Many of my coworkers have contributed to the completion of this work. In particular, Dr. Weimin Wu (now with Texas Instruments) and Dr. Qina Zhou (now with GTC) shared insightful thoughts and discussions, Dr. Xin Li (now with Global Foundries) provided coding and model extraction support, and Wei Yao and Gajanan Dessai also joined many technical discussions regarding the compact MOSFET modeling.

I am also indebted to Dr. James Victory, Dr. Samir Chaudhry, and Juan Cordovez who have been my supervisors at TowerJazz. Their guidance and support were essential for me to complete the two summer internships at TowerJazz. I am also thankful to Dr. Gert-Jan Smit, Dr. Andries J. Scholten, and Dr. Dirk B. M. Klaassen for their insightful discussions and help on the NQS work and other collaborating projects. I am particulary grateful to Dr. Geoffrey Coram for numer-

ous support in verilog-A code checking and Dr. Ik-Sung Lim, Dr. Li Dong, Zhixin Yan, Dr. Jie Zheng, and Dr. David Quon for providing the experimental data of RF CMOS processes. Additional thanks go to James Laux for numerous technical support on the EDA tools of Connection One at ASU.

Last but certainly not the least, my deepest thanks are owed to my family members, especially to my wife, Ying Li who has always loved, trusted, and supported me. I also would like to thank my parents, Wensheng Zhu and Jufeng Chen, for love and support.

TABLE OF CONTENTS

Page

LIST OF TABLES vii

LIST OF FIGURES viii

CHAPTER

1 INTRODUCTION 1

1.1. NQS Compact MOSFET Models 1

1.2. Existing Large-Signal NQS Models 2

1.2.1. BSIM3/BSIM4-NQS 2

1.2.2. HiSIM-NQS 4

1.2.3. Channel Segmentation Method 5

1.2.4. SP-NQS and PSP-NQS 6

1.3. Existing Small-Signal NQS Models 6

1.3.1. Small-Signal Model in [1] 7

1.3.2. Small-Signal Models in [2, 3] 10

1.3.3. Small-Signal Model in [4] 10

1.4. Present Work 11

1.5. Organization of This Thesis 13

2 THE NEW RTA-BASED NQS MOSFET MODEL 14

2.1. Terminal Charges 14

2.2. Terminal Currents 18

2.3. Small-Geometry Effects, Parasitics, and Noise 19

3 MODEL VALIDATION 20

3.1. Model Validation with TCAD 20

CHAPTER Page

3.2. Model Validation with Experimental Data 29

3.3. Parameter Extraction for RTA-Based NQS MOSFET Models . . 54

3.3.1. Analysis 54

3.3.2. Extraction Algorithm 55

3.3.3. Experimental Results 56

4 SMALL-SIGNAL MODEL 59

4.1. Small-Signal RTA-Based NQS Model 59

4.1.1. Model Formulation and Terminal Charges 59

4.1.2. y-Parameters 62

4.1.3. Lowest-Order Corrections to the QS Small-Signal Model 77

4.2. Benchmark Test for $V_{\mathrm{DS}} = 0$ in Strong Inversion Regime 78

5 BULK RESISTANCE EFFECT ON MOSFET GATE CAPACITANCE . 85

5.1. Introduction 85

5.2. TCAD and PSP-RTA-NQS Modeling 86

5.3. Analytic Expression for C_{gg} in the Presence of Bulk Resistance . 93

5.4. Experimental Data 96

5.5. Summary 99

6 CONCLUSIONS 102

6.1. Conclusion 102

REFERENCES 103

APPENDIX A ADDITIONAL RESULTS FOR MODEL VALIDATION . . 117

A.1. $V_{\mathrm{DS}} = 0$ V 118

A.2. $V_{\mathrm{DS}} = -0.3$ V 126

LIST OF TABLES

Table Page

2.1. Summary of Evaluation of Terminal Charges in PSP-RTA-NQS 18

4.1. Small-Signal Terminal Charges 62

LIST OF FIGURES

Figure Page

1.1. Schematic for channel segmentation method 5

3.1. Drain and source terminal currents for v_{GS} switching from 0 to 3 V at 10^{10} V/s; V_{DS}=3 V and V_{BS}=0. 21

3.2. Gate and bulk terminal currents for v_{GS} switching from 0 to 3 V at 10^{10} V/s, V_{DS}=3 V. 22

3.3. Gate and bulk terminal currents for v_{GS} switching from -3 to 3 V at 2×10^{10} V/s; V_{DS}=3 V. 23

3.4. Gate and bulk terminal currents for v_{GS} switching from 0 to 5 V at 5×10^{11} V/s; V_{DS}=5 V. 24

3.5. C_{gg} for f=0, $0.5f_{\mathrm{T}}$, $1.0f_{\mathrm{T}}$, $1.5f_{\mathrm{T}}$ and $2.0f_{\mathrm{T}}$ (top to bottom), where f_{T}=1.6 GHz; V_{DS}=0.5 V. The weak frequency dependence in accumulation is completely due to the bulk resistance effect (extracted R_{bulk} = 116.8 Ω from TCAD data) [5]. 25

3.6. C_{gs} for f=0, $0.5f_{\mathrm{T}}$, $1.0f_{\mathrm{T}}$, $1.5f_{\mathrm{T}}$ and $2.0f_{\mathrm{T}}$ (top to bottom), where f_{T} = 1.6 GHz; V_{DS}=0.5 V. 26

3.7. C_{bg} for f=0, $3.1f_{\mathrm{T}}$, $6.3f_{\mathrm{T}}$, $12.5f_{\mathrm{T}}$, $18.8f_{\mathrm{T}}$, $25f_{\mathrm{T}}$ and $31f_{\mathrm{T}}$ (top to bottom in accumulation region, bottom to top in strong inversion inset), where f_{T}=1.6 GHz; V_{DS}=0.5 V. The significant decrease in the accumulation is completely due to the bulk resistance effect (extracted R_{bulk} = 116.8 Ω from TCAD data) [5]. 27

3.8. C_{ds} from partitioning based on (2.1) (solid lines) and (2.2) (dot-dash lines), f_{T} = 1.6 GHz; V_{DS}=0. 28

Figure Page

3.9. Test device with GSG probe pad configuration. Courtesy of Freescale semiconductors, presented with permission. 29

3.10. Comparison of model and measured data for a PMOS g_{gg} when V_{DS} = -0.6 V. Frequencies are 0.1, 0.5, 1 and 2 GHz where $f_{\mathrm{T}} = 0.71$ GHz. L = 1.2 μm, W = 10 μm. 30

3.11. Comparison of model and measured data for a PMOS C_{gg} when V_{DS} = -0.6 V. Frequencies are 0.1, 0.5, 1 and 2 GHz where $f_{\mathrm{T}} = 0.71$ GHz. L = 1.2 μm, W = 10 μm. 31

3.12. Comparison of model and measured data for a PMOS g_{gd} when V_{DS} = -0.6 V. Frequencies are 0.1, 0.5, 1 and 2 GHz where $f_{\mathrm{T}} = 0.71$ GHz. L = 1.2 μm, W = 10 μm. 32

3.13. Comparison of model and measured data for a PMOS C_{gd} when V_{DS} = -0.6 V. Frequencies are 0.1, 0.5, 1 and 2 GHz where $f_{\mathrm{T}} = 0.71$ GHz. L = 1.2 μm, W = 10 μm. 33

3.14. Comparison of model and measured data for a PMOS g_{dg} when V_{DS} = -0.6 V. Frequencies are 0.1, 0.5, 1 and 2 GHz where $f_{\mathrm{T}} = 0.71$ GHz. L = 1.2 μm, W = 10 μm. 34

3.15. Comparison of model and measured data for a PMOS C_{dg} when V_{DS} = -0.6 V. Frequencies are 0.1, 0.5, 1 and 2 GHz where $f_{\mathrm{T}} = 0.71$ GHz. L = 1.2 μm, W = 10 μm. 35

3.16. Comparison of model and measured data for a PMOS g_{dd} when V_{DS} = -0.6 V. Frequencies are 0.1, 0.5, 1 and 2 GHz where $f_{\mathrm{T}} = 0.71$ GHz. L = 1.2 μm, W = 10 μm. 36

Figure Page

3.17. Comparison of model and measured data for a PMOS C_{dd} when V_{DS} = -0.6 V. Frequencies are 0.1, 0.5, 1 and 2 GHz where $f_{\mathrm{T}} = 0.71$ GHz. L = 1.2 μm, W = 10 μm. 37

3.18. Comparison of model and measured data for a PMOS g_{gg} when V_{GS} = -0.8 V. Frequencies are 0.1, 0.5, 1 and 2 GHz where $f_{\mathrm{T}} = 0.71$ GHz. L = 1.2 μm, W = 10 μm. 38

3.19. Comparison of model and measured data for a PMOS C_{gg} when V_{GS} = -0.8 V. Frequencies are 0.1, 0.5, 1 and 2 GHz where $f_{\mathrm{T}} = 0.71$ GHz. L = 1.2 μm, W = 10 μm. 39

3.20. Comparison of model and measured data for a PMOS g_{gd} when V_{GS} = -0.8 V. Frequencies are 0.1, 0.5, 1 and 2 GHz where $f_{\mathrm{T}} = 0.71$ GHz. L = 1.2 μm, W = 10 μm. 40

3.21. Comparison of model and measured data for a PMOS C_{gd} when V_{GS} = -0.8 V. Frequencies are 0.1, 0.5, 1 and 2 GHz where $f_{\mathrm{T}} = 0.71$ GHz. L = 1.2 μm, W = 10 μm. 41

3.22. Comparison of model and measured data for a PMOS g_{dg} when V_{GS} = -0.8 V. Frequencies are 0.1, 0.5, 1 and 2 GHz where $f_{\mathrm{T}} = 0.71$ GHz. L = 1.2 μm, W = 10 μm. 42

3.23. Comparison of model and measured data for a PMOS C_{dg} when V_{GS} = -0.8 V. Frequencies are 0.1, 0.5, 1 and 2 GHz where $f_{\mathrm{T}} = 0.71$ GHz. L = 1.2 μm, W = 10 μm. 43

Figure Page

3.24. Comparison of model and measured data for a PMOS g_{dd} when V_{GS} = -0.8 V. Frequencies are 0.1, 0.5, 1 and 2 GHz where $f_{\mathrm{T}} = 0.71$ GHz. L = 1.2 μm, W = 10 μm. 44

3.25. Comparison of model and measured data for a PMOS C_{dd} when V_{GS} = -0.8 V. Frequencies are 0.1, 0.5, 1 and 2 GHz where $f_{\mathrm{T}} = 0.71$ GHz. L = 1.2 μm, W = 10 μm. 45

3.26. Comparison of model and measured data for a PMOS g_{gg} when V_{GS} = -0.9 V. Frequencies are 0.1, 0.5, 1 and 2 GHz where $f_{\mathrm{T}} = 0.71$ GHz. L = 1.2 μm, W = 10 μm. 46

3.27. Comparison of model and measured data for a PMOS C_{gg} when V_{GS} = -0.9 V. Frequencies are 0.1, 0.5, 1 and 2 GHz where $f_{\mathrm{T}} = 0.71$ GHz. L = 1.2 μm, W = 10 μm. 47

3.28. Comparison of model and measured data for a PMOS g_{gd} when V_{GS} = -0.9 V. Frequencies are 0.1, 0.5, 1 and 2 GHz where $f_{\mathrm{T}} = 0.71$ GHz. L = 1.2 μm, W = 10 μm. 48

3.29. Comparison of model and measured data for a PMOS C_{gd} when V_{GS} = -0.9 V. Frequencies are 0.1, 0.5, 1 and 2 GHz where $f_{\mathrm{T}} = 0.71$ GHz. L = 1.2 μm, W = 10 μm. 49

3.30. Comparison of model and measured data for a PMOS g_{dg} when V_{GS} = -0.9 V. Frequencies are 0.1, 0.5, 1 and 2 GHz where $f_{\mathrm{T}} = 0.71$ GHz. L = 1.2 μm, W = 10 μm. 50

Figure Page

3.31. Comparison of model and measured data for a PMOS C_{dg} when V_{GS} = -0.9 V. Frequencies are 0.1, 0.5, 1 and 2 GHz where $f_{\mathrm{T}} = 0.71$ GHz. L = 1.2 μm, W = 10 μm. 51

3.32. Comparison of model and measured data for a PMOS g_{dd} when V_{GS} = -0.9 V. Frequencies are 0.1, 0.5, 1 and 2 GHz where $f_{\mathrm{T}} = 0.71$ GHz. L = 1.2 μm, W = 10 μm. 52

3.33. Comparison of model and measured data for a PMOS C_{dd} when V_{GS} = -0.9 V. Frequencies are 0.1, 0.5, 1 and 2 GHz where $f_{\mathrm{T}} = 0.71$ GHz. L = 1.2 μm, W = 10 μm. 53

3.34. Extracted and modeled $C_{\mathrm{dg}}^{(0)}/C_{\mathrm{dg}} - 1$, pMOS transistor; $V_{\mathrm{DS}} = 0$, V_{SG}=1.5V, f=0.1, 0.5, 1.0, 2.0GHz. 57

3.35. Extracted and modeled effective NQS relaxation times, pMOS transistor; $V_{\mathrm{DS}} = 0$, V_{SG}=0.6 to 1.5V by 0.1V top right to bottom left. 58

4.1. Intrinsic MOSFET with dc biases and small-signal voltages. 59

5.1. TCAD and PSP-QS models of normalized C_{gg}, with $R_{\mathrm{bulk}} = 0$ for PSP-QS. W/L = 1.0μm/5.0μm, t_{ox} = 2.0nm, $N_{\mathrm{bulk}} = 3.0 \times 10^{17}\mathrm{cm}^{-3}$ (p-type), frequencies are 0, 0.25f_{T}, 0.5f_{T}, 0.75f_{T}, f_{T}, 1.25f_{T} and 1.5f_{T}(top to bottom). Here f_{T} = 1.6 GHz and substrate thickness t_{bulk} = 30 μm. 87

5.2. Effect of accounting for NQS behavior – TCAD and PSP-RTA-NQS models of normalized C_{gg}, with $R_{\mathrm{bulk}} = 0$ for PSP-RTA-NQS. Same device parameters and frequencies as Fig. 5.1. 88

5.3. $C_{\mathrm{gg}}^{(0)}/C_{\mathrm{gg}}$ vs. ω^2 from TCAD simulations at $V_{\mathrm{GS}} = -2$. 90

Figure Page

5.4. Effect of accounting for both R_{bulk} and NQS behavior – TCAD and PSP-RTA-NQS models of C_{gg} with $R_{\text{bulk}} = 2.2$ kΩ included for PSP-RTA-NQS. Same device parameters and frequencies as Fig. 5.1. 91

5.5. Effect of accounting for R_{bulk} – TCAD and PSP-QS models of C_{gg} with $R_{\text{bulk}} = 2.2$ kΩ included for PSP-QS. Same device parameters and frequencies as Fig. 5.1. 92

5.6. Effect of variation of bulk thickness, $f = f_{\text{T}} = 1.6$ GHz. PSP-RTA-NQS model parameter $R_{\text{bulk}} = 2/3R_{\text{bulk0}}$, R_{bulk0} and $4/3R_{\text{bulk0}}$ for $t_{\text{bulk}} = 2/3t_{\text{bulk0}}$, t_{bulk0} and $4/3t_{\text{bulk0}}$, respectively. Here $R_{\text{bulk0}} = 2.2$ kΩ and $t_{\text{bulk0}} = 30$ μm. 93

5.7. TCAD and analytic models, R_{bulk} effect only (no NQS) in the analytic model. Same device parameters and frequencies as Fig. 5.1. 97

5.8. Measured PMOS data and PSP-RTA-NQS model with both R_{bulk} and R_{gate} included. $W/L = 10.0\mu\text{m}/1.2\mu\text{m}$, frequencies are 5, 10, 20, 30, and 50 GHz (top to bottom). $f_{\text{T}} = 0.71$GHz. 98

5.9. Effect of not accounting for R_{gate} – measured PMOS data and PSP-RTA-NQS model with only R_{bulk} included. Same device and frequencies as Fig. 5.8. 99

5.10. Effect of not accounting for R_{bulk} – measured PMOS data and PSP-RTA-NQS model with only R_{gate} included. Same device and frequencies as Fig. 5.8. 100

Figure Page

5.11. Effect of not accounting for NQS effects – measured PMOS data and PSP-QS model with R_{bulk} and R_{gate} included. Same device as Fig. 5.8. In addition to the same frequencies as in Fig. 5.8, the curve for $f \ll f_{\text{T}}$ is included as well. 101

A.1. Comparison of model and measured data for a PMOS g_{gg} when $V_{\text{DS}} =$ 0 V. Frequencies are 0.1, 0.5, 1 and 2 GHz where $f_{\text{T}} = 0.71$ GHz. $L =$ 1.2 μm, $W = 10$ μm. 118

A.2. Comparison of model and measured data for a PMOS C_{gg} when $V_{\text{DS}} =$ 0 V. Frequencies are 0.1, 0.5, 1 and 2 GHz where $f_{\text{T}} = 0.71$ GHz. $L =$ 1.2 μm, $W = 10$ μm. 119

A.3. Comparison of model and measured data for a PMOS g_{gd} when $V_{\text{DS}} =$ 0 V. Frequencies are 0.1, 0.5, 1 and 2 GHz where $f_{\text{T}} = 0.71$ GHz. $L =$ 1.2 μm, $W = 10$ μm. 120

A.4. Comparison of model and measured data for a PMOS C_{gd} when $V_{\text{DS}} =$ 0 V. Frequencies are 0.1, 0.5, 1 and 2 GHz where $f_{\text{T}} = 0.71$ GHz. $L =$ 1.2 μm, $W = 10$ μm. 121

A.5. Comparison of model and measured data for a PMOS g_{dg} when $V_{\text{DS}} =$ 0 V. Frequencies are 0.1, 0.5, 1 and 2 GHz where $f_{\text{T}} = 0.71$ GHz. $L =$ 1.2 μm, $W = 10$ μm. 122

A.6. Comparison of model and measured data for a PMOS C_{dg} when $V_{\text{DS}} =$ 0 V. Frequencies are 0.1, 0.5, 1 and 2 GHz where $f_{\text{T}} = 0.71$ GHz. $L =$ 1.2 μm, $W = 10$ μm. 123

Figure Page

A.7. Comparison of model and measured data for a PMOS g_{dd} when V_{DS} = 0 V. Frequencies are 0.1, 0.5, 1 and 2 GHz where $f_{\mathrm{T}} = 0.71$ GHz. L = 1.2 μm, W = 10 μm. 124

A.8. Comparison of model and measured data for a PMOS C_{dd} when V_{DS} = 0 V. Frequencies are 0.1, 0.5, 1 and 2 GHz where $f_{\mathrm{T}} = 0.71$ GHz. L = 1.2 μm, W = 10 μm. 125

A.9. Comparison of model and measured data for a PMOS g_{gg} when V_{DS} = -0.3 V. Frequencies are 0.1, 0.5, 1 and 2 GHz where $f_{\mathrm{T}} = 0.71$ GHz. L = 1.2 μm, W = 10 μm. 126

A.10. Comparison of model and measured data for a PMOS C_{gg} when V_{DS} = -0.3 V. Frequencies are 0.1, 0.5, 1 and 2 GHz where $f_{\mathrm{T}} = 0.71$ GHz. L = 1.2 μm, W = 10 μm. 127

A.11. Comparison of model and measured data for a PMOS g_{gd} when V_{DS} = -0.3 V. Frequencies are 0.1, 0.5, 1 and 2 GHz where $f_{\mathrm{T}} = 0.71$ GHz. L = 1.2 μm, W = 10 μm. 128

A.12. Comparison of model and measured data for a PMOS C_{gd} when V_{DS} = -0.3 V. Frequencies are 0.1, 0.5, 1 and 2 GHz where $f_{\mathrm{T}} = 0.71$ GHz. L = 1.2 μm, W = 10 μm. 129

A.13. Comparison of model and measured data for a PMOS g_{dg} when V_{DS} = -0.3 V. Frequencies are 0.1, 0.5, 1 and 2 GHz where $f_{\mathrm{T}} = 0.71$ GHz. L = 1.2 μm, W = 10 μm. 130

Figure Page

A.14. Comparison of model and measured data for a PMOS C_{dg} when V_{DS} = -0.3 V. Frequencies are 0.1, 0.5, 1 and 2 GHz where $f_{\mathrm{T}} = 0.71$ GHz. L = 1.2 μm, W = 10 μm. 131

A.15. Comparison of model and measured data for a PMOS g_{dd} when V_{DS} = -0.3 V. Frequencies are 0.1, 0.5, 1 and 2 GHz where $f_{\mathrm{T}} = 0.71$ GHz. L = 1.2 μm, W = 10 μm. 132

A.16. Comparison of model and measured data for a PMOS C_{dd} when V_{DS} = -0.3 V. Frequencies are 0.1, 0.5, 1 and 2 GHz where $f_{\mathrm{T}} = 0.71$ GHz. L = 1.2 μm, W = 10 μm. 133

CHAPTER 1

Introduction

1.1. NQS Compact MOSFET Models

The state-of-the-art design of RF and mixed-signal CMOS circuits can require inclusion of the non-quasi-static (NQS) effects, such as the finite channel transit time [1]. Various compact formulations of NQS models have been reported [3, 4, 6–51]. Among them, [25, 29, 30] are threshold-voltage-based (V_{T}-based) models, [3, 44, 50] are inversion-charge-based (q_{I}-based) models, and [4,31–34,47] are surface-potential-based (ψ_{S}-based) models. To be useful in a generic circuit simulator, NQS models need to be large-signal and not rely on the small-signal approximation. Inclusion of NQS effects in a large-signal formulation is a difficult task which when performed rigorously, and increases both the model complexity and the execution time. For example, two accurate large-signal NQS ψ_{s}-based compact models are based on the channel segmentation [31] and spline-collocation-method [32, 33] and are both significantly more complex than the corresponding QS models [52, 53]. A popular simplification of the NQS model is the use of the relaxation-time-approximation (RTA) which reduces the simulation time and improves convergence at the price of the reduced accuracy, especially at high frequencies. These models are described in [29, 34, 54–56] with some additional insights found in [57]. In a different form, RTA also appears in a comprehensive varactor model where it is used to describe the inertia in the formulation of the inversion layer [58–61]. In the development of RTA NQS models, it is common to assume that RTA applies to all terminal charges, including the bulk charge. As shown in [62], this assumption makes RTA models

fail a benchmark test specific for NQS models. The shortcomings of this assumption from the experimental point of view are discussed in [5].

1.2. Existing Large-Signal NQS Models

1.2.1. BSIM3/BSIM4-NQS

BSIM3 and BSIM4 are V_{T}-based models [57, 63–66]. Berkeley's LEVEL1, LEVEL2, and LEVEL3; BSIM1, BSIM2, BSIM3, and BSIM4; and NXP's MM9 all belong to this category. The models of this type are formulated directly in terms of figures of merits in mainstream circuit design theory (e.g., V_{T}, subthreshold slope, etc). The V_{T}-based model is essentially a regional model that relies on a piece-wise description of the strong and weak inversion regimes of the device operation.

In the BSIM3 and BSIM4 NQS models, the MOSFET is divided into a few sub-MOSFETs of smaller channel length. The RC network representing the distributed channel is now replaced by an Elmore lumped equivalent circuit that preserves the lowest frequency pole of the distributed channel [29]. The Elmore resistance is given by:

$$R_{\mathrm{ELM}} = \frac{L^2}{P_{\mathrm{ELM}} \cdot \mu \cdot q_{\mathrm{I}}^{(0)}} \tag{1.1}$$

where μ is effective channel mobility, L is channel length, P_{ELM} is a fitting parameter, the total inversion $q_{\mathrm{I}} = C_{\mathrm{ox}} (V_{\mathrm{GS}} - V_{\mathrm{T}})$ is adopted in the V_{T}-based model which is only valid for the strong inversion region, and C_{ox} is the oxide capacitance. The superscript "(0)" denotes the QS value of the corresponding variable and SI units and physical signs are used throughout. The value of P_{ELM} is extracted by matching the time response of the fast switching device operation.

The RTA models in BSIM3 and BSIM4 are essentially the same [29, 65, 66] [1]:

$$\frac{dq_{\mathrm{T}}}{dt} = F_{\mathrm{T}} \cdot \frac{q_{\mathrm{I}}^{(0)} - q_{\mathrm{I}}}{\tau}, \quad \mathrm{T} \in \{\mathrm{D}, \mathrm{G}, \mathrm{S}\} \tag{1.2}$$

where F_{D}, F_{G}, and F_{S} are the NQS channel charge partitioning factors for terminals D, G, and S, respectively:

$$F_{\mathrm{S}} + F_{\mathrm{D}} = 1 \tag{1.3}$$

$$F_{\mathrm{G}} = -1 \tag{1.4}$$

Both BSIM3 and BSIM4 large signal NQS models use the quasi-static value for the bulk charge [65, 66].

The relaxation time, τ, is slightly different for BSIM3 and BSIM4. In BSIM3, for a unified expression valid for both strong and weak inversion modes of operation, τ is given as a combination of the diffusion and drift mechanisms:

$$\frac{1}{\tau} = \frac{1}{\tau_{\mathrm{diff}}} + \frac{1}{\tau_{\mathrm{dr}}} \tag{1.5}$$

where

$$\tau_{\mathrm{diff}} = \frac{L^2}{16 \cdot \mu \cdot \phi_{\mathrm{t}}} \tag{1.6}$$

ϕ_{t} is the thermal voltage, and

$$\tau_{\mathrm{dr}} = R_{\mathrm{ELM}} \cdot C_{\mathrm{ox}} = \frac{L^2 \cdot C_{\mathrm{ox}}}{P_{\mathrm{ELM}} \cdot \mu \cdot q_{\mathrm{I}}^{(0)}} \tag{1.7}$$

In BSIM4, τ is given by

$$\frac{1}{\tau} = \frac{1}{R_{\mathrm{ii}} C_{\mathrm{ox}}} \tag{1.8}$$

[1] cf. Eq. (8.1.4b) of [66]

where the inverse of the intrinsic input resistance

$$\frac{1}{R_{\mathrm{ii}}} = \mathrm{XRCRG1} \cdot \left(\frac{I_{\mathrm{DS}}}{V_{\mathrm{deff}}} + \mathrm{XRCRG2} \cdot \frac{\mu \phi_{\mathrm{t}} C_{\mathrm{ox}}}{L^2} \right) \tag{1.9}$$

Here, XRCRG1 and XRCRG2 are model parameters and V_{deff} is the effective drain voltage.

1.2.2. HiSIM-NQS

HiSIM [56, 67, 68] is a ψ_{S}-based model. In fact, HiSIM NQS uses [34]

$$q_{\mathrm{I}}(t_{\mathrm{n}}) = q_{\mathrm{I}}(t_{\mathrm{n-1}}) + \frac{\Delta t}{\tau} \left[q_{\mathrm{I}}^{(0)}(t_{\mathrm{n}}) - q_{\mathrm{I}}(t_{\mathrm{n-1}}) \right] \tag{1.10}$$

$$q_{\mathrm{B}}(t_{\mathrm{n}}) = q_{\mathrm{B}}(t_{\mathrm{n-1}}) + \frac{\Delta t}{\tau_{\mathrm{B}}} \left[q_{\mathrm{B}}^{(0)}(t_{\mathrm{n}}) - q_{\mathrm{B}}(t_{\mathrm{n-1}}) \right] \tag{1.11}$$

where τ and τ_{B} are the relaxation time for inversion and bulk charges, respectively. After the inversion charge is known, source and drain charges are evaluated by

$$q_{\mathrm{D}} = F_{\mathrm{D}}^{(0)} \cdot q_{\mathrm{I}} \tag{1.12}$$

$$q_{\mathrm{S}} = \left[1 - F_{\mathrm{D}}^{(0)} \right] \cdot q_{\mathrm{I}} \tag{1.13}$$

where $F_{\mathrm{D}}^{(0)}$ is the QS partitioning factor for drain charge.

The relaxation time, τ, is evaluated in the same way as (1.5) but with slightly different parameterization of the components for diffusion and drift currents (P_{diff} and P_{dr} are model parameters) [34]

$$\tau_{\mathrm{diff}} = \frac{L^2}{P_{\mathrm{diff}} \cdot \mu \cdot \phi_{\mathrm{t}}} \tag{1.14}$$

$$\tau_{\mathrm{dr}} = \frac{L^2 \cdot C_{\mathrm{ox}}}{P_{\mathrm{dr}} \cdot \mu \cdot q_{\mathrm{I}}^{(0)}} \tag{1.15}$$

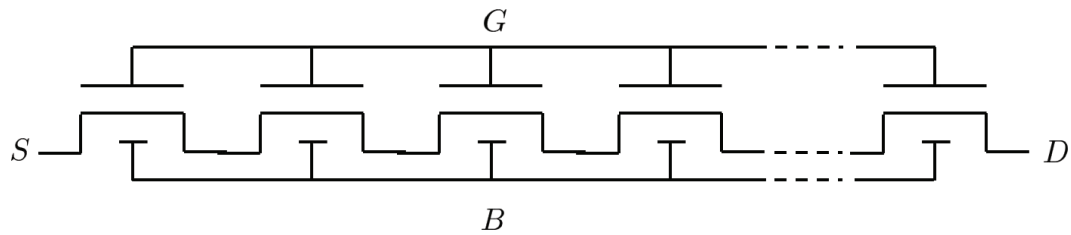

Fig. 1.1. Schematic for channel segmentation method

Similarly,

$$\frac{1}{\tau_{\mathrm{B}}} = \frac{1}{\tau_{\mathrm{diff}}} + \frac{1}{\tau_{\mathrm{dr,B}}} \tag{1.16}$$

and

$$\tau_{\mathrm{dr,B}} = \frac{L^2 \cdot C_{\mathrm{ox}}}{P_{\mathrm{dr,B}} \cdot \mu \cdot q_{\mathrm{I}}^{(0)}} \tag{1.17}$$

where $P_{\mathrm{dr,B}}$ is an additional model parameter.

The use of RTA (1.11) for q_{B} is unphysical as explained in [5]. In particular, it introduces inertia in the response of q_{B} to ψ_{S} which is not present in real devices.

1.2.3. Channel Segmentation Method

A powerful but computationally expensive method to model a MOS transistor operating under NQS condition is to view its channel as a series connection of segments, each segment being short enough to be modeled quasi-statically [1, 31, 69–78]. The NQS model in MM11 [47, 79, 80] is based on this approach. This idea is illustrated in Fig. 1.1 with each segment modeled by a "subtransistor." These subtransistors are assumed to consist only of intrinsic parts. In other words, no extrinsic source and drain regions at intermediate points are included. Also, it can be tricky to model short-channel effects.

1.2.4. SP-NQS and PSP-NQS

SP-NQS and PSP-NQS are ψ_S-based MOSFET models which are based on SP [81–85] and PSP [52,53,86–88], respectively. Both models are based on the cubic spine-collocation method which is a weighted residues method. The restraining equations and boundary condition are enforced on the continuity equation at each collocation point to construct a number of (the same number as the user specified collocation points) coupled ordinary differential equations. Detailed descriptions of the model can be found in [32, 33].

The cubic spline-collocation-method gives physically meaningful approximations and transforms the partial differential continuity equations into a system of ordinary differential equations. Another advantage of this method is that users can choose the number of collocation points to balance simulation speed and accuracy depending on their applications. Still, the spine-collocation NQS model is significantly slower than the QS model (but faster than the channel segmentation method.)

1.3. Existing Small-Signal NQS Models

During small-signal simulations, complex quantities such as the voltage phase and amplitude are used to reduce the complexity of computation [1, 89–91]; thus, the system matrix becomes complex with a real and imaginary part for each element. In the analysis of high-frequency MOSFET characteristics, the so-called "y-parameters" are often used. In this section, we developed the y-parameter models for the RTA-based NQS MOSFET model to perform the benchmark test suggested

in [62]. The standard definition of y-matrix in circuit theory is as follows

$$y_{\mathrm{jk}} = i_{\mathrm{j}}\big|_{v_{\mathrm{m}}=\delta_{\mathrm{mk}}} \tag{1.18}$$

For a linear 4-port network, it is assumed that the small-signal terminal currents i_{d}, i_{g}, i_{s}, and i_{b} are linear functions of the applied small-signal terminal voltages v_{d}, v_{g}, v_{s}, and v_{b}. Superposition principle may be applied to find a terminal current i_{j} when all four of the small-signal voltages are nonzero:

$$i_{\mathrm{j}} = y_{\mathrm{jd}}v_{\mathrm{d}} + y_{\mathrm{jg}}v_{\mathrm{g}} + y_{\mathrm{js}}v_{\mathrm{s}} + y_{\mathrm{jb}}v_{\mathrm{b}}, \quad \mathrm{j} \in \{\mathrm{d}, \mathrm{g}, \mathrm{s}, \mathrm{b}\} \tag{1.19}$$

The y-matrix satisfies certain conditions which follow from the following observations:

(1) There is no current flowing if all four small-signal potentials are identical.

(2) The sum of the total 4 small-signal currents have to be zero for a 4-port network.

Consequently, the relations between the y-parameters are as follows

$$\sum_{\mathrm{k}} y_{\mathrm{jk}} = 0 \tag{1.20}$$

$$\sum_{\mathrm{j}} y_{\mathrm{jk}} = 0 \tag{1.21}$$

1.3.1. Small-Signal Model in [1]

Physically formulating the y_{jk} terms is non-trivial, as it requires the solution to the coupled continuity and drift-diffusion equations. Sometimes, numerical results might be practically obtained and used. Analytical solutions are available with simplifying approximations. Presented in [1, 35, 92] is a four-terminal small-signal dc-to-high-frequency model, valid in weak, moderate, and strong inversion regimes.

This model is advantageous in the following aspects. First, it is formulated in a single continuous expression valid for weak, moderate, and strong inversion regimes which is free of discontinuities across the boundaries of different regimes. Second, it is for a 4-terminal MOSFET device which is capable of modeling various substrate effects. Third, it reduces to the QS version of the model at sufficiently low frequencies which contains the nonreciprocal capacitive effects [93].

Various approximations have been made to arrive at the analytic expressions for y_{jk} in [1, 35]. The first assumption is since ψ_{S} only changes slightly as the gate to bulk voltage, v_{GB}, increases in strong inversion, ψ_{S} is assumed to be pinned at

$$\psi_{\mathrm{S}} \approx \phi_0 + V_{\mathrm{CB}} \tag{1.22}$$

where V_{CB} is the channel to bulk voltage,

$$\phi_0 \approx 2\phi_{\mathrm{F}} + \Delta\phi \tag{1.23}$$

with $\Delta\phi$ equal to several ϕ_{t}.

Another assumption made is that, in strong inversion, the negative of the normalized inversion charge u_{I} (for the source referenced model)

$$u_{\mathrm{I}} = v_{\mathrm{GS}} - V_{\mathrm{FB}} - \phi_0 - \gamma\sqrt{\phi_0 + V_{\mathrm{SB}}} - \alpha_0 V_{\mathrm{CS}} \tag{1.24}$$

where V_{FB} is the flatband voltage, γ is the body effect coefficient, and

$$\alpha_0 = 1 + \frac{\gamma}{2\sqrt{\phi_0 + V_{\mathrm{SB}}}} \tag{1.25}$$

. Here, the bulk charge is linearized at its dc biasing point.

The results are

$$y_{\mathrm{jk}} = \frac{\sum_{l=0}^{2} (i\omega)^l N_{\mathrm{jk,l}}}{\sum_{l=0}^{2} (j\omega)^l D_{\mathrm{l}}} \tag{1.26a}$$

where

$$D_0 = 1 \tag{1.27a}$$

$$D_1 = \frac{4}{15\omega_{\mathrm{o}}} \frac{1 + 3\eta_0 + \eta_0^2}{(1+\eta_0)^3} \tag{1.27b}$$

$$D_2 = \frac{1}{45\omega_{\mathrm{o}}^2} \frac{1 + 4\eta_0 + \eta_0^2}{(1+\eta_0)^4} \tag{1.27c}$$

and (we consider y_{gg}) [1]

$$N_{\mathrm{gg0}} = 0 \tag{1.28a}$$

$$N_{\mathrm{gg1}} = C_{\mathrm{ox}} \left[\frac{2}{3\alpha_0} \frac{1 + 4\eta_0 + \eta_0^2}{(1+\eta_0)^2} + \frac{\alpha_0 - 1}{\alpha_0} \right] \tag{1.28b}$$

$$N_{\mathrm{gg2}} = \frac{C_{\mathrm{ox}}}{\omega_{\mathrm{o}}} \left[\frac{2}{45\alpha_0} \frac{2 + 11\eta_0 + 2\eta_0^2}{(1+\eta_0)^3} + \frac{4}{15} \frac{\alpha_0 - 1}{\alpha_0} \frac{1 + 3\eta_0 + \eta_0^2}{(1+\eta_0)^3} \right] \tag{1.28c}$$

Here

$$\eta_0 = \begin{cases} 1 - \dfrac{V_{\mathrm{DS}}}{V_{\mathrm{DS}}'}, & V_{\mathrm{DS}} \leq V_{\mathrm{DS}}' \quad (1.29a) \\ 0. & V_{\mathrm{DS}} > V_{\mathrm{DS}}' \quad (1.29b) \end{cases}$$

$$V_{\mathrm{DS}}' = \frac{V_{GS} - V_{\mathrm{T}}}{\alpha_0} \tag{1.30}$$

$$\omega_o = \frac{\mu(V_{GS} - V_{\mathrm{T}})}{L^2} \tag{1.31}$$

Naturally, these equations are only valid for strong inversion and do not cover all regions of MOSFET operation; in addition they do not account for any small geometry effects and assume constant mobility.

1.3.2. Small-Signal Models in [2, 3]

A set of analytic expressions is presented in [2] for the small-signal analysis of NQS operation of the MOS transistor. This model is derived from the q_{I}-based EKV compact model [94–98]. Expressions for the figures of merit for small-signal analysis are formulated which are valid from weak to strong inversion regimes. The model is derived from the continuity equation and drift-diffusion equation, and relies on the assumptions that underlie q_{I}-based compact models. The results are written in the form of a normalized y-matrix, which is expressed in terms of normalized variables including currents and frequency, so that they are independent of the process parameters such as mobility and substrate doping. From this approach, first and second order approximations to the detailed analytical expressions have been obtained.

The results are expressed in terms of Bessel functions of fractional orders and of complex arguments. Such functions are not available in most programming environments, and their numerical evaluation tends to be slow and have poor convergence. Therefore, the results require simplifications in order to become practically useful. In [3], it is proposed that a simple equivalent small-signal circuit is sufficient to express the terms of the transadmittances in [2]. [3] further shows that these functions can be represented in two simple forms, which are valid for all operating regions. Approximate analytical expressions are also proposed in [3].

1.3.3. Small-Signal Model in [4]

In [4], a small-signal MOSFET model is described, which takes the local effects of both velocity saturation and transverse mobility reduction into account.

The model is based on the PSP model and is valid for both QS and NQS operation. Recently, it has been found that, in the presence of velocity saturation, the low-frequency capacitances cannot be determined from the Ward-Dutton charge-partitioning scheme [99, 100]. By use of the small-signal model developed in [4], it is demonstrated that, in the presence of velocity saturation, no terminal drain and source charges exist, from which the capacitances can be derived. The small-signal model enables the determination of the correct capacitive behavior in the presence of velocity saturation. Furthermore, it is demonstrated how the small-signal model can be used to determine the number of collocation points needed in the large-signal NQS PSP model. Finally, inclusion of the local variation of mobility reduction due to the vertical electrical fields provides insight into the approach commonly applied in compact modeling, where these fields are replaced by global ones depending upon the terminal voltages only.

1.4. Present Work

In the present work, we develop a new version of the NQS model based on RTA for the inversion charge (and some other approximations detailed below.) No RTA is used for the bulk charge or (to be consistent with the neutrality condition) for the gate charge. This leads to increased accuracy while retaining the simplicity and speed of the model. Most importantly, the description of the NQS effects in the new formulation becomes reliable in the frequency range up to 1.5-2f_{T} (in this work f_{T} is a shorthand for $f_{\mathrm{T,max}}$ for a single transistor as described in [101, 102].) Since practical MOSFET applications for $f > 2f_{\mathrm{T}}$ are rare, this makes the new approach to NQS modeling suitable for most RF applications [59, 103–119].

We note in passing that if for some reason large-signal formulation is not required, then a variety of analytic small-signal models become available even without RTA [3, 4, 25, 35, 41, 44, 49, 50]. These are theoretically significant and in some cases may be practically useful. However, the emphasis in this work is on the complete large-signal formulation required by SPICE-like simulators. The small-signal version of the new model is derived entirely for the purpose of applying the benchmark test of [62].

While the work described in this thesis is based on PSP [52, 53] as the underlying QS model, the approach is quite general and with suitable modifications can be used with any advanced ψ_{s}-based model.

In summary, the main objective of the new RTA-based NQS model are as follows:

(1) To formulate an accurate and efficient approach for RF and mixed-signal circuit simulations,

(1-1) To achieve consistency between large-signal and small-signal simulations,

(1-2) To accurately model all terminal currents under NQS conditions up to $2f_{\mathrm{T,max}}$,

(1-3) To include all regions of MOSFET operation,

(1-4) To include short-channel-effects (SCEs),

(1-5) To achieve the consistency with QS simulation results for slow transients and low frequencies,

(2) To verify the new NQS model using PSP-NQS, TCAD results and measured data,

(3) To develop a new small-signal y-parameter model based on the new RTA-based

NQS model to perform the benchmark test of [62], and

(4) To implement the model into commonly used circuit simulators and demonstrate the applicability of the new NQS model using circuit simulations.

1.5. Organization of This Thesis

This thesis proceeds as follows. In chapter 2, we formulate the new version of RTA, which is verified by comparison with TCAD simulations and experimental data in chapter 3 while chapter 4 contains results based on the small-signal version of the model. After the modeling of the bulk resistance effect on the high frequency gate capacitances in chapter 5, the conclusions are presented in chapter 6.

CHAPTER 2

The New RTA-Based NQS MOSFET Model

2.1. Terminal Charges

To formulate the RTA, we introduce terminal charges at the source q_{S} and at the drain q_{D} and the total inversion charge $q_{\mathrm{I}} = q_{\mathrm{S}} + q_{\mathrm{D}}$. It is assumed that the equation

$$\frac{dq_{\mathrm{T}}}{dt} = -\frac{q_{\mathrm{T}} - q_{\mathrm{T}}^{(0)}}{\tau} \tag{2.1}$$

(τ is the relaxation time) is valid for T = S, D and hence, for T = I. Applying (2.1) to the source and drain charges directly differs from the approach in [34] where (2.1) was used for q_{I} and q_{B} after which the QS partition of the total inversion charge was adopted to compute q_{D} and q_{S},

$$q_{\mathrm{D}} = \frac{q_{\mathrm{D}}^{(0)}}{q_{\mathrm{I}}^{(0)}} \cdot q_{\mathrm{I}} \tag{2.2}$$

Strictly speaking, the relaxation time approximation (2.1) is not valid for q_{B} since the bulk charge has no inertia to follow the variation of surface potential, hence it doesn't have a characteristic relaxation time associated with it [5]. This aspect of the new NQS model is further detailed in section 5.2.

The inverse of the relaxation time entering (2.1) is modeled as in [29, 34]:

$$\frac{1}{\tau} = \frac{12\mu}{L^2}\left[K_{\mathrm{drift}} \cdot Q_{\mathrm{i}}^{(0)} + K_{\mathrm{diff}} \cdot \phi_{\mathrm{t}}\right] \tag{2.3}$$

where K_{drift} and K_{diff} are model parameters corresponding to the drift and diffusion current components, respectively, $Q_{\mathrm{i}}^{(0)} = -q_{\mathrm{I}}^{(0)}/C_{\mathrm{ox}}$, and $\phi_{\mathrm{t}} = k_{\mathrm{B}}T/q$ where k_{B} is Boltzmann's constant, T is the absolute temperature, and q is the magnitude of the

electronic charge. The form (2.3) is similar to the models of [29,34] but includes the physical factor 12, which follows from detailed analysis of inversion charge inertia with contacts to both source and drain [1].

The gate charge is

$$q_{\mathrm{G}} = W \int_0^L q_{\mathrm{G}}^{'} dy \tag{2.4}$$

where W is channel width and

$$q_{\mathrm{G}}^{'} = (C_{\mathrm{ox}}/WL)\left[v_{\mathrm{GB}} - V_{\mathrm{FB}} - \psi_{\mathrm{S}}(y)\right] \tag{2.5}$$

where $\psi_{\mathrm{S}}(y)$ is the surface potential at a point y along the channel (from $y = 0$ at the source to $y = L$ at the drain). Hence,

$$q_{\mathrm{G}} = C_{\mathrm{ox}}\left(v_{\mathrm{GB}} - V_{\mathrm{FB}} - \overline{\psi_{\mathrm{S}}}\right) \tag{2.6}$$

where the average value of the surface potential along the channel is

$$\overline{\psi_{\mathrm{S}}} = \frac{1}{L}\int_0^L \psi_{\mathrm{S}}(y) dy \ . \tag{2.7}$$

The bulk charge is

$$q_{\mathrm{B}} = W \int_0^L q_{\mathrm{B}}^{'} dy \tag{2.8}$$

where $q_{\mathrm{B}}^{'}$ is the bulk charge density per unit area which, unlike the inversion charge, responds practically instantaneously to changes in the surface potential. The functional form of the $q_{\mathrm{B}}(\psi_{\mathrm{S}})$ dependence is not affected by NQS effects so

$$q_{\mathrm{B}}^{'} = -\frac{\mathrm{sgn}(\psi_{\mathrm{S}})\, C_{\mathrm{ox}}\, \gamma\, \beta^{-1/2}\sqrt{e^{-\beta\psi_{\mathrm{S}}} + \beta\psi_{\mathrm{S}} - 1}}{WL} \tag{2.9}$$

where $\beta = 1/\phi_{\mathrm{t}}$, thus

$$q_{\mathrm{B}} = -\frac{\mathrm{sgn}(\psi_{\mathrm{S}})\, C_{\mathrm{ox}}\, \gamma\, \beta^{-1/2}}{L} \int_0^L \sqrt{e^{-\beta\psi_{\mathrm{S}}} + \beta\psi_{\mathrm{S}} - 1}\, dy\ . \tag{2.10}$$

From the first mean-value theorem of integral calculus, there exists a point $y^* \in (0, L)$ such that

$$q_{\mathrm{B}} = -\mathrm{sgn}(\psi_{\mathrm{S}}^*)\, C_{\mathrm{ox}}\, \gamma\, \beta^{-1/2} \sqrt{e^{-\beta\psi_{\mathrm{S}}^*} + \beta\psi_{\mathrm{S}}^* - 1} \tag{2.11}$$

where $\psi_{\mathrm{S}}^* = \psi_{\mathrm{S}}(y^*)$.

Generally speaking, ψ_{S}^* is not known, varies with bias, and differs from $\overline{\psi_{\mathrm{S}}}$ as defined in (2.7). In the QS case the symmetric linearization method [53, 120] gives

$$\psi_{\mathrm{S}}^* \approx \psi_{\mathrm{M}} - \frac{(\Delta\psi)^2}{12H} \approx \overline{\psi_{\mathrm{S}}} \tag{2.12}$$

where

$$\psi_{\mathrm{M}} = (\psi_{\mathrm{S0}} + \psi_{\mathrm{SL}})/2 \tag{2.13}$$

$$\Delta\psi = \psi_{\mathrm{SL}} - \psi_{\mathrm{S0}} \tag{2.14}$$

ψ_{S0} and ψ_{SL} denote the surface potentials at the source and drain ends of the channel, respectively, and H is a bias-dependent but position-independent variable whose precise value depends on the details of the velocity-field relation implemented in the compact model. Here, we use H in the form given in [53].

The additional approximation we make is that

$$\psi_{\mathrm{S}}^* \approx \overline{\psi_{\mathrm{S}}} \tag{2.15}$$

is valid in the more general NQS case. Note that we do not assume that the ψ_{S}^* dependence on ψ_{M} and $\Delta\psi$ remains unchanged in the NQS case, which means that (2.15) is a weaker condition than (2.12).

We believe that (2.15) is preferable to assuming that (2.1) applies to the bulk charge. Indeed, (2.15) produces some numerical error in the evaluation of q_{B} while using RTA for q_{B} introduces an unphysical inertia in the response of q_{B} to the surface potential variation. The approximate validity of the NQS model based on (2.1) and (2.15) is justified by comparison with TCAD simulations, experimental data, and a benchmark test in subsequent sections.

The charge neutrality condition

$$q_{\mathrm{G}} + q_{\mathrm{I}} + q_{\mathrm{B}} = 0 \tag{2.16}$$

with (2.6) and (2.15) gives

$$C_{\mathrm{ox}}\left(v_{\mathrm{GB}} - V_{\mathrm{FB}} - \overline{\psi_{\mathrm{S}}}\right) + q_{\mathrm{I}} + q_{\mathrm{B}}(\overline{\psi_{\mathrm{S}}}) = 0 \tag{2.17}$$

where $q_{\mathrm{B}}(\overline{\psi_{\mathrm{S}}})$ is given by (2.11) with ψ_{S}^{*} replaced by $\overline{\psi_{\mathrm{S}}}$. Note that while the corresponding equation for the charge densities per unit area, $q_{\mathrm{I}}^{'}$ and $q_{\mathrm{B}}^{'}$,

$$(C_{\mathrm{ox}}/WL)\left(v_{\mathrm{GB}} - V_{\mathrm{FB}} - \psi_{\mathrm{S}}\right) + q_{\mathrm{I}}^{'} + q_{\mathrm{B}}^{'}(\psi_{\mathrm{S}}) = 0 \tag{2.18}$$

is exact, the equation (2.17) for the charges is approximate and is based on (2.15). The terminal charges are computed as follows: the RTA equations (2.1) are solved for q_{I} and q_{D}; with q_{I} known, $\overline{\psi_{\mathrm{S}}}$ is determined from (2.17) using an accurate analytical approximation originally developed for varactor modeling [59]; with $\overline{\psi_{\mathrm{S}}}$ thus determined q_{G} is evaluated from (2.6); and, finally, q_{B} is calculated from (2.16). All small-geometry and secondary effects are inherited from the QS model used to compute μ, $q_{\mathrm{I}}^{(0)}$, and $q_{\mathrm{B}}^{(0)}$. The resulting NQS model is coded in Verilog-A to make it portable across circuit simulators. While the simulations presented below were

performed using the Verilog-A compilers of two widely used simulators: Spectre and ADS, we have also used automatically generated C-code [121] with identical results. Typical execution time increases by about 40% relative to the QS PSP model [52, 53] which is acceptable for NQS simulations; the exact computational overhead compared to QS modeling depends on details of the circuit, analysis performed, computing platform, compiler, and similar factors.

In this section, we have obtained large-signal NQS terminal charges. This is summarized in Table 2.1.

TABLE 2.1
SUMMARY OF EVALUATION OF TERMINAL CHARGES IN PSP-RTA-NQS

Sequence	Terminal Charge	Equation(s)	Comments
1	q_{D}	(2.1)	q_{D} satisfies (2.1)
2	q_{S}	Equivalently by (2.1)	q_{S} satisfies (2.1)
3	q_{G}	(2.6) and (2.17)	(2.11) and (2.15)
4	q_{B}	(2.16)	NA

2.2. Terminal Currents

Terminal currents are given by

$$i_{\mathrm{D}} = I_{\mathrm{D}} + \frac{dq_{\mathrm{D}}}{dt} \tag{2.19}$$

$$i_{\mathrm{G}} = I_{\mathrm{G}} + \frac{dq_{\mathrm{G}}}{dt} \tag{2.20}$$

$$i_{\mathrm{S}} = I_{\mathrm{S}} + \frac{dq_{\mathrm{S}}}{dt} \tag{2.21}$$

$$i_{\mathrm{B}} = I_{\mathrm{B}} + \frac{dq_{\mathrm{B}}}{dt} \tag{2.22}$$

where I_{D}, I_{G}, I_{S}, and I_{B} are convection currents which are computed by the PSP-QS model.

2.3. Small-Geometry Effects, Parasitics, and Noise

Model equations for the small-geometry effects (such as the polysilicon depletion effect [122–125], quantum mechanical corrections [126–129], etc.) are inherited from the PSP-QS model and their description is not affected by the RTA approach. Parasitics [130–132] are also modeled automatically. An NQS noise model [110, 133–148] is not included in the present work. More precisely, small-geometry effects, parasitics, and noise models are included in $i_{\mathrm{D}}^{(0)}$, $i_{\mathrm{G}}^{(0)}$, $i_{\mathrm{S}}^{(0)}$, $i_{\mathrm{B}}^{(0)}$, $q_{\mathrm{D}}^{(0)}$, $q_{\mathrm{G}}^{(0)}$, $q_{\mathrm{S}}^{(0)}$, and $q_{\mathrm{B}}^{(0)}$. The geometry dependance of τ is given by (2.3).

CHAPTER 3

Model Validation

3.1. Model Validation with TCAD

The new RTA-based NQS model has been implemented in PSP103 [53] and is called PSP-RTA-NQS. Comparisons with two-dimensional (2-D) TCAD [149] results for large-signal simulations are shown in Figs. 3.1-3.4 and for small-signal simulations in Figs. 3.5-3.8. In all cases, W=1 μm, L=5 μm, V_{SB} =0, t_{ox}=2 nm, μ=0.104 m^2/V-s, N_{sub}=3 $\times$ 10^{23} m^{-3}, and T=300 K. The relatively large L was selected to emphasize the NQS effects.

Figs. 3.1 and 3.2 show the terminal currents during switching from depletion to strong inversion operation for $dV_{\mathrm{G}}/dt = 10^{10}$ V/s; results from the QS version of PSP are also shown for comparison. There is good agreement between PSP-RTA-NQS and TCAD simulations, and the improvement over PSP-QS is apparent. Fig. 3.3 shows transient gate and bulk current during switching from accumulation to strong inversion for a ramp rate of 2×10^{10} V/s. As expected, NQS effects appear only when the inversion charge becomes significant. This further illustrates the fact that there is no inertia involved in the formation of the bulk charge (at least until the Maxwell relaxation becomes relevant) [5].

RTA-based models are approximations and become less accurate as voltage ramp rates increase, see Fig. 3.4 for gate and bulk currents for a ramp rate of 5×10^{11}V/s. Even in this extreme case, the qualitative behavior of the PSP-RTA-NQS model remains reasonable.

While an ability to model the large-signal response to a fast transient is im-

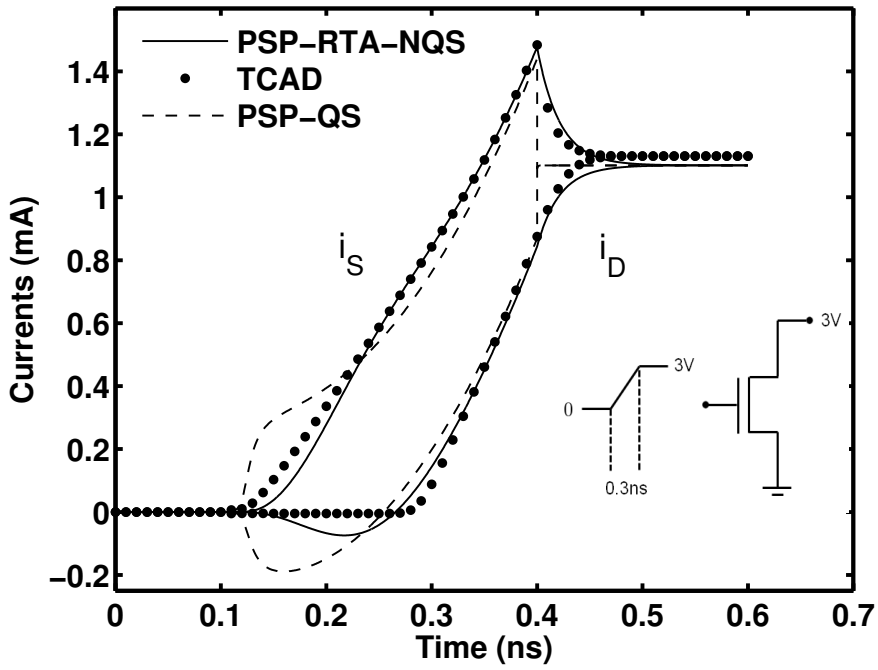

Fig. 3.1. Drain and source terminal currents for v_{GS} switching from 0 to 3 V at 10^{10} V/s; V_{DS}=3 V and V_{BS}=0.

portant for NQS models, RF circuit design requires small-signal modeling, including transcapacitances, at high frequencies. Figs. 3.5 and 3.6 show C_{gg} and C_{gs}, respectively, for f from 0 to $2f_{\mathrm{T}}$; the new model fits the TCAD results well, with some inaccuracy at the onset of strong inversion at the highest frequency. Fig. 3.7 shows C_{bg} over a significantly extended frequency range; although neither the gate nor the bulk charge are affected by the inertia in the inversion charge, if the partitioning of the NQS inversion charge into source and drain components is done incorrectly, then this induces errors in modeling C_{bg} at high frequencies; the inset in Fig. 3.7 shows that this is not the case for PSP-RTA-NQS.

A further interesting detail that demonstrates how NQS inversion charge par-

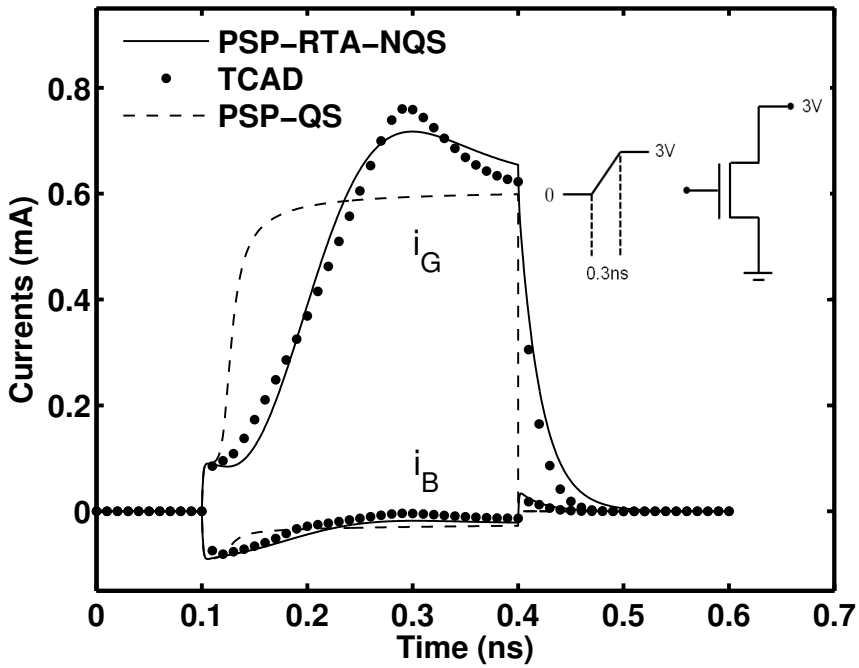

Fig. 3.2. Gate and bulk terminal currents for v_{GS} switching from 0 to 3 V at 10^{10} V/s, V_{DS}=3 V.

titioning qualitatively affects capacitance modeling is shown in Fig. 3.8. In our model formulation, as described in the previous section, the issue of partitioning does not arise since both q_{D} and q_{I} are individually computed from (2.1) and $q_{\mathrm{D}}^{(0)}$ and $q_{\mathrm{I}}^{(0)}$ are directly provided by the underlying QS model. This results in the physical monotonic behavior of C_{ds} as a function of the dc bias V_{GS} in Fig. 3.8. In contrast, if the ratio $q_{\mathrm{D}}/q_{\mathrm{I}}$ is assumed to be its QS value, as is done in previous RTA NQS models, then C_{ds} acquires an unphysical peak which becomes more pronounced as frequency increases.

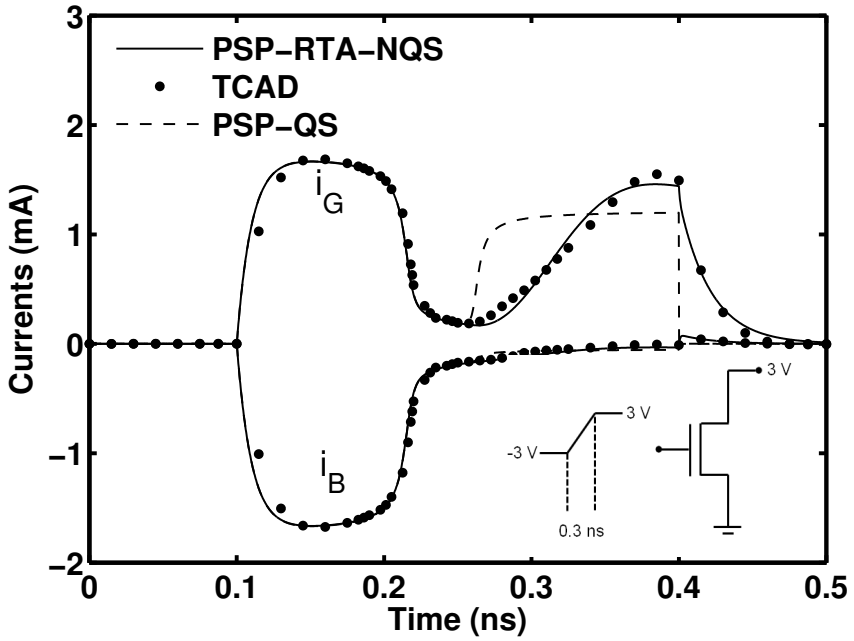

Fig. 3.3. Gate and bulk terminal currents for v_{GS} switching from -3 to 3 V at 2×10^{10} V/s; V_{DS}=3 V.

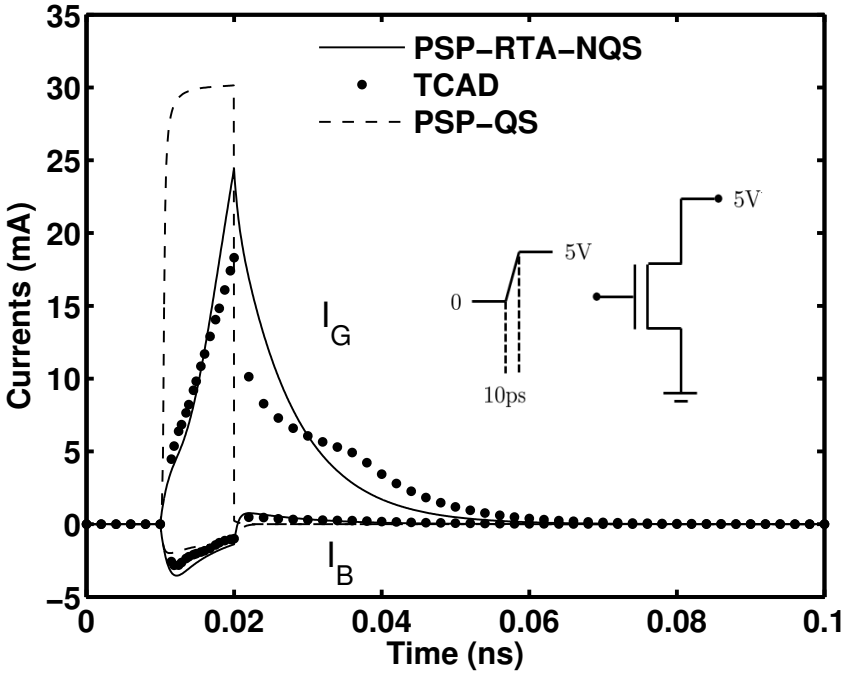

Fig. 3.4. Gate and bulk terminal currents for v_{GS} switching from 0 to 5 V at 5×10^{11} V/s; V_{DS}=5 V.

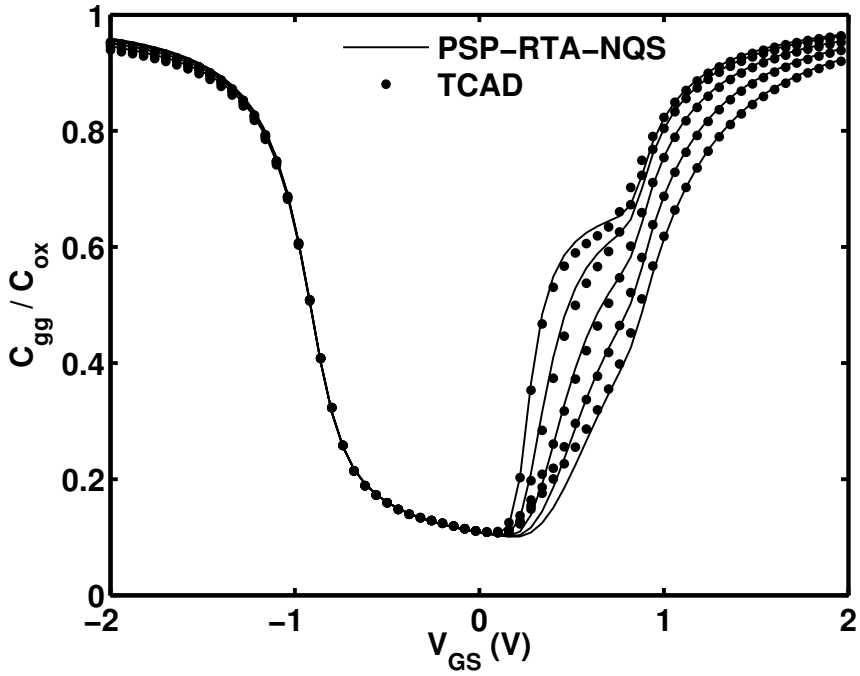

Fig. 3.5. C_{gg} for f=0, 0.5f_{T}, 1.0f_{T}, 1.5f_{T} and 2.0f_{T} (top to bottom), where f_{T}=1.6 GHz; V_{DS}=0.5 V. The weak frequency dependence in accumulation is completely due to the bulk resistance effect (extracted R_{bulk} = 116.8 Ω from TCAD data) [5].

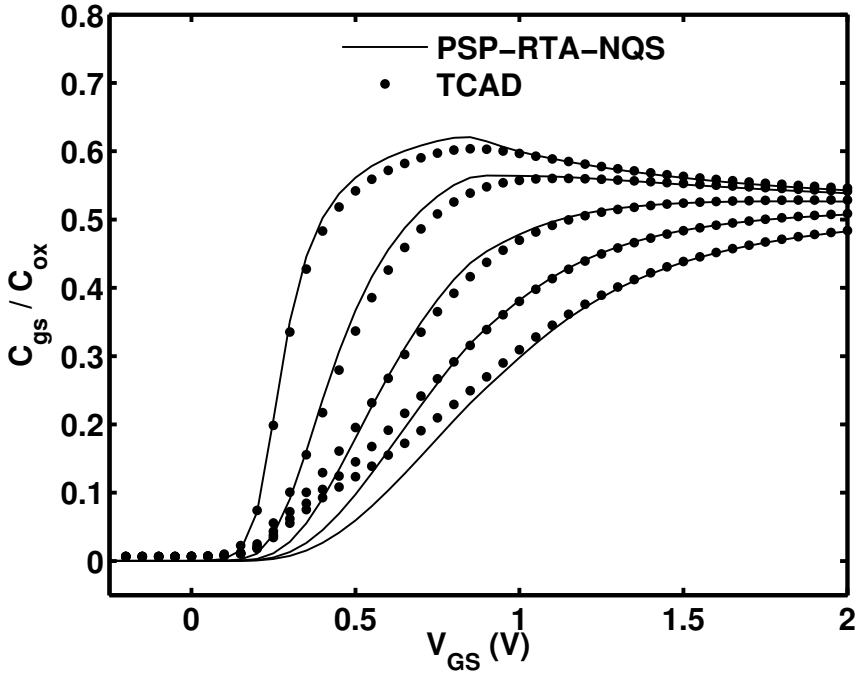

Fig. 3.6. C_{gs} for f=0, 0.5f_{T}, 1.0f_{T}, 1.5f_{T} and 2.0f_{T} (top to bottom), where f_{T} = 1.6 GHz; V_{DS}=0.5 V.

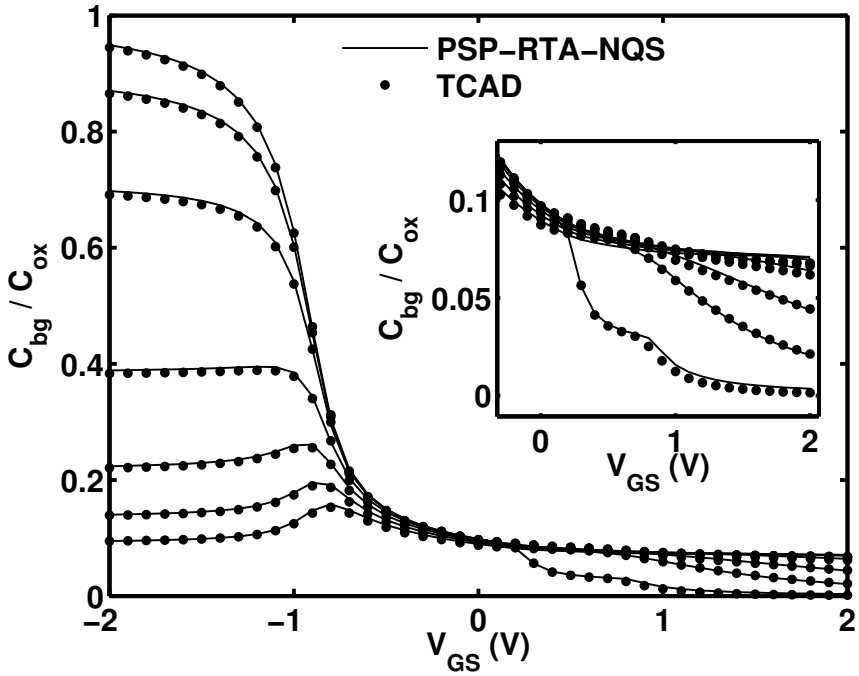

Fig. 3.7. C_{bg} for f=0, 3.1f_{T}, 6.3f_{T}, 12.5f_{T}, 18.8f_{T}, 25f_{T} and 31f_{T} (top to bottom in accumulation region, bottom to top in strong inversion inset), where f_{T}=1.6 GHz; V_{DS}=0.5 V. The significant decrease in the accumulation is completely due to the bulk resistance effect (extracted R_{bulk} = 116.8 Ω from TCAD data) [5].

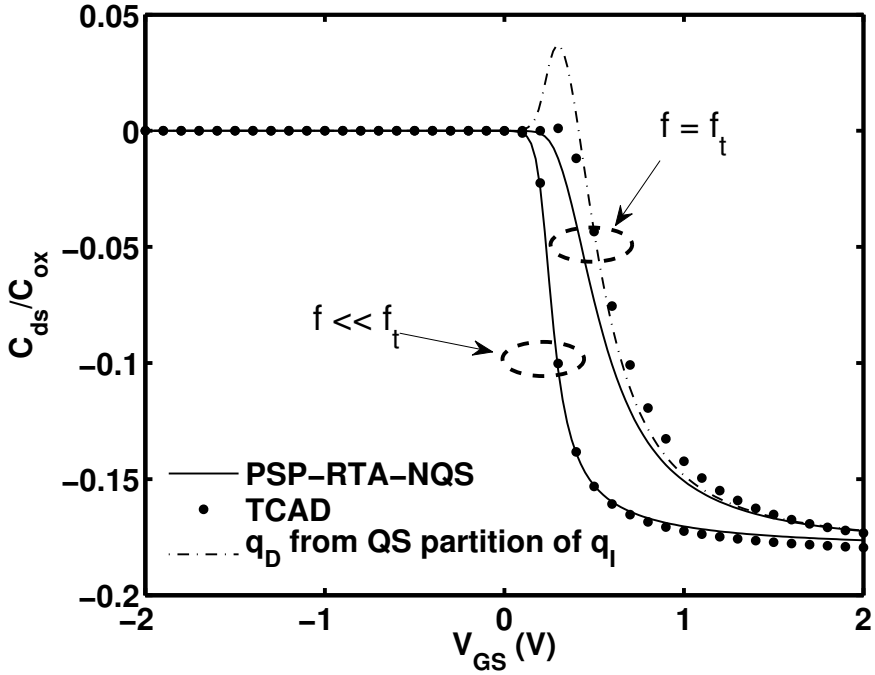

Fig. 3.8. $C_{\rm ds}$ from partitioning based on (2.1) (solid lines) and (2.2) (dot-dash lines), $f_{\rm T}$ = 1.6 GHz; $V_{\rm DS}$=0.

3.2. Model Validation with Experimental Data

To further validate the accuracy of the new model, we measured s-parameters, over a range of gate and drain biases and frequency with V_{BS}=0, for a PMOS transistor in a 90nm RF CMOS process. Fig. 3.9 shows the layout view of the device.

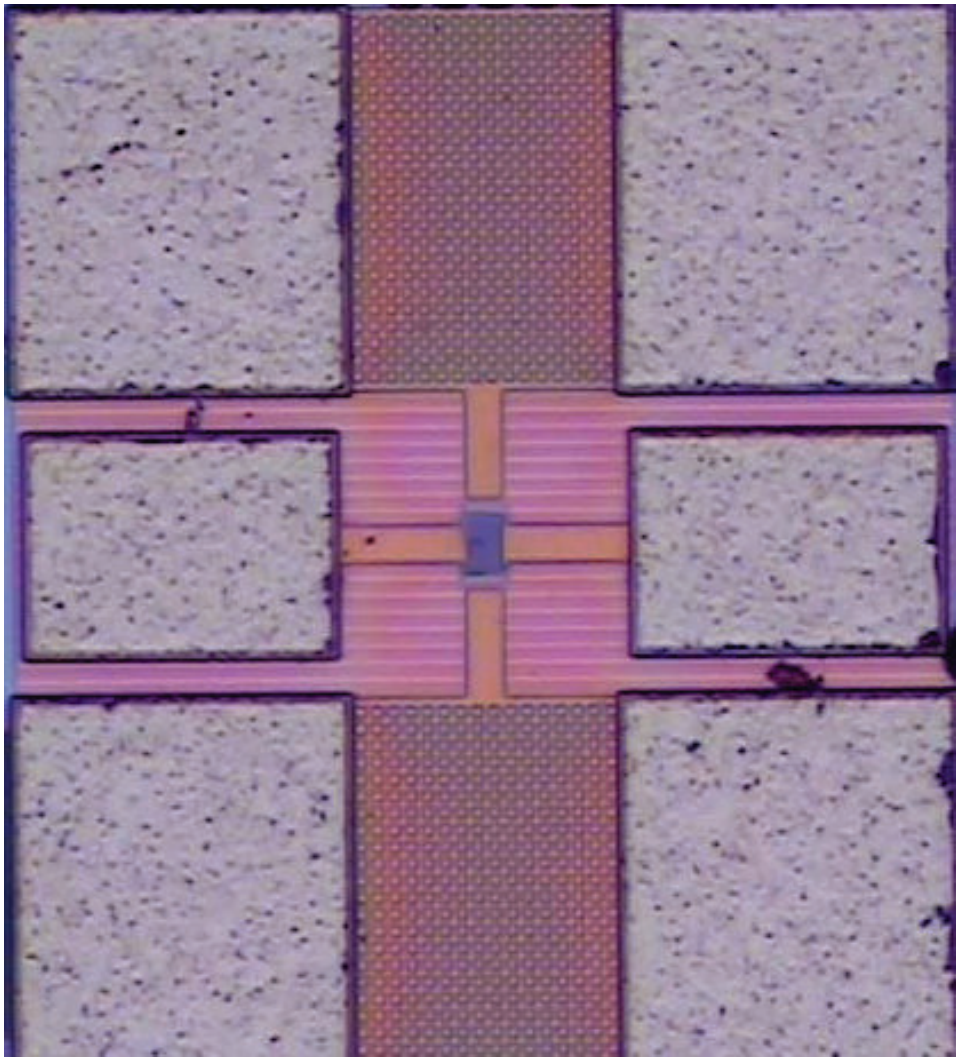

Fig. 3.9. Test device with GSG probe pad configuration. Courtesy of Freescale semiconductors, presented with permission.

The device was laid out in a 2-port ground-signal-ground (GSG) probe configuration, with the gate configured as port 1 and the drain as port 2; the structure included 6 gate fingers and a surrounding bulk contact ring, with two devices connected in parallel. De-embedding was done using a 2-step open-short technique [150].

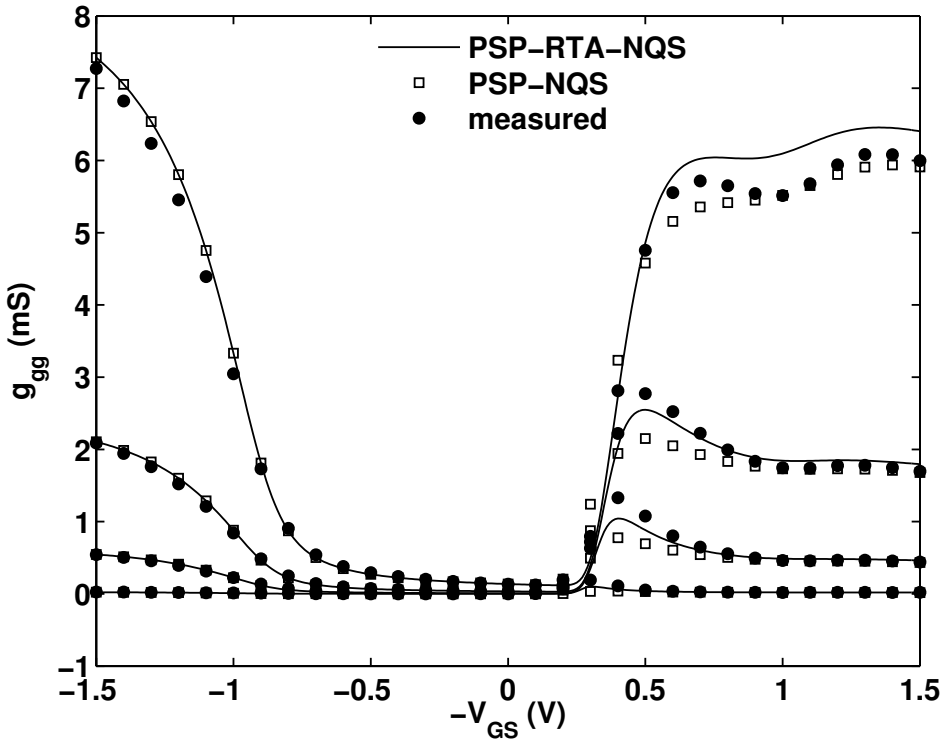

Fig. 3.10. Comparison of model and measured data for a PMOS g_{gg} when V_{DS} = -0.6 V. Frequencies are 0.1, 0.5, 1 and 2 GHz where $f_{\mathrm{T}} = 0.71$ GHz. $L = 1.2$ μm, $W = 10$ μm.

Figs. 3.10 through 3.33 show measured data from the device (cf. Fig. 3.9), along with simulation results from both the PSP-RTA-NQS model and, for comparison, PSP-NQS with the spine collocation points $N = 9$ which is the maximum allowed number. The y-parameters are shown over frequency both vs. V_{GS}, for fixed V_{DS}, and vs. V_{DS}, for fixed V_{GS}, with the fixed voltage value chosen to be that for

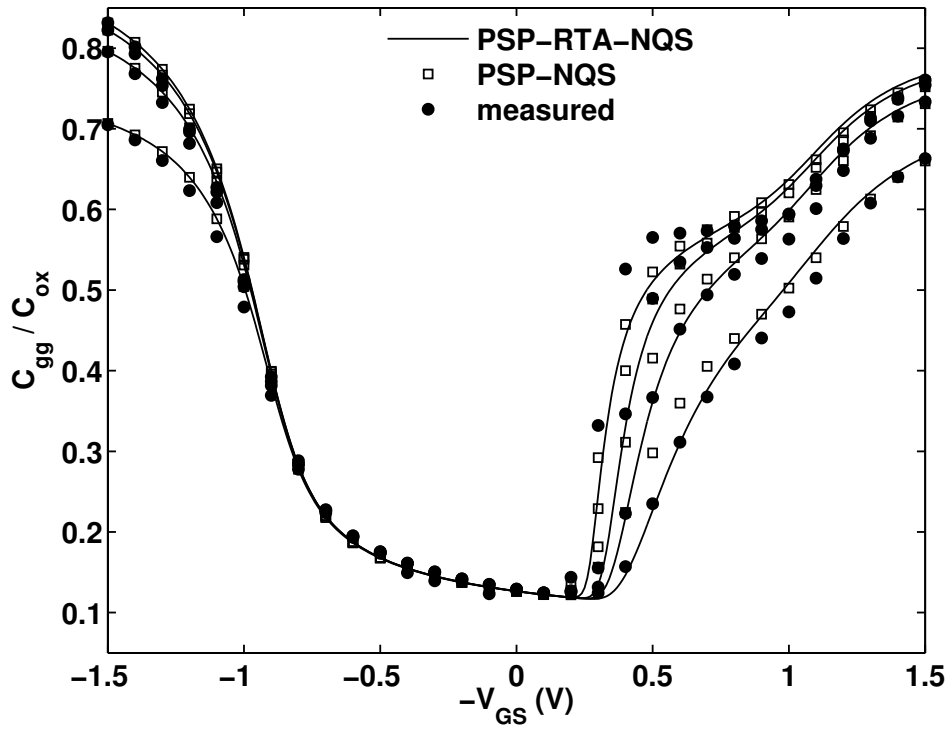

Fig. 3.11. Comparison of model and measured data for a PMOS C_{gg} when V_{DS} = -0.6 V. Frequencies are 0.1, 0.5, 1 and 2 GHz where $f_{\mathrm{T}} = 0.71$ GHz. $L = 1.2$ μm, $W = 10$ μm.

which there was the maximum change in qualitative behavior over both frequency and the swept bias. C_{jk} was calculated as $(2\delta_{\mathrm{jk}} - 1)\,\mathrm{Im}(y_{jk})/\omega$, with y_{jk} computed from transformation of the de-embedded s-parameters; f_{T} for the device is 0.71 GHz. R_{bulk} and R_{gate} were adjusted to provide a least squares fit to the data. The frequency and bias dependence of the measured data are fitted well, both qualitatively and quantitatively, by PSP-RTA-NQS, and in many of the plots it fits the data better than PSP-NQS, even though the latter is a significantly more complex model. For example, the peak in $g_{\mathrm{gg}}(V_{\mathrm{GS}})$ in Fig. 3.10 near threshold is able to be modeled by PSP-RTA-NQS.

In particular, Figs. 3.10 through 3.17 are the fitted frequency and gate bias dependance of conductances and normalized capacitances when $V_{\mathrm{DS}} = -0.6$V.

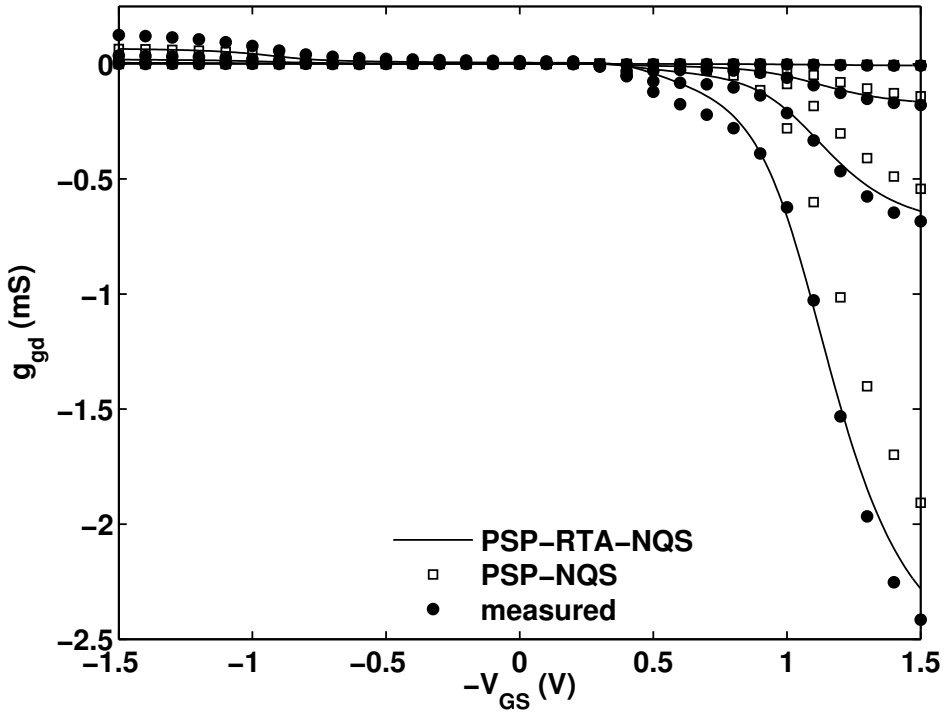

Fig. 3.12. Comparison of model and measured data for a PMOS g_{gd} when $V_{\mathrm{DS}} =$ -0.6 V. Frequencies are 0.1, 0.5, 1 and 2 GHz where $f_{\mathrm{T}} = 0.71$ GHz. $L = 1.2$ μm, $W = 10$ μm.

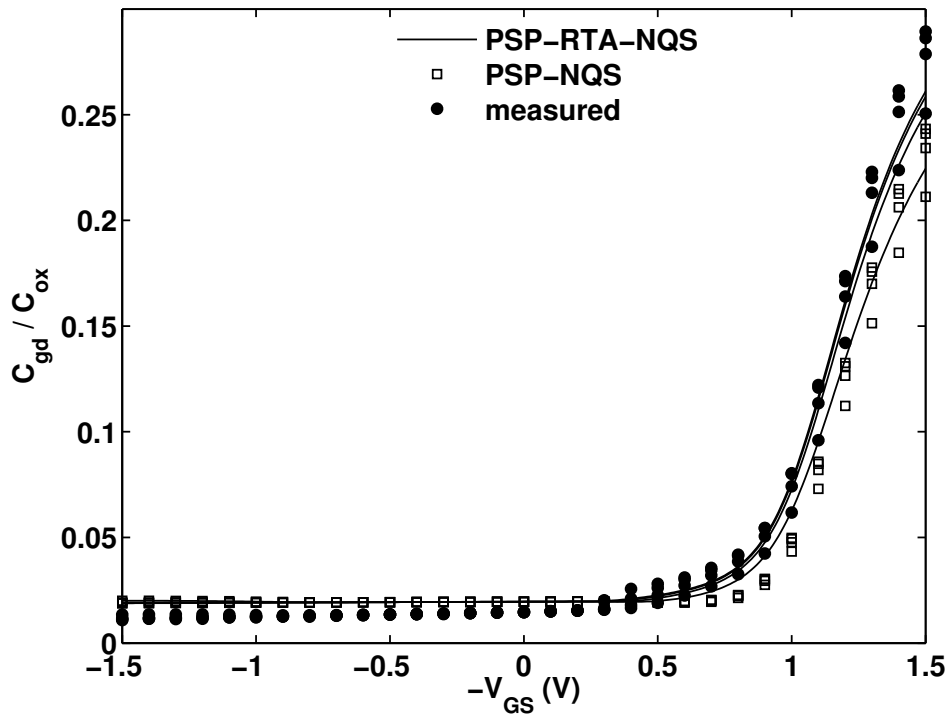

Fig. 3.13. Comparison of model and measured data for a PMOS C_{gd} when V_{DS} = -0.6 V. Frequencies are 0.1, 0.5, 1 and 2 GHz where $f_{\mathrm{T}} = 0.71$ GHz. $L = 1.2$ μm, $W = 10$ μm.

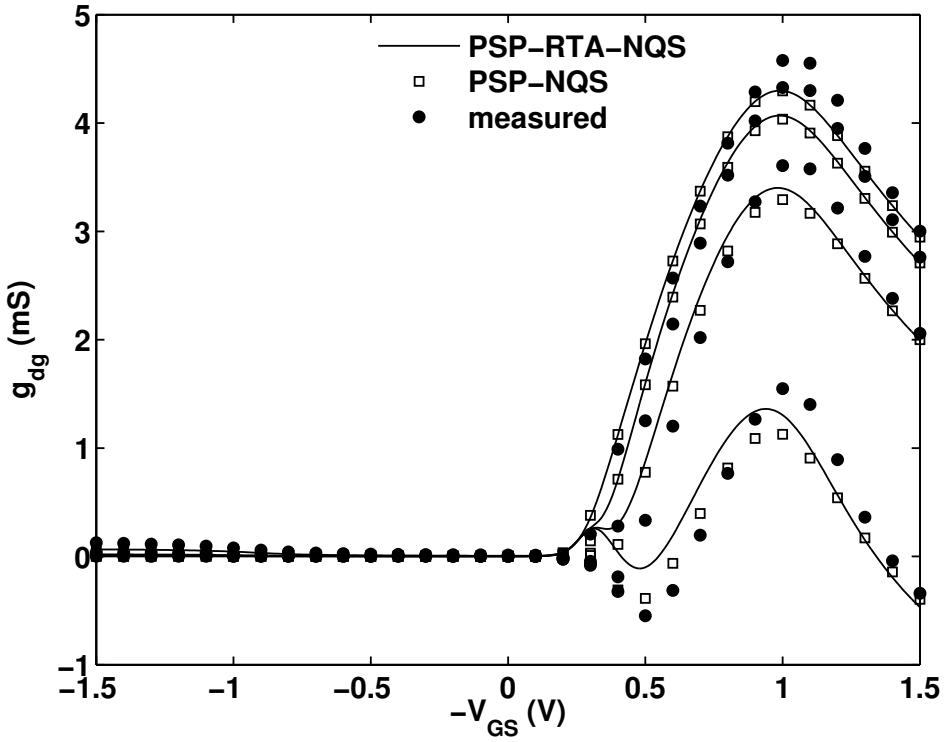

Fig. 3.14. Comparison of model and measured data for a PMOS g_{dg} when V_{DS} = -0.6 V. Frequencies are 0.1, 0.5, 1 and 2 GHz where $f_{\mathrm{T}} = 0.71$ GHz. $L = 1.2$ μm, $W = 10$ μm.

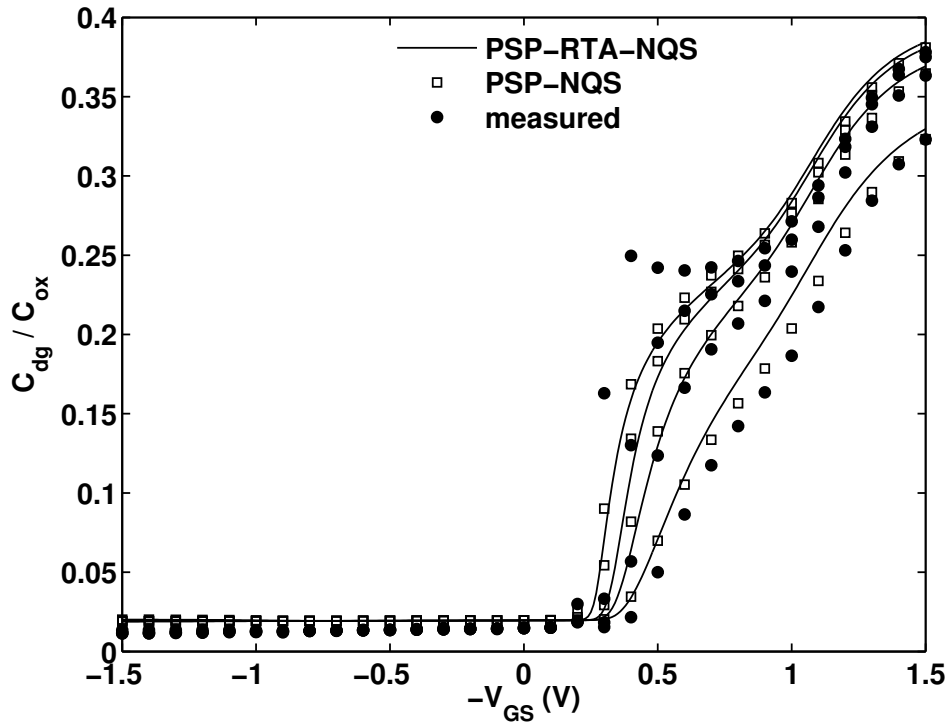

Fig. 3.15. Comparison of model and measured data for a PMOS C_{dg} when V_{DS} = -0.6 V. Frequencies are 0.1, 0.5, 1 and 2 GHz where $f_{\mathrm{T}} = 0.71$ GHz. $L = 1.2$ μm, $W = 10$ μm.

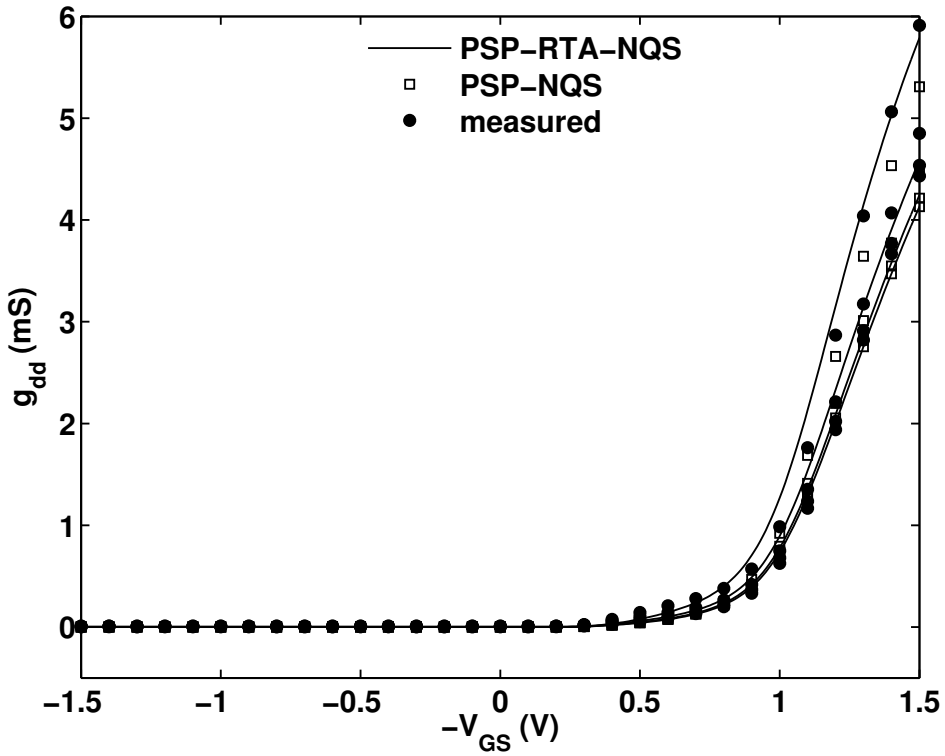

Fig. 3.16. Comparison of model and measured data for a PMOS g_{dd} when V_{DS} = -0.6 V. Frequencies are 0.1, 0.5, 1 and 2 GHz where f_{T} = 0.71 GHz. L = 1.2 μm, W = 10 μm.

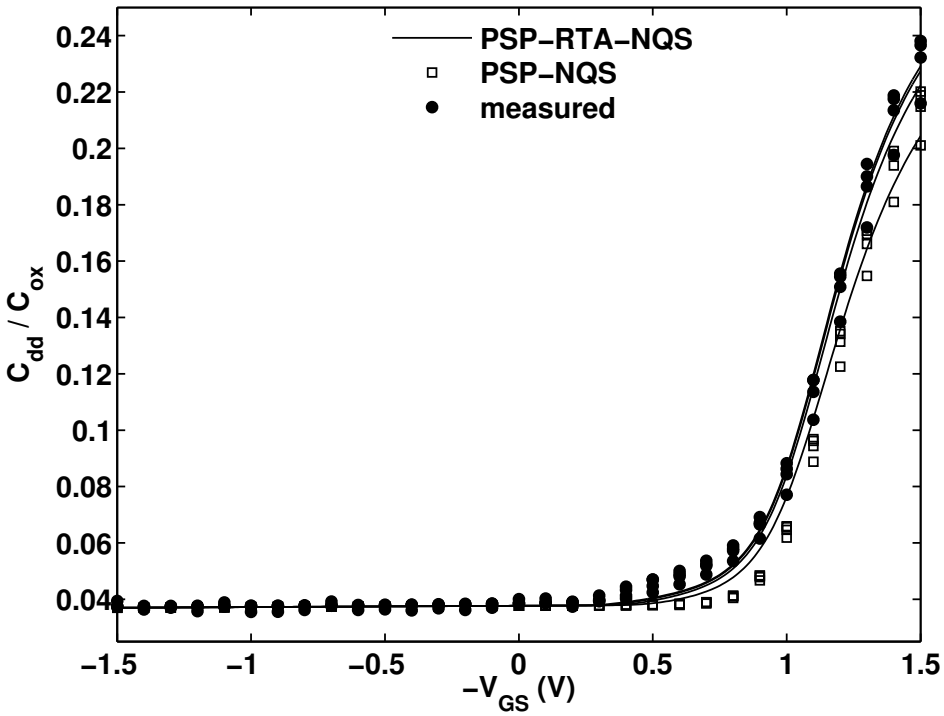

Fig. 3.17. Comparison of model and measured data for a PMOS C_{dd} when V_{DS} = -0.6 V. Frequencies are 0.1, 0.5, 1 and 2 GHz where $f_{\mathrm{T}} = 0.71$ GHz. $L = 1.2$ μm, $W = 10$ μm.

Figs. 3.18 through 3.25 are the fitted frequency and drain bias dependance of conductances and normalized capacitances when $V_{\mathrm{GS}} = -0.8$V.

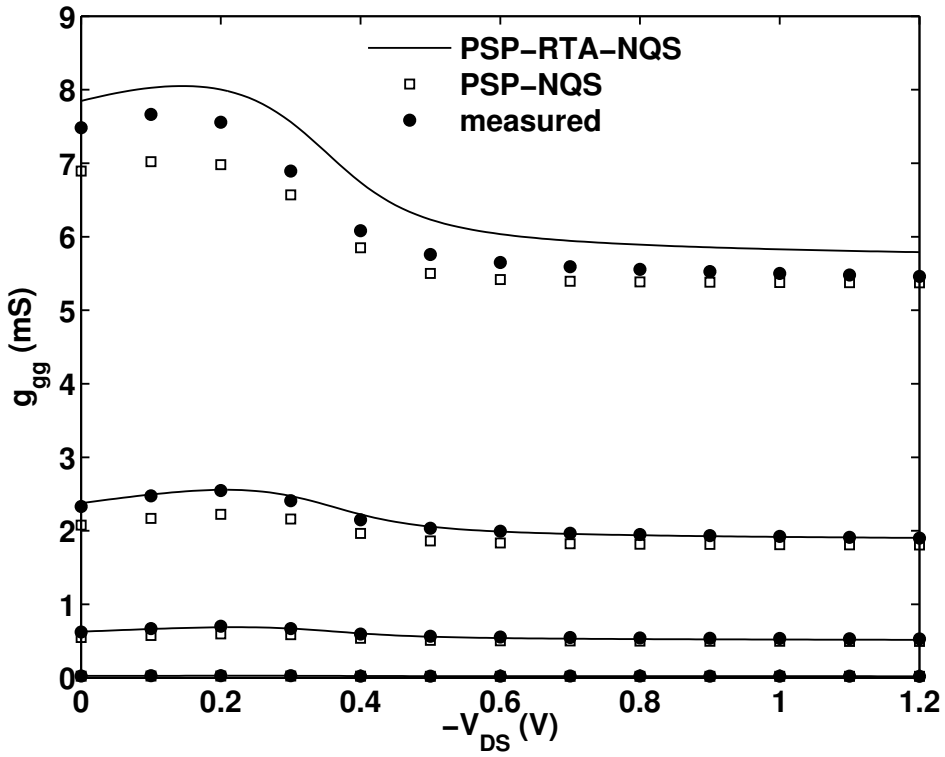

Fig. 3.18. Comparison of model and measured data for a PMOS g_{gg} when V_{GS} = -0.8 V. Frequencies are 0.1, 0.5, 1 and 2 GHz where $f_{\mathrm{T}} = 0.71$ GHz. $L = 1.2$ μm, $W = 10$ μm.

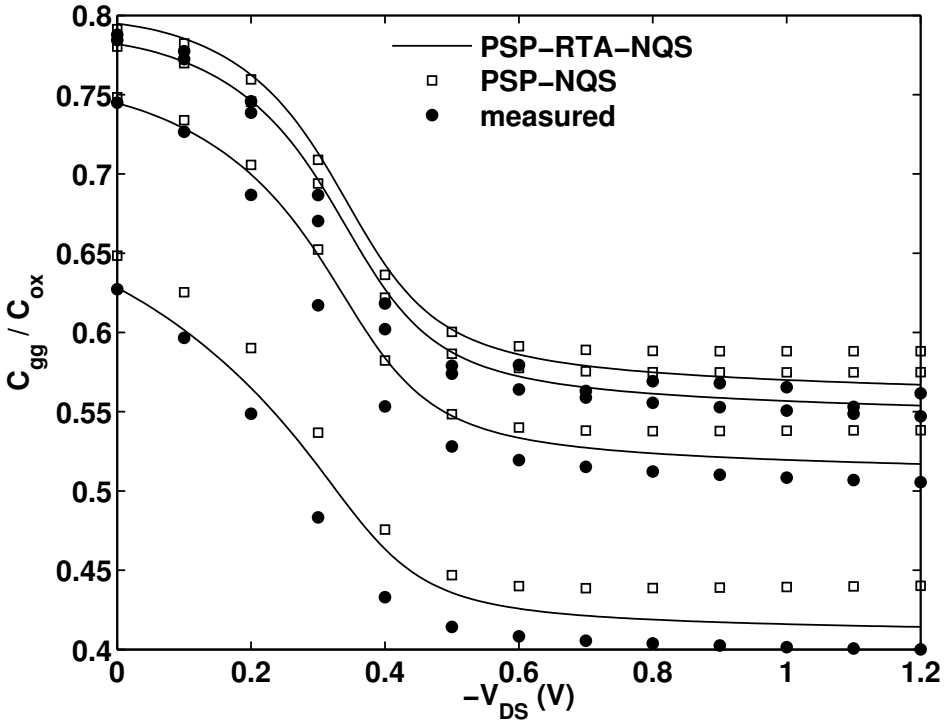

Fig. 3.19. Comparison of model and measured data for a PMOS C_{gg} when V_{GS} = -0.8 V. Frequencies are 0.1, 0.5, 1 and 2 GHz where $f_{\mathrm{T}} = 0.71$ GHz. $L = 1.2$ μm, $W = 10$ μm.

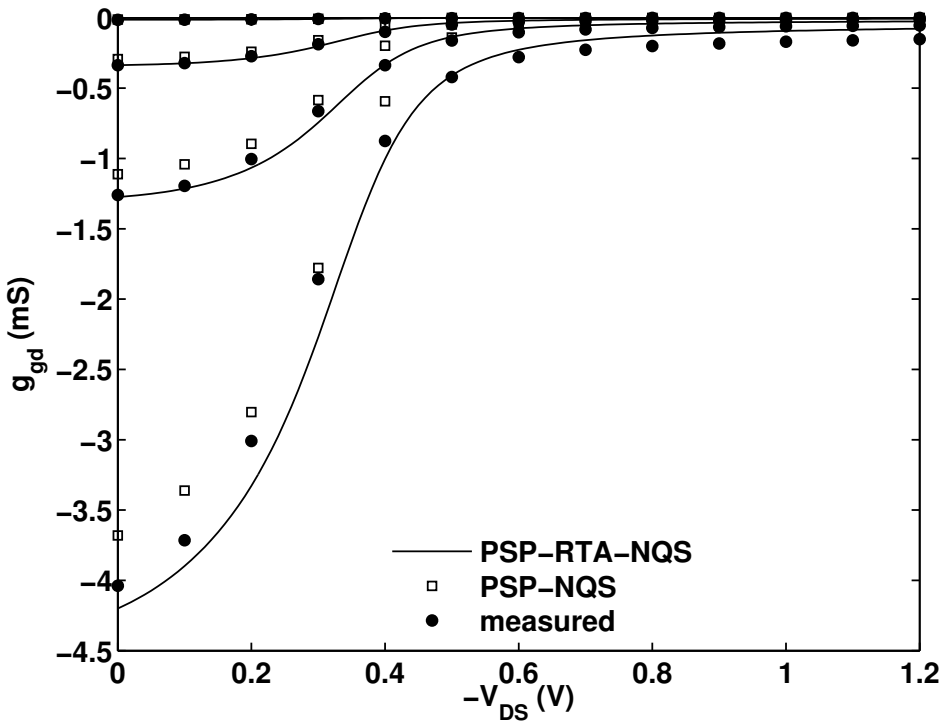

Fig. 3.20. Comparison of model and measured data for a PMOS g_{gd} when V_{GS} = -0.8 V. Frequencies are 0.1, 0.5, 1 and 2 GHz where $f_{\mathrm{T}} = 0.71$ GHz. $L = 1.2$ μm, $W = 10$ μm.

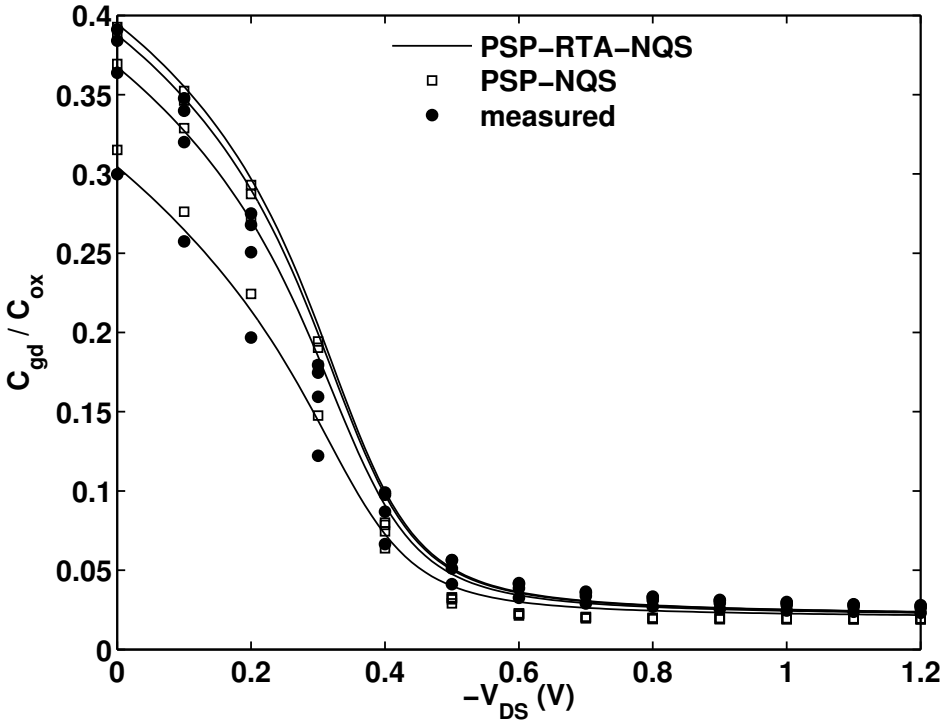

Fig. 3.21. Comparison of model and measured data for a PMOS C_{gd} when V_{GS} = -0.8 V. Frequencies are 0.1, 0.5, 1 and 2 GHz where $f_{\mathrm{T}} = 0.71$ GHz. $L = 1.2$ μm, $W = 10$ μm.

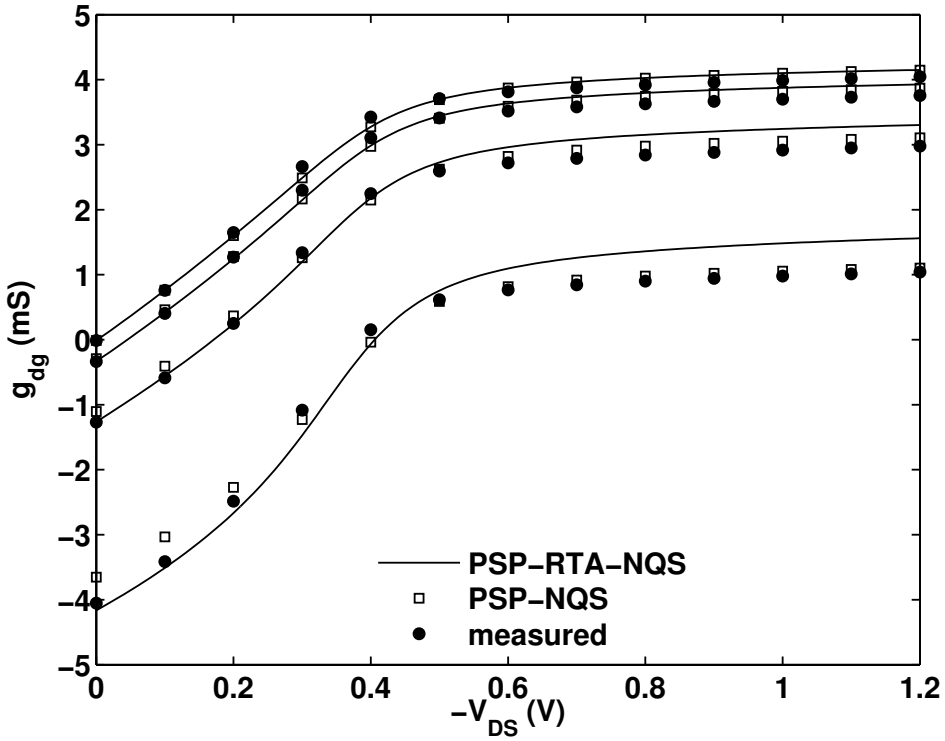

Fig. 3.22. Comparison of model and measured data for a PMOS g_{dg} when V_{GS} = -0.8 V. Frequencies are 0.1, 0.5, 1 and 2 GHz where $f_{\mathrm{T}} = 0.71$ GHz. $L = 1.2$ μm, $W = 10$ μm.

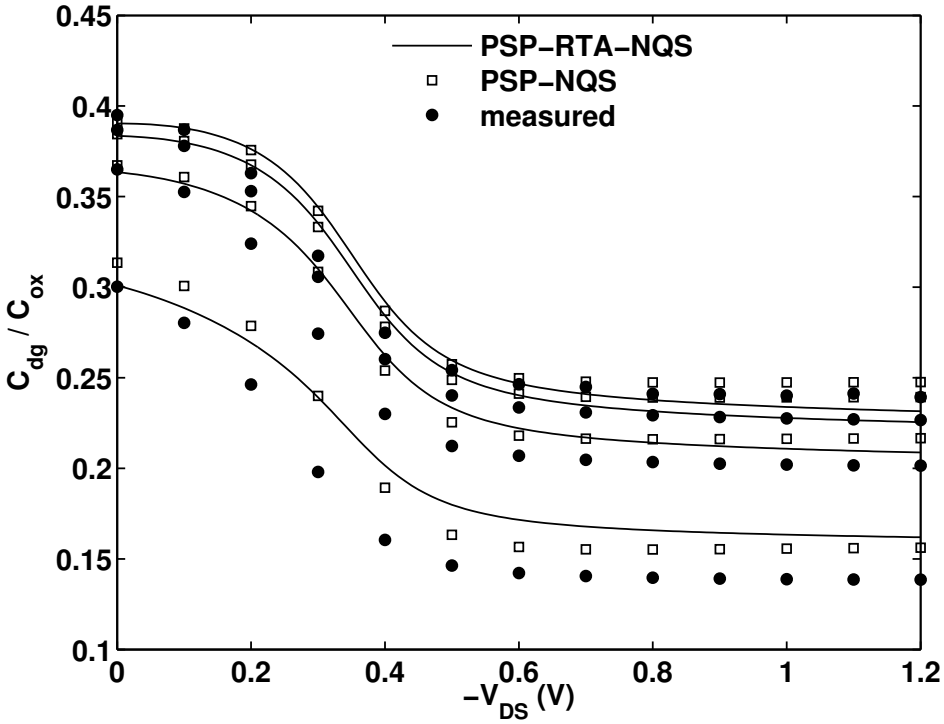

Fig. 3.23. Comparison of model and measured data for a PMOS C_{dg} when V_{GS} = -0.8 V. Frequencies are 0.1, 0.5, 1 and 2 GHz where $f_{\mathrm{T}} = 0.71$ GHz. $L = 1.2$ μm, $W = 10$ μm.

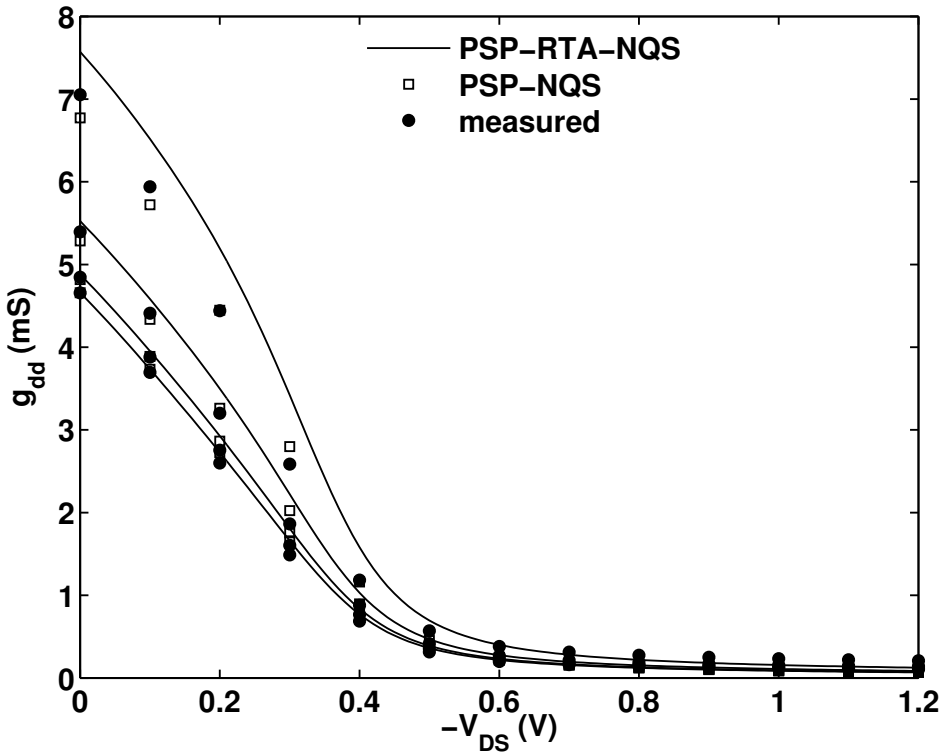

Fig. 3.24. Comparison of model and measured data for a PMOS g_{dd} when V_{GS} = -0.8 V. Frequencies are 0.1, 0.5, 1 and 2 GHz where f_{T} = 0.71 GHz. L = 1.2 μm, W = 10 μm.

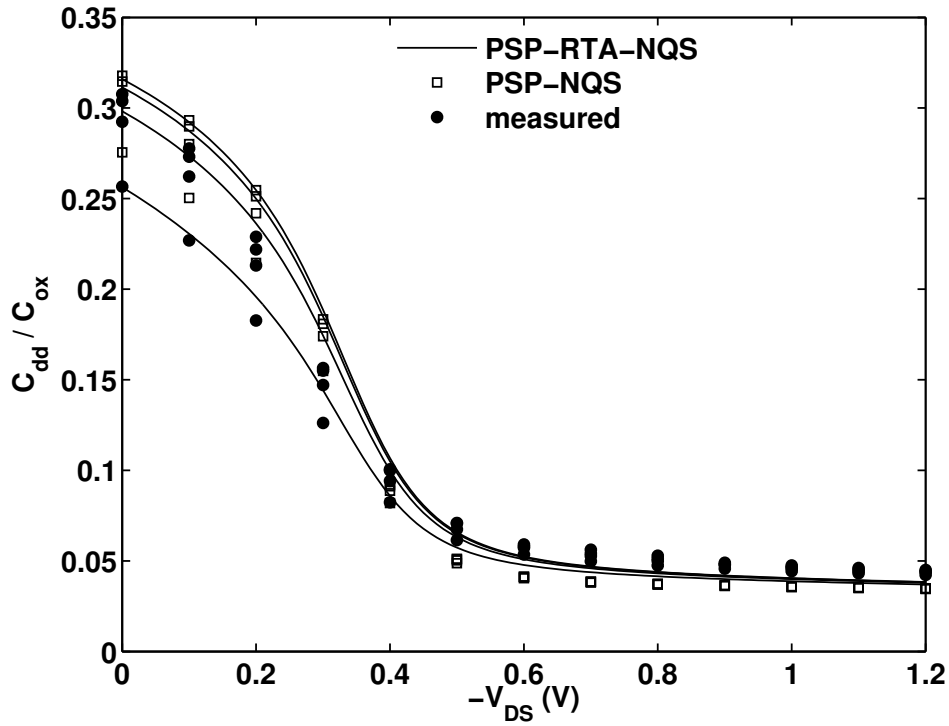

Fig. 3.25. Comparison of model and measured data for a PMOS C_{dd} when V_{GS} = -0.8 V. Frequencies are 0.1, 0.5, 1 and 2 GHz where $f_{\mathrm{T}} = 0.71$ GHz. $L = 1.2$ μm, $W = 10$ μm.

Figs. 3.26 through 3.33 are the fitted frequency and drain bias dependance of conductances and normalized capacitances when $V_{\mathrm{GS}} = -0.9$V.

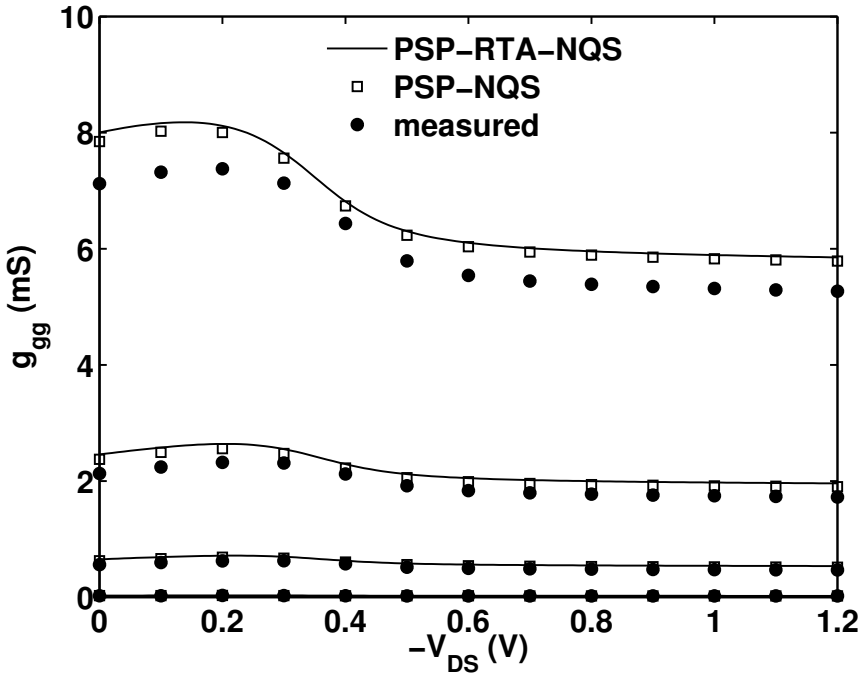

Fig. 3.26. Comparison of model and measured data for a PMOS g_{gg} when V_{GS} = -0.9 V. Frequencies are 0.1, 0.5, 1 and 2 GHz where $f_{\mathrm{T}} = 0.71$ GHz. $L = 1.2$ μm, $W = 10$ μm.

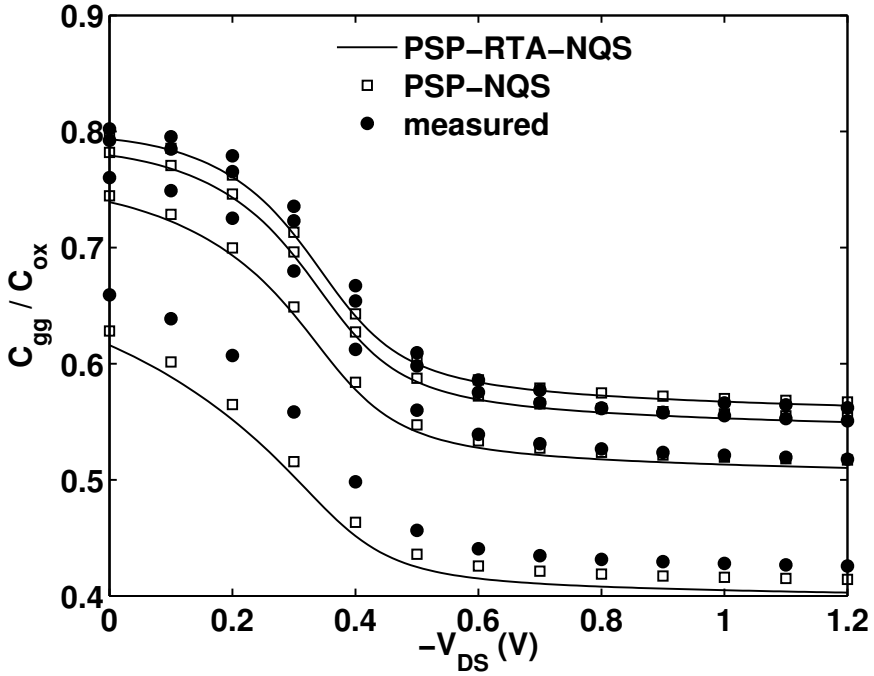

Fig. 3.27. Comparison of model and measured data for a PMOS C_{gg} when V_{GS} = -0.9 V. Frequencies are 0.1, 0.5, 1 and 2 GHz where f_{T} = 0.71 GHz. L = 1.2 μm, W = 10 μm.

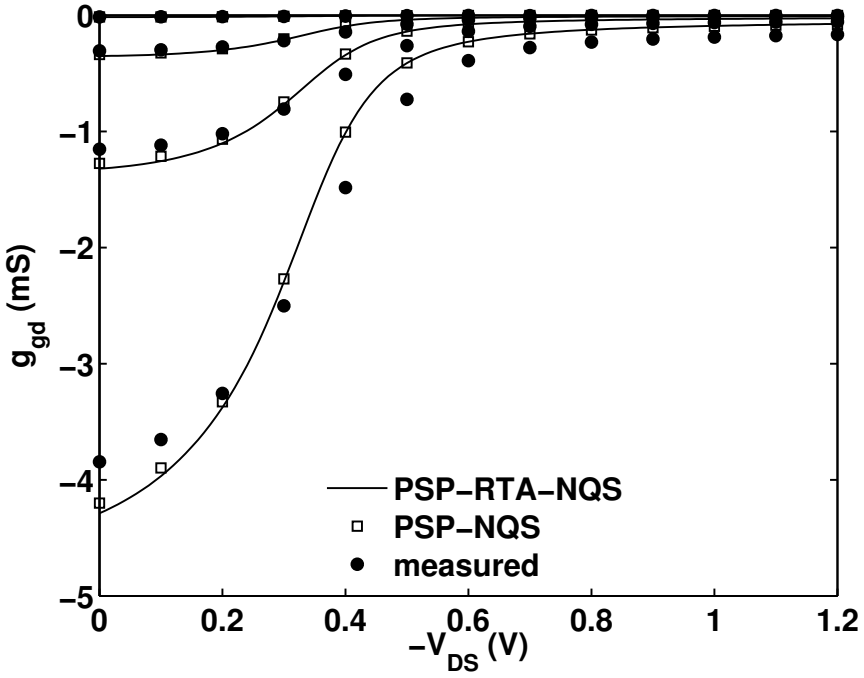

Fig. 3.28. Comparison of model and measured data for a PMOS g_{gd} when V_{GS} = -0.9 V. Frequencies are 0.1, 0.5, 1 and 2 GHz where $f_{\mathrm{T}} = 0.71$ GHz. $L = 1.2$ μm, $W = 10$ μm.

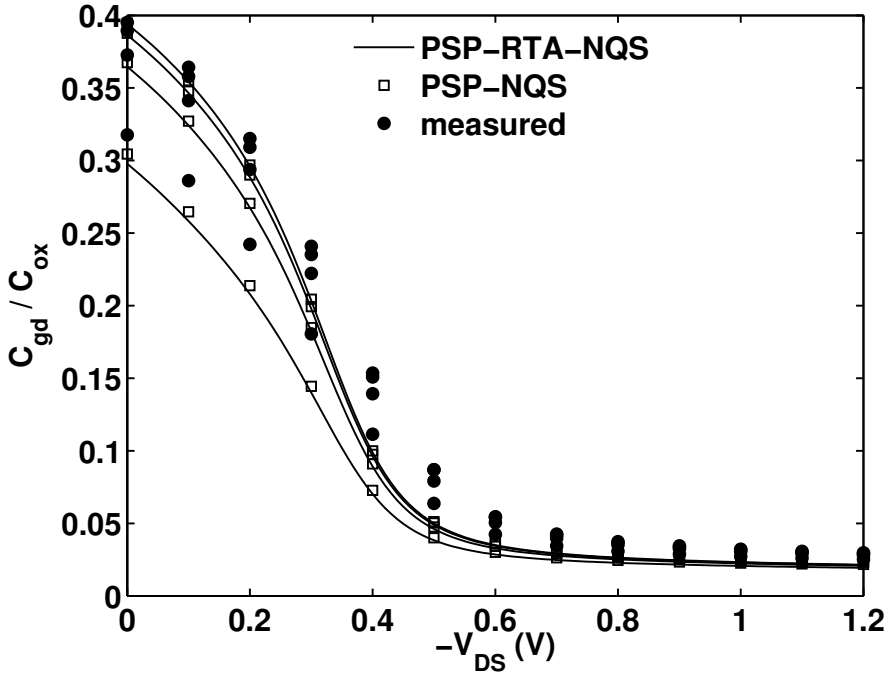

Fig. 3.29. Comparison of model and measured data for a PMOS C_{gd} when V_{GS} = -0.9 V. Frequencies are 0.1, 0.5, 1 and 2 GHz where f_{T} = 0.71 GHz. L = 1.2 μm, W = 10 μm.

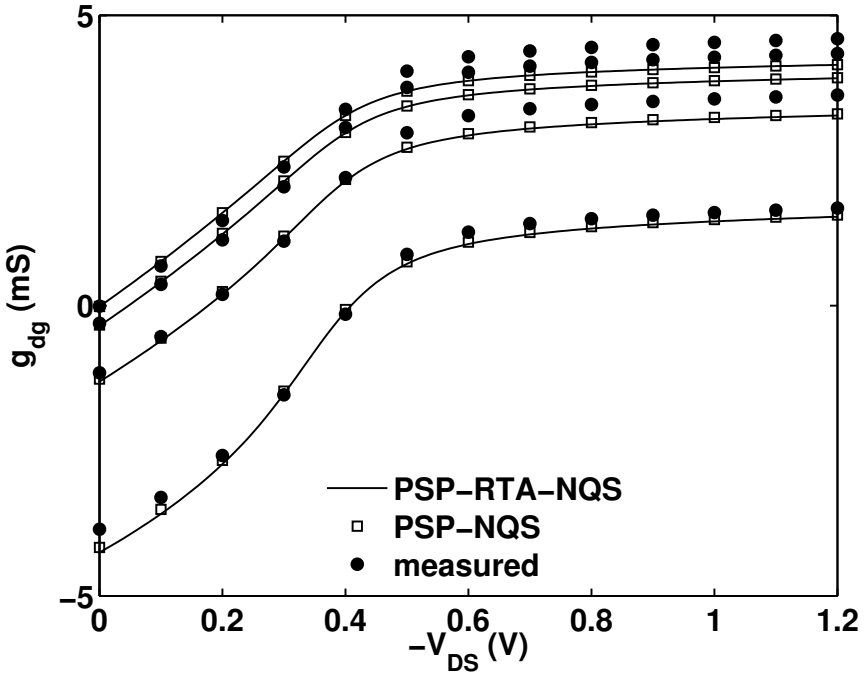

Fig. 3.30. Comparison of model and measured data for a PMOS g_{dg} when V_{GS} = -0.9 V. Frequencies are 0.1, 0.5, 1 and 2 GHz where f_{T} = 0.71 GHz. L = 1.2 μm, W = 10 μm.

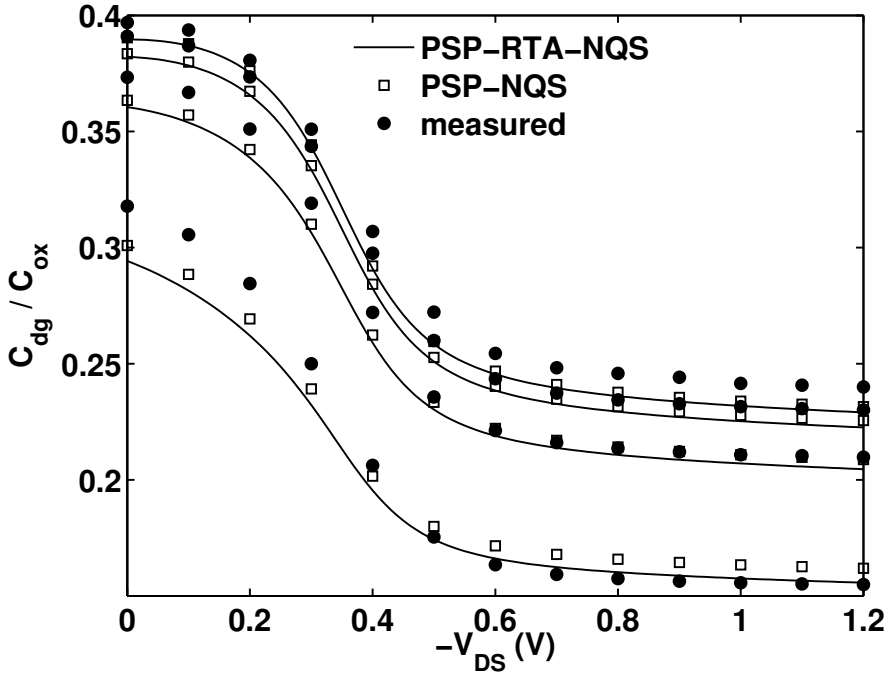

Fig. 3.31. Comparison of model and measured data for a PMOS C_{dg} when V_{GS} = -0.9 V. Frequencies are 0.1, 0.5, 1 and 2 GHz where f_{T} = 0.71 GHz. L = 1.2 μm, W = 10 μm.

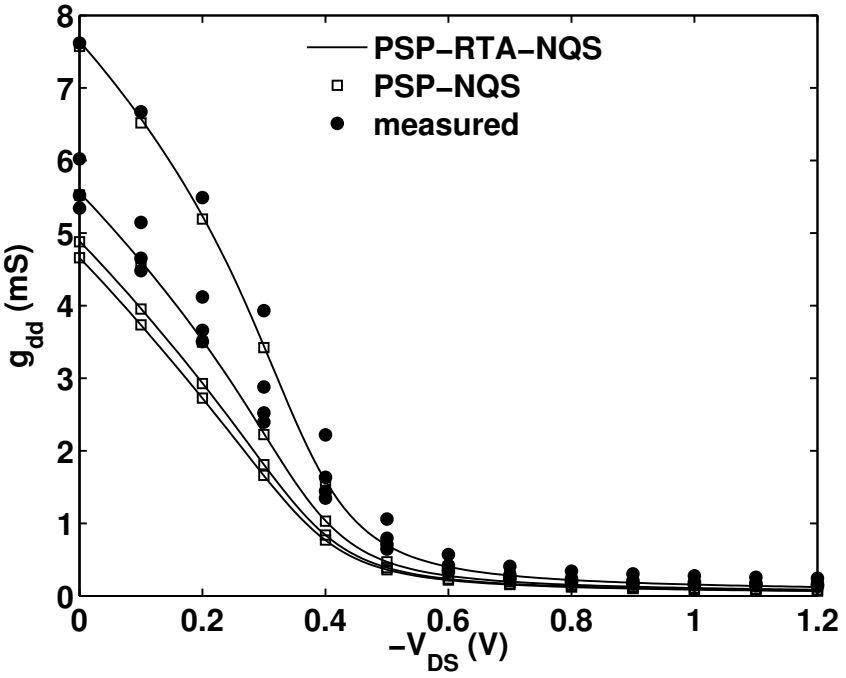

Fig. 3.32. Comparison of model and measured data for a PMOS g_{dd} when V_{GS} = -0.9 V. Frequencies are 0.1, 0.5, 1 and 2 GHz where f_{T} = 0.71 GHz. L = 1.2 μm, W = 10 μm.

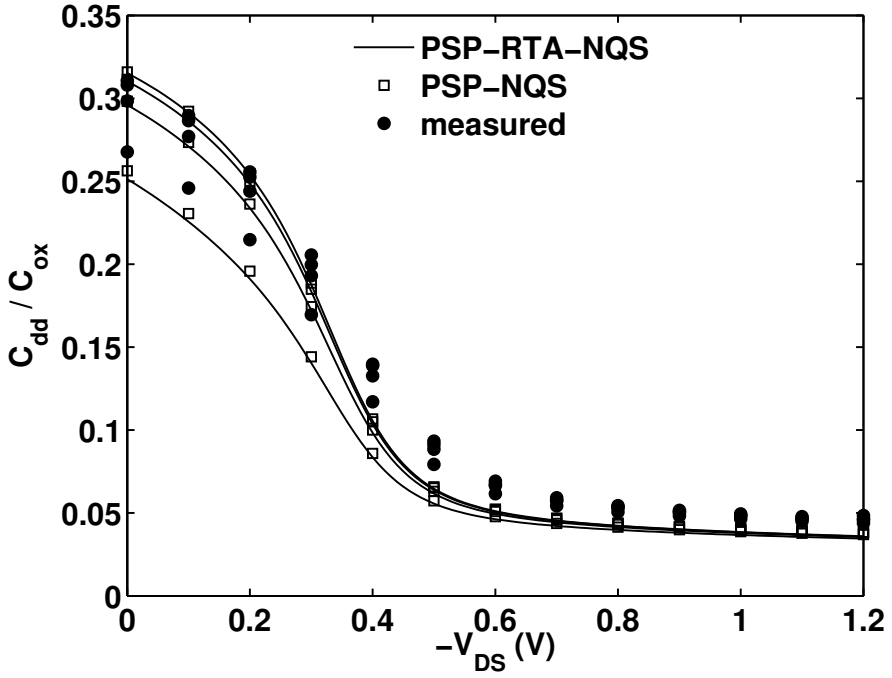

Fig. 3.33. Comparison of model and measured data for a PMOS C_{dd} when V_{GS} = -0.9 V. Frequencies are 0.1, 0.5, 1 and 2 GHz where f_{T} = 0.71 GHz. L = 1.2 μm, W = 10 μm.

3.3. Parameter Extraction for RTA-Based NQS MOSFET Models

It is interesting to mention that the fitting results in Sec. 3.2 not only complete the model validation but also suggest a physical extraction methodology for an advanced RTA-based NQS model. In fact, high frequency MOS transistor behavior is also affected by the gate resistance R_{gate} [5]. In this section, we present a technique to self-consistently determine both K_{drift} in (2.3) and R_{gate} from measured data; the approach uses bias dependent $Q_{\text{i}}^{(0)}$ and effective mobility μ as computed by the PSP model.

3.3.1. Analysis

The RTA-based model introduces a relaxation time that in strong inversion is

$$\tau_{\text{nqs}} = \frac{\tau_0}{K_{\text{drift}}}, \quad \tau_0 = \frac{L^2}{12\mu Q_{\text{i}}^{(0)}} \tag{3.1}$$

For a MOSFET in strong inversion with $V_{\text{BS}} = 0$ the y-parameter matrix accounting for NQS effects in the relaxation time approximation to first order is

$$\begin{bmatrix} y_{\text{gg}} & y_{\text{gd}} \\ y_{\text{dg}} & y_{\text{dd}} \end{bmatrix} = \frac{1}{p_1} \begin{bmatrix} j\omega[C_{\text{gs}}^{(0)} p_2 + C_{\text{gd}}^{(0)} p_3 + C_{\text{gb}}^{(0)} p_1] & -j\omega C_{\text{gd}}^{(0)} p_3 \\ g_{\text{m}}^{(0)} - j\omega C_{\text{gd}}^{(0)} p_3 & g_{\text{sd}}^{(0)} + j\omega(C_{\text{gd}}^{(0)} + C_{\text{bd}}^{(0)}) p_3 \end{bmatrix} \tag{3.2}$$

where $p_1 = 1 + j\omega\tau_1$, $p_2 = 1 + j\omega\tau_2$, and $p_3 = 1 + j\omega\tau_3$; the symbols have their usual meaning, the superscript (0) denotes the quasi-equilibrium value, and the time constants $\tau_{[123]}$, defined in [1], are V_{DS} dependent factors multiplied by τ_0. The simplest terms in (3.2) to analyze are clearly y_{dg} and y_{gd}. The latter is small in saturation, so is not reliably measurable there, however $C_{\text{dg}}^{(0)}$ is large and easily measurable for all drain biases. In particular, it has a maximum at $V_{\text{DS}} = 0$ and at

that bias $g_{\mathrm{m}}^{(0)} = 0$. Extraction of NQS effects from measured data is therefore most easily and directly done by analyzing y_{dg} for $V_{\mathrm{DS}} = 0$.

Both real and imaginary parts of y_{dg} as a function of ω could be used for NQS behavior characterization (although $\mathrm{Re}(y_{\mathrm{dg}}^{(0)}) = 0$ for $V_{\mathrm{DS}} = 0$, at higher frequencies capacitive currents "bleed over" into the real components of all y-parameters, giving them a characteristic ω^2 dependence). From measurement, the imaginary component has the cleanest behavior, and it is also the easiest to analyze. Including the effect of R_{gate} gives

$$C_{\mathrm{dg}} = -\frac{\mathrm{Im}(y_{\mathrm{dg}})}{\omega} = \frac{C_{\mathrm{dg}}^{(0)}}{1 + \tau_{\mathrm{eff}}^2 \omega^2} + O(\omega^4) \tag{3.3}$$

where $\tau_{\mathrm{eff}} = \tau_{\mathrm{nqs}} + R_{\mathrm{gate}} C_{\mathrm{gg}}$ is a function of V_{GS} (through both μ and $Q_{\mathrm{i}}^{(0)}$ in (3.1)). Rearranging gives

$$\frac{C_{\mathrm{dg}}^{(0)}}{C_{\mathrm{dg}}} - 1 = \tau_{\mathrm{eff}}^2 \omega^2 \tag{3.4}$$

and this is the basic relationship we use to determine the NQS and R_{gate} parameters.

3.3.2. Extraction Algorithm

From C_{dg} at $V_{\mathrm{DS}} = 0$ over V_{GS} and ω, at each V_{GS}, extrapolation of $1/C_{\mathrm{dg}}$ vs. ω^2 to $\omega = 0$ gives $1/C_{\mathrm{dg}}^{(0)}$. V_{GS} should be where the device is reasonably into strong inversion and ω should be from well below f_{T} (so extrapolation to determine $C_{\mathrm{dg}}^{(0)}$ is accurate) to roughly $2f_{\mathrm{T}}$ (for higher frequencies higher order terms make (3.3) and (3.4) inaccurate). Knowing $C_{\mathrm{dg}}^{(0)}$, from (3.4) regression of $C_{\mathrm{dg}}^{(0)}/C_{\mathrm{dg}} - 1$ on ω^2 gives τ_{eff} as a function of V_{GS} (cf. Fig. 3.34).

In modern technologies with low supply voltages MOS transistors never reach very strong inversion operation, so the assumption that $Q_{\mathrm{i}}^{(0)} = V_{\mathrm{GS}} - V_{\mathrm{T}}$ is not

accurate, and mobility μ is not constant but depends on V_{GS}. In addition, the RTA NQS model (3.1) is applied to PSP [53] and not to an approximate, simple analytical model; NQS parameters should therefore be extracted to be consistent with $\mu Q_{\mathrm{i}}^{(0)}$ as modeled by PSP. By calculating $\mu Q_{\mathrm{i}}^{(0)}$ from PSP, with parameters extracted to fit dc and low frequency capacitance data, τ_0 in (3.1) can be computed and then from

$$\tau_{\mathrm{eff}} = R_{\mathrm{gate}} C_{\mathrm{gg}}^{(0)} + \frac{\tau_0(V_{\mathrm{GS}})}{K_{\mathrm{drift}}} \tag{3.5}$$

R_{gate} and K_{drift} can be determined from the intercept and reciprocal of the slope of τ_{eff} vs. τ_0 (with $C_{\mathrm{gg}}^{(0)}$ extrapolated from the measured data at the highest V_{GS}; as V_{GS} increases C_{gg} approaches $C_{\mathrm{gg}}^{(0)}$ irrespective of frequency).

3.3.3. Experimental Results

Fig. 3.35 shows a plot of τ_{eff} vs. τ_0 for a $W/L = 10\mu\mathrm{m}/1.2\mu\mathrm{m}$ pMOS transistor in a 90nm RFCMOS technology; the extracted parameter values are $R_{\mathrm{gate}} = 5.9\Omega$ and $K_{\mathrm{drift}} = 0.959$ (which indicates that the underlying NQS model is quite accurate, if it were perfect then K_{drift} should equal 1 exactly). It is apparent that our analysis leads to a highly linear relationship, and the extracted value of R_{gate} is close to the value of 5.54Ω determined from brute force nonlinear least-squares optimization [5] to gate capacitance at $V_{\mathrm{DS}} = 0$ over V_{GS} and frequency. If a constant mobility and $Q_{\mathrm{i}}^{(0)} = V_{\mathrm{GS}} - V_{\mathrm{T}}$ are assumed the extracted value of R_{gate} is 10.3Ω, which is significantly in error.

In this section, we have presented a new and simple technique to characterize NQS and R_{gate} MOS model parameters from measured data. $\mu Q_{\mathrm{i}}^{(0)}$ from PSP is used

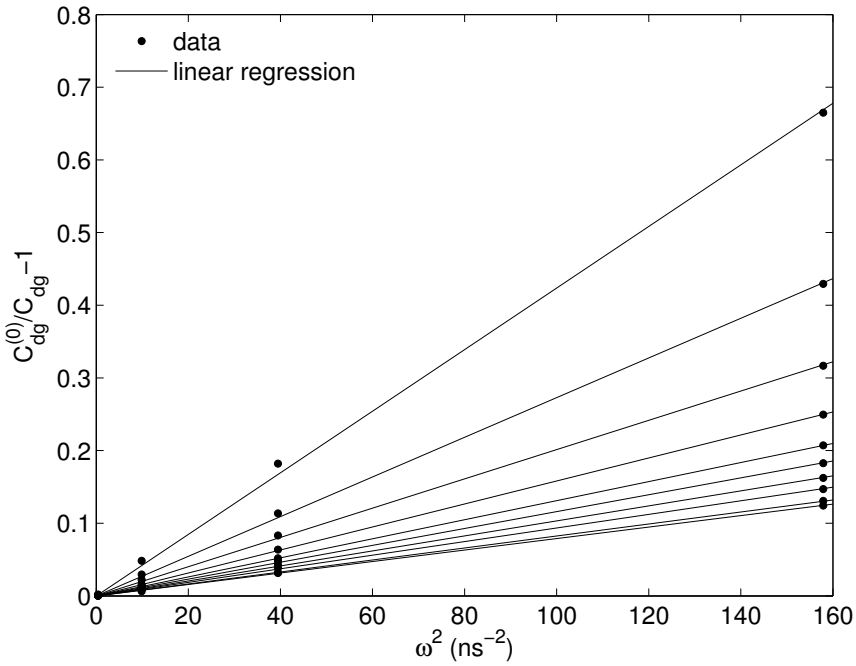

Fig. 3.34. Extracted and modeled $C_{\mathrm{dg}}^{(0)}/C_{\mathrm{dg}} - 1$, pMOS transistor; $V_{\mathrm{DS}} = 0$, V_{SG}=1.5V, f=0.1, 0.5, 1.0, 2.0GHz.

both to ensure consistency between the extracted parameters and the model they will be used for and to avoid the assumptions that mobility is constant and $Q_{\mathrm{i}}^{(0)} = V_{\mathrm{GS}} - V_{\mathrm{T}}$, which are inaccurate for modern devices. As far as we are aware, this is the first procedure reported for self-consistent direct extraction of NQS relaxation time and R_{gate} parameters.

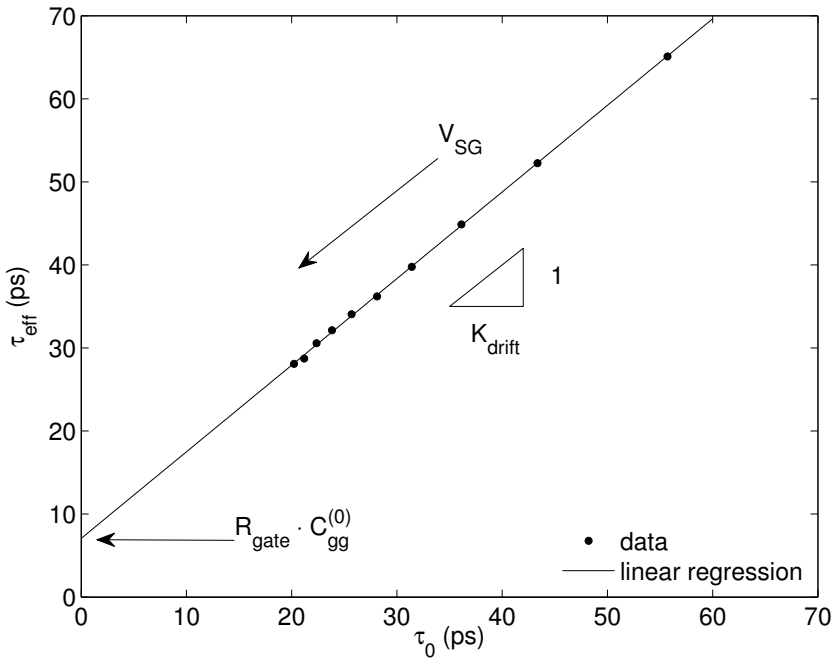

Fig. 3.35. Extracted and modeled effective NQS relaxation times, pMOS transistor; $V_{\mathrm{DS}} = 0$, V_{SG}=0.6 to 1.5V by 0.1V top right to bottom left.

CHAPTER 4

Small-Signal Model

4.1. Small-Signal RTA-Based NQS Model

Practical applications of NQS models rely on the large-signal formulation, which is the one implemented directly in circuit simulators. The small-signal model is provided directly by the circuit simulator by linearization of the large-signal model. Nevertheless, there are some situations where it is advantageous to have an analytical small-signal model. The small-signal model derived in this chapter is particularly useful to perform an RF benchmark test on NQS MOSFET models.

4.1.1. Model Formulation and Terminal Charges

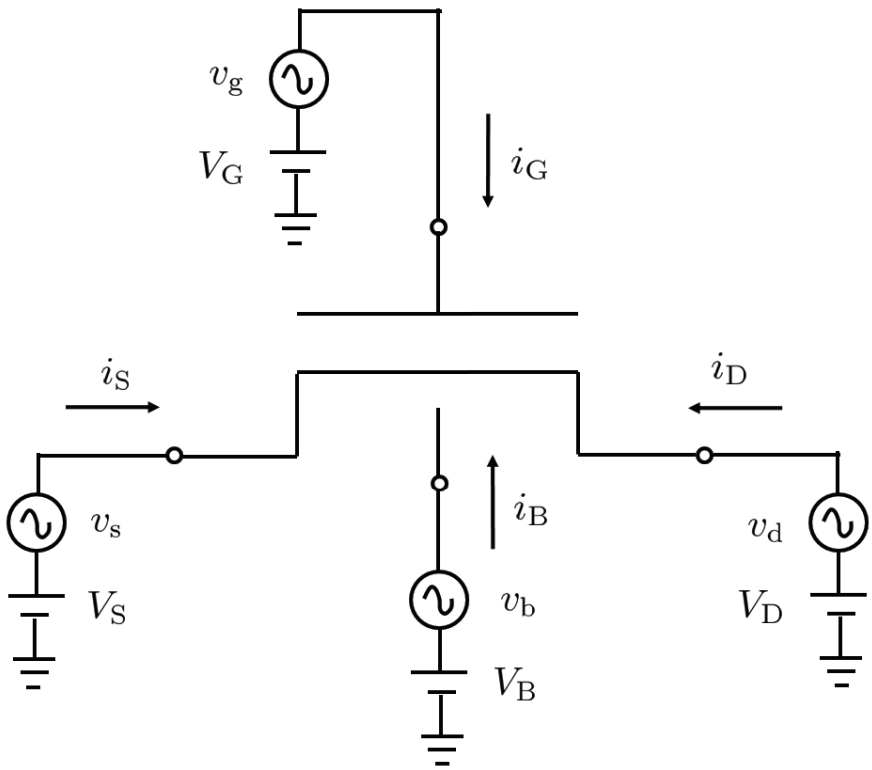

Fig. 4.1. Intrinsic MOSFET with dc biases and small-signal voltages.

Let us consider a MOSFET driven by a dc bias and small-signal excitation

at each terminal, as shown in Fig. 4.1. One could assume that the small-signal voltages are sinusoids and consider the corresponding small-signal terminal currents. However, the algebra turns out to be unnecessarily complicated. We will thus follow, instead, a standard practice and consider a fictitious complex exponential excitation [1,89–91,151]. Thus, the small signal voltages, charges, and currents are given by (j $\in$ { d, g, s, b}):

$$v_{\mathrm{j}}(t) = \mathrm{Re}\left(\Delta v_{\mathrm{j}} e^{i\omega t}\right) \tag{4.1a}$$

$$q_{\mathrm{j}}(t) = \mathrm{Re}\left(\Delta q_{\mathrm{j}} e^{i\omega t}\right) \tag{4.1b}$$

$$i_{\mathrm{j}}(t) = \mathrm{Re}\left(\Delta i_{\mathrm{j}} e^{i\omega t}\right) \tag{4.1c}$$

where Δv_{j} denotes the complex amplitude and ω is the angular frequency. Similarly, Δq_{j} and $\Delta i_{\mathrm{j}} = i\omega\Delta q_{\mathrm{j}}$ denote the complex amplitudes of the corresponding charges and terminal currents. We also use

$$q_{\mathrm{i}} = q_{\mathrm{s}} + q_{\mathrm{d}} = \mathrm{Re}\left(\Delta q_{\mathrm{i}} e^{i\omega t}\right) \tag{4.2}$$

where

$$\Delta q_{\mathrm{i}} = \Delta q_{\mathrm{s}} + \Delta q_{\mathrm{d}} \tag{4.3}$$

From (2.1)

$$\Delta q_{\mathrm{j}} = \frac{\Delta q_{\mathrm{j}}^{(0)}}{1 + i\omega\tau};\ \mathrm{j} \in \{\mathrm{s,\ d,\ i}\} \tag{4.4}$$

where $\Delta q_{\mathrm{j}}^{(0)}$ denotes the QS value of Δq_{j}. Just as (2.1), (4.4) does not apply for j = g or j = b. Instead, we use the linearized form of (2.6)

$$\Delta q_{\mathrm{g}} = C_{\mathrm{ox}} \cdot (\Delta v_{\mathrm{gb}} - \Delta\overline{\psi_{\mathrm{S}}}) \tag{4.5}$$

where $\Delta\overline{\psi_{\mathrm{S}}}$ is the surface potential phasor and the linearized form of (2.17)

$$C_{\mathrm{ox}} \cdot \left(\Delta v_{\mathrm{gb}} - \Delta\overline{\psi_{\mathrm{S}}}\right) + \Delta q_{\mathrm{i}} + \Delta q_{\mathrm{b}} = 0 \tag{4.6}$$

Here, according to (2.11) and (2.15)

$$\Delta q_{\mathrm{b}}/C_{\mathrm{ox}} = -\xi \cdot \Delta\overline{\psi_{\mathrm{S}}} \tag{4.7}$$

where

$$\xi = \frac{\mathrm{sgn}(\overline{\psi_{\mathrm{S}}})\,\gamma\,\beta^{1/2}\,\left[1 - \exp(-\beta\overline{\psi_{\mathrm{S}}})\right]}{2\sqrt{\exp(-\beta\overline{\psi_{\mathrm{S}}}) + \beta\overline{\psi_{\mathrm{S}}} - 1}} \tag{4.8}$$

The validity of (4.7) is based on the fact that the response of the majority carriers (and hence of q_{B}) to the surface potential is, essentially, instantaneous.

From (4.6) and (4.7)

$$\Delta\overline{\psi_{\mathrm{S}}} = \frac{\Delta v_{\mathrm{gb}} + \Delta q_{\mathrm{i}}/C_{\mathrm{ox}}}{1+\xi} \tag{4.9}$$

and

$$\Delta q_{\mathrm{g}} = (1-\eta) \cdot \Delta v_{\mathrm{gb}} \cdot C_{\mathrm{ox}} - \eta \cdot \Delta q_{\mathrm{i}} \tag{4.10}$$

where

$$\eta = \frac{1}{1+\xi} \tag{4.11}$$

With reference to (4.4)

$$\Delta q_{\mathrm{g}} = (1-\eta) \cdot \Delta v_{\mathrm{gb}} \cdot C_{\mathrm{ox}} - \frac{\eta \cdot \Delta q_{\mathrm{i}}^{(0)}}{1+i\omega\tau} \tag{4.12}$$

while from the neutrality condition $\Delta q_{\mathrm{b}} = -\Delta q_{\mathrm{i}} - \Delta q_{\mathrm{g}}$ or

$$\Delta q_{\mathrm{b}} = -(1-\eta) \cdot \left[\Delta v_{\mathrm{gb}} \cdot C_{\mathrm{ox}} + \frac{\Delta q_{\mathrm{i}}^{(0)}}{1+i\omega\tau}\right] \tag{4.13}$$

So far, we have formulated the small-signal RTA-based NQS MOSFET model. The terminal charges are summarized in Table 4.1.

TABLE 4.1
SMALL-SIGNAL TERMINAL CHARGES

Terminal Charge	Equation
Δq_{d}	(4.4)
Δq_{s}	(4.4)
Δq_{g}	(4.12)
Δq_{b}	(4.13)

4.1.2. y-Parameters

Denoting

$$g_{\mathrm{jk}} = \mathrm{Re}(y_{\mathrm{jk}}) \tag{4.14}$$

and

$$c_{\mathrm{jk}} = \frac{\mathrm{Im}(y_{\mathrm{jk}})}{\omega \cdot C_{\mathrm{ox}}} \tag{4.15}$$

we have

$$y_{\mathrm{jk}} = g_{\mathrm{jk}} + i\omega C_{\mathrm{ox}} c_{\mathrm{jk}} \tag{4.16}$$

with these notations, the traditionally defined transcapacitances become

$$C_{\mathrm{jk}} = (2\delta_{\mathrm{jk}} - 1) \cdot c_{\mathrm{jk}} \cdot C_{\mathrm{ox}} \tag{4.17}$$

In terms of complex amplitudes,

$$y_{\mathrm{jk}} = g_{\mathrm{jk}}^{(0)} + i\omega \Delta q_{\mathrm{j}}\big|_{\Delta v_{\mathrm{m}} = \delta_{\mathrm{mk}}} \tag{4.18}$$

whereas

$$g_{\mathrm{jk}} = g_{\mathrm{jk}}^{(0)} - \omega \mathrm{Im}\left(\Delta q_{\mathrm{j}}\big|_{\Delta v_{\mathrm{m}} = \delta_{\mathrm{mk}}}\right) \tag{4.19}$$

$$c_{\mathrm{jk}} = \frac{1}{C_{\mathrm{ox}}} \mathrm{Re}(\Delta q_{\mathrm{j}}\big|_{\Delta v_{\mathrm{m}} = \delta_{\mathrm{mk}}}) \tag{4.20}$$

In what follows, we present detailed derivation of y_{gg} and y_{bb}. The remaining elements of the y-matrix will be discussed in a more condensed manner.

Starting with (4.16)

$$y_{\mathrm{gg}} = g_{\mathrm{gg}} + i\omega C_{\mathrm{ox}} c_{\mathrm{gg}} \tag{4.21}$$

where from (4.19) and (4.20)

$$g_{\mathrm{gg}} = g_{\mathrm{gg}}^{(0)} - \omega \cdot \mathrm{Im}\left(\Delta q_{\mathrm{g}}\big|_{\Delta v_{\mathrm{m}}=\delta_{\mathrm{mg}}}\right) \tag{4.22}$$

$$c_{\mathrm{gg}} = \frac{1}{C_{\mathrm{ox}}}\mathrm{Re}\left(\Delta q_{\mathrm{g}}\big|_{\Delta v_{\mathrm{m}}=\delta_{\mathrm{mg}}}\right) \tag{4.23}$$

Substituting Δq_{g} from (4.12)

$$g_{\mathrm{gg}} = g_{\mathrm{gg}}^{(0)} - \eta \cdot \Delta q_{\mathrm{i}}^{(0)} \cdot \frac{\omega^2 \tau}{1 + (\omega\tau)^2} \tag{4.24}$$

$$c_{\mathrm{gg}} = (1 - \eta) - \frac{\eta}{C_{\mathrm{ox}}} \cdot \Delta q_{\mathrm{i}}^{(0)} \cdot \frac{1}{1 + (\omega\tau)^2} \tag{4.25}$$

Substituting

$$\Delta q_{\mathrm{i}}^{(0)} = c_{\mathrm{ig}}^{(0)} C_{\mathrm{ox}} \Delta v_{\mathrm{g}} = c_{\mathrm{ig}}^{(0)} C_{\mathrm{ox}} \tag{4.26}$$

and assuming the steady-state gate tunneling current is negligible

$$g_{\mathrm{gg}}^{(0)} = \frac{\partial I_{\mathrm{G}}}{\partial V_{\mathrm{G}}} = 0 \tag{4.27}$$

yield

$$g_{\mathrm{gg}} = -\eta \cdot c_{\mathrm{ig}}^{(0)} \cdot C_{\mathrm{ox}} \cdot \frac{\omega^2 \tau}{1 + (\omega\tau)^2} \tag{4.28}$$

$$c_{\mathrm{gg}} = (1 - \eta) - \eta \cdot c_{\mathrm{ig}}^{(0)} \cdot \frac{1}{1 + (\omega\tau)^2} \tag{4.29}$$

To evaluate y_{bb}, we start with

$$y_{\mathrm{bb}} = g_{\mathrm{bb}} + i\omega C_{\mathrm{ox}} c_{\mathrm{bb}} \tag{4.30}$$

where

$$g_{\mathrm{bb}} = g_{\mathrm{bb}}^{(0)} - \omega \cdot \mathrm{Im}\left(\Delta q_{\mathrm{b}}\big|_{\Delta v_{\mathrm{m}}=\delta_{\mathrm{mb}}}\right) \tag{4.31}$$

$$c_{\mathrm{bb}} = \frac{1}{C_{\mathrm{ox}}}\mathrm{Re}\left(\Delta q_{\mathrm{b}}\big|_{\Delta v_{\mathrm{m}}=\delta_{\mathrm{mb}}}\right) \tag{4.32}$$

Substituting the expression for Δq_{b} from (4.13)

$$g_{\mathrm{bb}} = \omega \cdot (1-\eta) \cdot \Delta q_{\mathrm{i}}^{(0)} \cdot \mathrm{Im}\left(\frac{1}{1+i\omega\tau}\right) \tag{4.33}$$

$$c_{\mathrm{bb}} = -\frac{1-\eta}{C_{\mathrm{ox}}} \cdot \left[-C_{\mathrm{ox}} + \Delta q_{\mathrm{i}}^{(0)}\mathrm{Re}\left(\frac{1}{1+i\omega\tau}\right)\right] \tag{4.34}$$

Substituting

$$\Delta q_{\mathrm{i}}^{(0)} = c_{\mathrm{ig}}^{(0)} C_{\mathrm{ox}} \Delta v_{\mathrm{b}} = c_{\mathrm{ib}}^{(0)} C_{\mathrm{ox}} \tag{4.35}$$

and assuming the steady-state bulk tunneling current is negligible

$$g_{\mathrm{bb}}^{(0)} = \frac{\partial I_{\mathrm{B}}}{\partial V_{\mathrm{B}}} = 0 \tag{4.36}$$

yield

$$g_{\mathrm{bb}} = -(1-\eta) \cdot c_{\mathrm{ib}}^{(0)} \cdot \frac{\omega^2 \tau C_{\mathrm{ox}}}{1+(\omega\tau)^2} \tag{4.37}$$

$$c_{\mathrm{bb}} = (1-\eta) \cdot \left[1 - \frac{c_{\mathrm{ib}}^{(0)}}{1+(\omega\tau)^2}\right] \tag{4.38}$$

To evaluate y_{dd}, from (4.16)

$$y_{\mathrm{dd}} = g_{\mathrm{dd}} + i\omega C_{\mathrm{ox}} c_{\mathrm{dd}} \tag{4.39}$$

where from (4.19)

$$
\begin{aligned}
g_{\mathrm{dd}} &= g_{\mathrm{dd}}^{(0)} - \omega \cdot \mathrm{Im}\left(\Delta q_{\mathrm{d}}\big|_{\Delta v_{\mathrm{m}}=\delta_{\mathrm{md}}}\right) \\
&= g_{\mathrm{dd}}^{(0)} - \omega \cdot \Delta q_{\mathrm{d}}^{(0)}\big|_{\Delta v_{\mathrm{m}}=\delta_{\mathrm{md}}} \cdot \mathrm{Im}\left(\frac{1}{1+i\omega\tau}\right) \\
&= g_{\mathrm{dd}}^{(0)} + \Delta q_{\mathrm{d}}^{(0)}\big|_{\Delta v_{\mathrm{m}}=\delta_{\mathrm{md}}} \cdot \frac{\omega^2\tau}{1+(\omega\tau)^2} \\
&= g_{\mathrm{dd}}^{(0)} + c_{\mathrm{dd}}^{(0)} \cdot \frac{\omega^2\tau C_{\mathrm{ox}}}{1+(\omega\tau)^2}
\end{aligned} \tag{4.40}
$$

Here,

$$
g_{\mathrm{dd}}^{(0)} = \frac{\partial I_{\mathrm{D}}}{\partial V_{\mathrm{D}}} \tag{4.41}
$$

From (4.20)

$$
\begin{aligned}
c_{\mathrm{dd}} &= \frac{1}{C_{\mathrm{ox}}}\mathrm{Re}\left(\Delta q_{\mathrm{d}}\big|_{\Delta v_{\mathrm{m}}=\delta_{\mathrm{md}}}\right) \\
&= \frac{1}{C_{\mathrm{ox}}}\Delta q_{\mathrm{d}}^{(0)}\big|_{\Delta v_{\mathrm{m}}=\delta_{\mathrm{md}}}\mathrm{Re}\left(\frac{1}{1+i\omega\tau}\right) \\
&= \frac{1}{C_{\mathrm{ox}}}\Delta q_{\mathrm{d}}^{(0)}\big|_{\Delta v_{\mathrm{m}}=\delta_{\mathrm{md}}} \cdot \frac{1}{1+(\omega\tau)^2} \\
&= \frac{c_{\mathrm{dd}}^{(0)}}{1+(\omega\tau)^2}
\end{aligned} \tag{4.42}
$$

Then, we evaluate y_{gd} from (4.16)

$$
y_{\mathrm{gd}} = g_{\mathrm{gd}} + i\omega C_{\mathrm{ox}} c_{\mathrm{gd}} \tag{4.43}
$$

where from (4.12) and (4.19)

$$
\begin{aligned}
g_{\mathrm{gd}} &= g_{\mathrm{gd}}^{(0)} - \omega \cdot \mathrm{Im}\left(\Delta q_{\mathrm{g}}\big|_{\Delta v_{\mathrm{m}}=\delta_{\mathrm{md}}}\right) \qquad (4.44)\\
&= g_{\mathrm{gd}}^{(0)} - \omega \cdot \mathrm{Im}\left[\frac{(1-\eta)\cdot \Delta v_{\mathrm{gb}} \cdot C_{\mathrm{ox}} - \eta \cdot \Delta q_{\mathrm{i}}}{\Delta v_{\mathrm{d}}}\right]\\
&= g_{\mathrm{gd}}^{(0)} + \omega \cdot \eta \cdot \mathrm{Im}\left(\Delta q_{\mathrm{i}}\big|_{\Delta v_{\mathrm{m}}=\delta_{\mathrm{md}}}\right)\\
&= g_{\mathrm{gd}}^{(0)} + \omega \cdot \eta \cdot \Delta q_{\mathrm{i}}^{(0)}\big|_{\Delta v_{\mathrm{m}}=\delta_{\mathrm{md}}} \cdot \mathrm{Im}\left(\frac{1}{1+i\omega\tau}\right)\\
&= g_{\mathrm{gd}}^{(0)} - \eta \cdot \Delta q_{\mathrm{i}}^{(0)}\big|_{\Delta v_{\mathrm{m}}=\delta_{\mathrm{md}}} \cdot \frac{\omega^2\tau}{1+(\omega\tau)^2}\\
&= g_{\mathrm{gd}}^{(0)} - \eta \cdot c_{\mathrm{id}}^{(0)} \cdot \frac{\omega^2\tau C_{\mathrm{ox}}}{1+(\omega\tau)^2} \qquad (4.45)
\end{aligned}
$$

Recalling that

$$
g_{\mathrm{gd}}^{(0)} = \frac{\partial I_{\mathrm{G}}}{\partial V_{\mathrm{D}}} = 0 \qquad (4.46)
$$

we find

$$
g_{\mathrm{gd}} = -\eta \cdot c_{\mathrm{id}}^{(0)} \cdot \frac{\omega^2\tau C_{\mathrm{ox}}}{1+(\omega\tau)^2} \qquad (4.47)
$$

From (4.12) and (4.20)

$$
\begin{aligned}
c_{\mathrm{gd}} &= \frac{1}{C_{\mathrm{ox}}}\mathrm{Re}\left(\Delta q_{\mathrm{g}}\big|_{\Delta v_{\mathrm{m}}=\delta_{\mathrm{md}}}\right)\\
&= \frac{1}{C_{\mathrm{ox}}}\mathrm{Re}\left[\frac{(1-\eta)\cdot \Delta v_{\mathrm{gb}} \cdot C_{\mathrm{ox}} - \eta \cdot \Delta q_{\mathrm{i}}}{\Delta v_{\mathrm{d}}}\right]\\
&= -\frac{\eta}{C_{\mathrm{ox}}} \cdot \mathrm{Re}\left(\Delta q_{\mathrm{i}}\big|_{\Delta v_{\mathrm{m}}=\delta_{\mathrm{md}}}\right)\\
&= -\frac{\eta}{C_{\mathrm{ox}}} \cdot \Delta q_{\mathrm{i}}^{(0)}\big|_{\Delta v_{\mathrm{m}}=\delta_{\mathrm{md}}} \cdot \frac{1}{1+(\omega\tau)^2}\\
&= -\frac{\eta \cdot c_{\mathrm{id}}^{(0)}}{1+(\omega\tau)^2} \qquad (4.48)
\end{aligned}
$$

Next, we evaluate y_{sd} from (4.16)

$$
y_{\mathrm{sd}} = g_{\mathrm{sd}} + i\omega C_{\mathrm{ox}} c_{\mathrm{sd}} \qquad (4.49)
$$

where from (4.4) and (4.19)

$$
\begin{aligned}
g_{\mathrm{sd}} &= g_{\mathrm{sd}}^{(0)} - \omega \cdot \mathrm{Im}\left(\Delta q_{\mathrm{s}}\big|_{\Delta v_{\mathrm{m}}=\delta_{\mathrm{md}}}\right) \\
&= g_{\mathrm{sd}}^{(0)} - \omega \cdot \Delta q_{\mathrm{s}}^{(0)}\big|_{\Delta v_{\mathrm{m}}=\delta_{\mathrm{md}}} \cdot \mathrm{Im}\left(\frac{1}{1+i\omega\tau}\right) \\
&= g_{\mathrm{sd}}^{(0)} + \Delta q_{\mathrm{s}}^{(0)}\big|_{\Delta v_{\mathrm{m}}=\delta_{\mathrm{md}}} \cdot \frac{\omega^2\tau}{1+(\omega\tau)^2} \\
&= g_{\mathrm{sd}}^{(0)} + c_{\mathrm{sd}}^{(0)} \cdot \frac{\omega^2\tau C_{\mathrm{ox}}}{1+(\omega\tau)^2}
\end{aligned}
\tag{4.50}
$$

From (4.4) and (4.20)

$$
\begin{aligned}
C_{\mathrm{sd}} &= \mathrm{Re}\left(\Delta q_{\mathrm{s}}\big|_{\Delta v_{\mathrm{m}}=\delta_{\mathrm{md}}}\right) \\
&= \Delta q_{\mathrm{s}}^{(0)}\big|_{\Delta v_{\mathrm{m}}=\delta_{\mathrm{md}}} \mathrm{Re}\left(\frac{1}{1+i\omega\tau}\right) \\
&= \Delta q_{\mathrm{s}}^{(0)}\big|_{\Delta v_{\mathrm{m}}=\delta_{\mathrm{md}}} \cdot \frac{1}{1+(\omega\tau)^2} \\
&= c_{\mathrm{sd}}^{(0)} \cdot \frac{C_{\mathrm{ox}}}{1+(\omega\tau)^2}
\end{aligned}
\tag{4.51}
$$

It is followed by the evaluation of y_{bd}. From (4.16)

$$
y_{\mathrm{bd}} = g_{\mathrm{bd}} + i\omega C_{\mathrm{ox}} c_{\mathrm{bd}} \tag{4.52}
$$

where from (4.13) and (4.19)

$$
\begin{aligned}
g_{\mathrm{bd}} &= g_{\mathrm{bd}}^{(0)} - \omega \cdot \mathrm{Im}\left(\Delta q_{\mathrm{b}}\big|_{\Delta v_{\mathrm{m}}=\delta_{\mathrm{md}}}\right) && (4.53) \\
&= g_{\mathrm{bd}}^{(0)} - \omega \cdot \mathrm{Im}\left[\frac{-(1-\eta)\cdot(\Delta v_{\mathrm{gb}} \cdot C_{\mathrm{ox}} + \Delta q_{\mathrm{i}})}{\Delta v_{\mathrm{d}}}\right] \\
&= g_{\mathrm{bd}}^{(0)} + \omega \cdot (1-\eta) \cdot \mathrm{Im}\left(\Delta q_{\mathrm{i}}\big|_{\Delta v_{\mathrm{m}}=\delta_{\mathrm{md}}}\right) \\
&= g_{\mathrm{bd}}^{(0)} + \omega \cdot (1-\eta) \cdot \Delta q_{\mathrm{i}}^{(0)}\big|_{\Delta v_{\mathrm{m}}=\delta_{\mathrm{md}}} \cdot \mathrm{Im}\left[\left(\frac{1}{1+i\omega\tau}\right)\right] \\
&= g_{\mathrm{bd}}^{(0)} - (1-\eta) \cdot \Delta q_{\mathrm{i}}^{(0)}\big|_{\Delta v_{\mathrm{m}}=\delta_{\mathrm{md}}} \cdot \frac{\omega^2\tau}{1+(\omega\tau)^2} \\
&= g_{\mathrm{bd}}^{(0)} - (1-\eta) \cdot c_{\mathrm{id}}^{(0)} \cdot \frac{\omega^2\tau C_{\mathrm{ox}}}{1+(\omega\tau)^2} && (4.54)
\end{aligned}
$$

Recalling that

$$g_{\mathrm{bd}}^{(0)} = \frac{\partial I_{\mathrm{B}}}{\partial V_{\mathrm{D}}} = 0 \tag{4.55}$$

we find

$$g_{\mathrm{bd}} = -(1-\eta) \cdot c_{\mathrm{id}}^{(0)} \cdot \frac{\omega^2 \tau C_{\mathrm{ox}}}{1+(\omega\tau)^2} \tag{4.56}$$

Also from (4.20)

$$\begin{aligned}
c_{\mathrm{bd}} &= \frac{1}{C_{\mathrm{ox}}} \mathrm{Re}\left(\Delta q_{\mathrm{b}}\big|_{\Delta v_{\mathrm{m}}=\delta_{\mathrm{md}}}\right) \\
&= \frac{1}{C_{\mathrm{ox}}} \mathrm{Re}\left[\frac{-(1-\eta)\cdot(\Delta v_{\mathrm{gb}} \cdot C_{\mathrm{ox}} + \Delta q_{\mathrm{i}})}{\Delta v_{\mathrm{d}}}\right] \\
&= -\frac{1-\eta}{C_{\mathrm{ox}}} \cdot \mathrm{Re}\left(\Delta q_{\mathrm{i}}\big|_{\Delta v_{\mathrm{m}}=\delta_{\mathrm{md}}}\right) \\
&= -\frac{1-\eta}{C_{\mathrm{ox}}} \cdot \Delta q_{\mathrm{i}}^{(0)}\big|_{\Delta v_{\mathrm{m}}=\delta_{\mathrm{md}}} \cdot \frac{1}{1+(\omega\tau)^2} \\
&= -\frac{(1-\eta)\cdot c_{\mathrm{id}}^{(0)}}{1+(\omega\tau)^2}
\end{aligned} \tag{4.57}$$

To evaluate y_{dg} from (4.16)

$$y_{\mathrm{dg}} = g_{\mathrm{dg}} + i\omega C_{\mathrm{ox}} c_{\mathrm{dg}} \tag{4.58}$$

where from (4.4) and (4.19)

$$\begin{aligned}
g_{\mathrm{dg}} &= g_{\mathrm{dg}}^{(0)} - \omega \cdot \mathrm{Im}\left(\Delta q_{\mathrm{d}}\big|_{\Delta v_{\mathrm{m}}=\delta_{\mathrm{mg}}}\right) \\
&= g_{\mathrm{dg}}^{(0)} - \omega \cdot \Delta q_{\mathrm{d}}^{(0)}\big|_{\Delta v_{\mathrm{m}}=\delta_{\mathrm{mg}}} \cdot \mathrm{Im}\left(\frac{1}{1+i\omega\tau}\right) \\
&= g_{\mathrm{dg}}^{(0)} + \Delta q_{\mathrm{d}}^{(0)}\big|_{\Delta v_{\mathrm{m}}=\delta_{\mathrm{mg}}} \cdot \frac{\omega^2\tau}{1+(\omega\tau)^2} \\
&= g_{\mathrm{dg}}^{(0)} + c_{\mathrm{dg}}^{(0)} \cdot \frac{\omega^2 \tau C_{\mathrm{ox}}}{1+(\omega\tau)^2}
\end{aligned} \tag{4.59}$$

From (4.4) and (4.20)

$$
\begin{aligned}
c_{\mathrm{dg}} &= \frac{1}{C_{\mathrm{ox}}}\mathrm{Re}\left(\Delta q_{\mathrm{d}}\big|_{\Delta v_{\mathrm{m}}=\delta_{\mathrm{mg}}}\right) \\
&= \frac{1}{C_{\mathrm{ox}}}\Delta q_{\mathrm{d}}^{(0)}\big|_{\Delta v_{\mathrm{m}}=\delta_{\mathrm{mg}}}\mathrm{Re}\left(\frac{1}{1+i\omega\tau}\right) \\
&= \frac{1}{C_{\mathrm{ox}}}\Delta q_{\mathrm{d}}^{(0)}\big|_{\Delta v_{\mathrm{m}}=\delta_{\mathrm{mg}}}\cdot\frac{1}{1+(\omega\tau)^2} \\
&= \frac{c_{\mathrm{dg}}^{(0)}}{1+(\omega\tau)^2}
\end{aligned}
\tag{4.60}
$$

Similarly, we evaluate y_{sg} from (4.16)

$$
y_{\mathrm{sg}} = g_{\mathrm{sg}} + i\omega C_{\mathrm{ox}} c_{\mathrm{sg}} \tag{4.61}
$$

where from (4.4) and (4.19)

$$
\begin{aligned}
g_{\mathrm{sg}} &= g_{\mathrm{sg}}^{(0)} - \omega\cdot\mathrm{Im}\left(\Delta q_{\mathrm{s}}\big|_{\Delta v_{\mathrm{m}}=\delta_{\mathrm{mg}}}\right) \\
&= g_{\mathrm{sg}}^{(0)} - \omega\cdot\Delta q_{\mathrm{s}}^{(0)}\big|_{\Delta v_{\mathrm{m}}=\delta_{\mathrm{mg}}}\cdot\mathrm{Im}\left(\frac{1}{1+i\omega\tau}\right) \\
&= g_{\mathrm{sg}}^{(0)} + \Delta q_{\mathrm{s}}^{(0)}\big|_{\Delta v_{\mathrm{m}}=\delta_{\mathrm{mg}}}\cdot\frac{\omega^2\tau}{1+(\omega\tau)^2} \\
&= g_{\mathrm{sg}}^{(0)} + c_{\mathrm{sg}}^{(0)}\cdot\frac{\omega^2\tau C_{\mathrm{ox}}}{1+(\omega\tau)^2}
\end{aligned}
\tag{4.62}
$$

From (4.4) and (4.20)

$$
\begin{aligned}
c_{\mathrm{sg}} &= \frac{1}{C_{\mathrm{ox}}}\mathrm{Re}\left(\Delta q_{\mathrm{s}}\big|_{\Delta v_{\mathrm{m}}=\delta_{\mathrm{mg}}}\right) \\
&= \frac{1}{C_{\mathrm{ox}}}\Delta q_{\mathrm{s}}^{(0)}\big|_{\Delta v_{\mathrm{m}}=\delta_{\mathrm{mg}}}\mathrm{Re}\left(\frac{1}{1+i\omega\tau}\right) \\
&= \frac{1}{C_{\mathrm{ox}}}\Delta q_{\mathrm{s}}^{(0)}\big|_{\Delta v_{\mathrm{m}}=\delta_{\mathrm{mg}}}\cdot\frac{1}{1+(\omega\tau)^2} \\
&= \frac{c_{\mathrm{sg}}^{(0)}}{1+(\omega\tau)^2}
\end{aligned}
\tag{4.63}
$$

It is followed by the evaluation of y_{bg} from (4.16)

$$
y_{\mathrm{bg}} = g_{\mathrm{bg}} + i\omega C_{\mathrm{ox}} c_{\mathrm{bg}} \tag{4.64}
$$

where from (4.13) and (4.19)

$$
\begin{aligned}
g_{\mathrm{bg}} &= g_{\mathrm{bg}}^{(0)} - \omega \cdot \mathrm{Im}\left(\Delta q_{\mathrm{b}}\big|_{\Delta v_{\mathrm{m}}=\delta_{\mathrm{mg}}}\right) \qquad (4.65)\\
&= g_{\mathrm{bg}}^{(0)} - \omega \cdot \mathrm{Im}\left[\frac{-(1-\eta)\cdot(\Delta v_{\mathrm{gb}}\cdot C_{\mathrm{ox}} + \Delta q_{\mathrm{i}})}{\Delta v_{\mathrm{g}}}\right]\\
&= g_{\mathrm{bg}}^{(0)} + \omega \cdot (1-\eta)\cdot \mathrm{Im}\left(\Delta q_{\mathrm{i}}\big|_{\Delta v_{\mathrm{m}}=\delta_{\mathrm{mg}}}\right)\\
&= g_{\mathrm{bg}}^{(0)} + \omega \cdot (1-\eta)\cdot \Delta q_{\mathrm{i}}^{(0)}\big|_{\Delta v_{\mathrm{m}}=\delta_{\mathrm{mg}}} \cdot \mathrm{Im}\left(\frac{1}{1+i\omega\tau}\right)\\
&= g_{\mathrm{bg}}^{(0)} - (1-\eta)\cdot \Delta q_{\mathrm{i}}^{(0)}\big|_{\Delta v_{\mathrm{m}}=\delta_{\mathrm{mg}}} \cdot \frac{\omega^2\tau}{1+(\omega\tau)^2}\\
&= g_{\mathrm{bg}}^{(0)} - (1-\eta)\cdot c_{\mathrm{ig}}^{(0)} \cdot \frac{\omega^2\tau C_{\mathrm{ox}}}{1+(\omega\tau)^2} \qquad (4.66)
\end{aligned}
$$

From (4.4) and (4.20)

$$
\begin{aligned}
c_{\mathrm{bg}} &= \frac{1}{C_{\mathrm{ox}}}\mathrm{Re}\left(\Delta q_{\mathrm{b}}\big|_{\Delta v_{\mathrm{m}}=\delta_{\mathrm{mg}}}\right)\\
&= \frac{1}{C_{\mathrm{ox}}}\mathrm{Re}\left[\frac{-(1-\eta)\cdot(\Delta v_{\mathrm{gb}}\cdot C_{\mathrm{ox}} + \Delta q_{\mathrm{i}})}{\Delta v_{\mathrm{g}}}\right]\\
&= -\frac{1-\eta}{C_{\mathrm{ox}}}\cdot\left[C_{\mathrm{ox}} + \mathrm{Re}\left(\Delta q_{\mathrm{i}}\big|_{\Delta v_{\mathrm{m}}=\delta_{\mathrm{mg}}}\right)\right]\\
&= -\frac{1-\eta}{C_{\mathrm{ox}}}\cdot\left[C_{\mathrm{ox}} + \Delta q_{\mathrm{i}}^{(0)}\big|_{\Delta v_{\mathrm{m}}=\delta_{\mathrm{mg}}} \cdot \frac{1}{1+(\omega\tau)^2}\right]\\
&= -(1-\eta)\cdot\left[1 + \frac{c_{\mathrm{ig}}^{(0)}}{1+(\omega\tau)^2}\right] \qquad (4.67)
\end{aligned}
$$

In the next we evaluate y_{ds} from (4.16)

$$
y_{\mathrm{ds}} = g_{\mathrm{ds}} + i\omega C_{\mathrm{ox}} c_{\mathrm{ds}} \qquad (4.68)
$$

where from (4.4) and (4.19)

$$
\begin{aligned}
g_{\mathrm{ds}} &= g_{\mathrm{ds}}^{(0)} - \omega \cdot \mathrm{Im}\left(\Delta q_{\mathrm{d}}\big|_{\Delta v_{\mathrm{m}}=\delta_{\mathrm{ms}}}\right) \\
&= g_{\mathrm{ds}}^{(0)} - \omega \cdot \Delta q_{\mathrm{d}}^{(0)}\big|_{\Delta v_{\mathrm{m}}=\delta_{\mathrm{ms}}} \cdot \mathrm{Im}\left(\frac{1}{1+i\omega\tau}\right) \\
&= g_{\mathrm{ds}}^{(0)} + \Delta q_{\mathrm{d}}^{(0)}\big|_{\Delta v_{\mathrm{m}}=\delta_{\mathrm{ms}}} \cdot \frac{\omega^2\tau}{1+(\omega\tau)^2} \\
&= g_{\mathrm{ds}}^{(0)} + c_{\mathrm{ds}}^{(0)} \cdot \frac{\omega^2\tau C_{\mathrm{ox}}}{1+(\omega\tau)^2}
\end{aligned} \tag{4.69}
$$

From (4.4) and (4.20)

$$
\begin{aligned}
c_{\mathrm{ds}} &= \mathrm{Re}\left(\Delta q_{\mathrm{d}}\big|_{\Delta v_{\mathrm{m}}=\delta_{\mathrm{ms}}}\right) \\
&= \frac{1}{C_{\mathrm{ox}}}\Delta q_{\mathrm{d}}^{(0)}\big|_{\Delta v_{\mathrm{m}}=\delta_{\mathrm{ms}}} \mathrm{Re}\left(\frac{1}{1+i\omega\tau}\right) \\
&= \frac{1}{C_{\mathrm{ox}}}\Delta q_{\mathrm{d}}^{(0)}\big|_{\Delta v_{\mathrm{m}}=\delta_{\mathrm{ms}}} \cdot \frac{1}{1+(\omega\tau)^2} \\
&= \frac{c_{\mathrm{ds}}^{(0)}}{1+(\omega\tau)^2}
\end{aligned} \tag{4.70}
$$

Then, we evaluate y_{gs} from (4.16)

$$
y_{\mathrm{gs}} = g_{\mathrm{gs}} + i\omega C_{\mathrm{ox}} c_{\mathrm{gs}} \tag{4.71}
$$

where from (4.4) and (4.19)

$$
\begin{aligned}
g_{\mathrm{gs}} &= g_{\mathrm{gs}}^{(0)} - \omega \cdot \mathrm{Im}\left(\Delta q_{\mathrm{g}}\big|_{\Delta v_{\mathrm{m}}=\delta_{\mathrm{ms}}}\right) && (4.72) \\
&= g_{\mathrm{gs}}^{(0)} - \omega \cdot \mathrm{Im}\left[\frac{(1-\eta)\cdot\Delta v_{\mathrm{gb}}\cdot C_{\mathrm{ox}} - \eta\cdot\Delta q_{\mathrm{i}}}{\Delta v_{\mathrm{s}}}\right] \\
&= g_{\mathrm{gs}}^{(0)} + \omega \cdot \eta \cdot \mathrm{Im}\left(\Delta q_{\mathrm{i}}\big|_{\Delta v_{\mathrm{m}}=\delta_{\mathrm{ms}}}\right) \\
&= g_{\mathrm{gs}}^{(0)} + \omega \cdot \eta \cdot \Delta q_{\mathrm{i}}^{(0)}\big|_{\Delta v_{\mathrm{m}}=\delta_{\mathrm{ms}}} \cdot \mathrm{Im}\left(\frac{1}{1+i\omega\tau}\right) \\
&= g_{\mathrm{gs}}^{(0)} - \eta \cdot \Delta q_{\mathrm{i}}^{(0)}\big|_{\Delta v_{\mathrm{m}}=\delta_{\mathrm{ms}}} \cdot \frac{\omega^2\tau}{1+(\omega\tau)^2} \\
&= g_{\mathrm{gs}}^{(0)} - \eta \cdot c_{\mathrm{is}}^{(0)} \cdot \frac{\omega^2\tau C_{\mathrm{ox}}}{1+(\omega\tau)^2} && (4.73)
\end{aligned}
$$

Recalling that

$$g_{\mathrm{gs}}^{(0)} = \frac{\partial I_{\mathrm{G}}}{\partial V_{\mathrm{S}}} = 0 \tag{4.74}$$

we find

$$g_{\mathrm{gs}} = -\eta \cdot c_{\mathrm{is}}^{(0)} \cdot \frac{\omega^2 \tau C_{\mathrm{ox}}}{1 + (\omega\tau)^2} \tag{4.75}$$

From (4.4) and (4.20)

$$\begin{aligned}
c_{\mathrm{gs}} &= \frac{1}{C_{\mathrm{ox}}} \mathrm{Re}\left(\Delta q_{\mathrm{g}}\big|_{\Delta v_{\mathrm{m}}=\delta_{\mathrm{ms}}}\right) \\
&= \frac{1}{C_{\mathrm{ox}}} \mathrm{Re}\left[\frac{(1-\eta)\cdot \Delta v_{\mathrm{gb}} \cdot C_{\mathrm{ox}} - \eta \cdot \Delta q_{\mathrm{i}}}{\Delta v_{\mathrm{s}}}\right] \\
&= -\frac{\eta}{C_{\mathrm{ox}}} \cdot \mathrm{Re}\left(\Delta q_{\mathrm{i}}\big|_{\Delta v_{\mathrm{m}}=\delta_{\mathrm{ms}}}\right) \\
&= -\frac{\eta}{C_{\mathrm{ox}}} \cdot \Delta q_{\mathrm{i}}^{(0)}\big|_{\Delta v_{\mathrm{m}}=\delta_{\mathrm{ms}}} \cdot \frac{1}{1+(\omega\tau)^2} \\
&= -\frac{\eta \cdot c_{\mathrm{is}}^{(0)}}{1+(\omega\tau)^2}
\end{aligned} \tag{4.76}$$

Similarly, we evaluate y_{ss} from (4.16)

$$y_{\mathrm{ss}} = g_{\mathrm{ss}} + i\omega C_{\mathrm{ox}} c_{\mathrm{ss}} \tag{4.77}$$

where from (4.4) and (4.19)

$$\begin{aligned}
g_{\mathrm{ss}} &= g_{\mathrm{ss}}^{(0)} - \omega \cdot \mathrm{Im}\left(\Delta q_{\mathrm{s}}\big|_{\Delta v_{\mathrm{m}}=\delta_{\mathrm{ms}}}\right) \\
&= g_{\mathrm{ss}}^{(0)} - \omega \cdot \Delta q_{\mathrm{s}}^{(0)}\big|_{\Delta v_{\mathrm{m}}=\delta_{\mathrm{ms}}} \cdot \mathrm{Im}\left(\frac{1}{1+i\omega\tau}\right) \\
&= g_{\mathrm{ss}}^{(0)} + \Delta q_{\mathrm{s}}^{(0)}\big|_{\Delta v_{\mathrm{m}}=\delta_{\mathrm{ms}}} \cdot \frac{\omega^2\tau}{1+(\omega\tau)^2} \\
&= g_{\mathrm{ss}}^{(0)} + c_{\mathrm{ss}}^{(0)} \cdot \frac{\omega^2 \tau C_{\mathrm{ox}}}{1+(\omega\tau)^2}
\end{aligned} \tag{4.78}$$

From (4.4) and (4.20)

$$
\begin{aligned}
c_{\mathrm{ss}} &= \frac{1}{C_{\mathrm{ox}}}\mathrm{Re}\left(\Delta q_{\mathrm{s}}\big|_{\Delta v_{\mathrm{m}}=\delta_{\mathrm{ms}}}\right) \\
&= \frac{1}{C_{\mathrm{ox}}}\Delta q_{\mathrm{s}}^{(0)}\big|_{\Delta v_{\mathrm{m}}=\delta_{\mathrm{ms}}}\mathrm{Re}\left(\frac{1}{1+i\omega\tau}\right) \\
&= \frac{1}{C_{\mathrm{ox}}}\Delta q_{\mathrm{s}}^{(0)}\big|_{\Delta v_{\mathrm{m}}=\delta_{\mathrm{ms}}}\cdot\frac{1}{1+(\omega\tau)^2} \\
&= \frac{c_{\mathrm{ss}}^{(0)}}{1+(\omega\tau)^2} \qquad (4.79)
\end{aligned}
$$

It is followed by the evaluation of y_{bs} from (4.16)

$$
y_{\mathrm{bs}} = g_{\mathrm{bs}} + i\omega C_{\mathrm{ox}} c_{\mathrm{bs}} \qquad (4.80)
$$

where from (4.13) and (4.19)

$$
\begin{aligned}
g_{\mathrm{bs}} &= g_{\mathrm{bs}}^{(0)} - \omega\cdot\mathrm{Im}\left(\Delta q_{\mathrm{b}}\big|_{\Delta v_{\mathrm{m}}=\delta_{\mathrm{ms}}}\right) \qquad (4.81) \\
&= g_{\mathrm{bs}}^{(0)} - \omega\cdot\mathrm{Im}\left[\frac{-(1-\eta)\cdot(\Delta v_{\mathrm{gb}}\cdot C_{\mathrm{ox}}+\Delta q_{\mathrm{i}})}{\Delta v_{\mathrm{s}}}\right] \\
&= g_{\mathrm{bs}}^{(0)} + \omega\cdot(1-\eta)\cdot\mathrm{Im}\left(\Delta q_{\mathrm{i}}\big|_{\Delta v_{\mathrm{m}}=\delta_{\mathrm{ms}}}\right) \\
&= g_{\mathrm{bs}}^{(0)} + \omega\cdot(1-\eta)\cdot\Delta q_{\mathrm{i}}^{(0)}\big|_{\Delta v_{\mathrm{m}}=\delta_{\mathrm{ms}}}\cdot\mathrm{Im}\left(\frac{1}{1+i\omega\tau}\right) \\
&= g_{\mathrm{bs}}^{(0)} - (1-\eta)\cdot\Delta q_{\mathrm{i}}^{(0)}\big|_{\Delta v_{\mathrm{m}}=\delta_{\mathrm{ms}}}\cdot\frac{\omega^2\tau}{1+(\omega\tau)^2} \\
&= g_{\mathrm{bs}}^{(0)} - (1-\eta)\cdot c_{\mathrm{is}}^{(0)}\cdot\frac{\omega^2\tau C_{\mathrm{ox}}}{1+(\omega\tau)^2} \qquad (4.82)
\end{aligned}
$$

Recalling that

$$
g_{\mathrm{bs}}^{(0)} = \frac{\partial I_{\mathrm{B}}}{\partial V_{\mathrm{S}}} = 0 \qquad (4.83)
$$

we find

$$
g_{\mathrm{bs}} = -(1-\eta)\cdot c_{\mathrm{is}}^{(0)}\cdot\frac{\omega^2\tau C_{\mathrm{ox}}}{1+(\omega\tau)^2} \qquad (4.84)
$$

From (4.4) and (4.20)

$$
\begin{aligned}
c_{\mathrm{bs}} &= \frac{1}{C_{\mathrm{ox}}}\mathrm{Re}\left(\Delta q_{\mathrm{b}}\big|_{\Delta v_{\mathrm{m}}=\delta_{\mathrm{ms}}}\right) \\
&= \frac{1}{C_{\mathrm{ox}}}\mathrm{Re}\frac{-(1-\eta)\cdot(\Delta v_{\mathrm{gb}}\cdot C_{\mathrm{ox}}+\Delta q_{\mathrm{i}})}{\Delta v_{\mathrm{s}}} \\
&= -\frac{1-\eta}{C_{\mathrm{ox}}}\cdot\mathrm{Re}\left(\Delta q_{\mathrm{i}}\big|_{\Delta v_{\mathrm{m}}=\delta_{\mathrm{ms}}}\right) \\
&= -\frac{1-\eta}{C_{\mathrm{ox}}}\cdot\Delta q_{\mathrm{i}}^{(0)}\big|_{\Delta v_{\mathrm{m}}=\delta_{\mathrm{ms}}}\cdot\frac{1}{1+(\omega\tau)^2} \\
&= -\frac{(1-\eta)\cdot c_{\mathrm{is}}^{(0)}}{1+(\omega\tau)^2}
\end{aligned}
\tag{4.85}
$$

Then, we evaluate y_{db} from (4.16)

$$
y_{\mathrm{db}} = g_{\mathrm{db}} + i\omega C_{\mathrm{ox}} c_{\mathrm{db}} \tag{4.86}
$$

where from (4.4) and (4.19)

$$
\begin{aligned}
g_{\mathrm{db}} &= g_{\mathrm{db}}^{(0)} - \omega\cdot\mathrm{Im}\left(\Delta q_{\mathrm{d}}\big|_{\Delta v_{\mathrm{m}}=\delta_{\mathrm{mb}}}\right) \\
&= g_{\mathrm{db}}^{(0)} - \omega\cdot\Delta q_{\mathrm{d}}^{(0)}\big|_{\Delta v_{\mathrm{m}}=\delta_{\mathrm{mb}}}\cdot\mathrm{Im}\left(\frac{1}{1+i\omega\tau}\right) \\
&= g_{\mathrm{db}}^{(0)} + \Delta q_{\mathrm{d}}^{(0)}\big|_{\Delta v_{\mathrm{m}}=\delta_{\mathrm{mb}}}\cdot\frac{\omega^2\tau}{1+(\omega\tau)^2} \\
&= g_{\mathrm{db}}^{(0)} + c_{\mathrm{db}}^{(0)}\cdot\frac{\omega^2\tau C_{\mathrm{ox}}}{1+(\omega\tau)^2}
\end{aligned}
\tag{4.87}
$$

From (4.4) and (4.20)

$$
\begin{aligned}
c_{\mathrm{db}} &= \frac{1}{C_{\mathrm{ox}}}\mathrm{Re}\left(\Delta q_{\mathrm{d}}\big|_{\Delta v_{\mathrm{m}}=\delta_{\mathrm{mb}}}\right) \\
&= \frac{1}{C_{\mathrm{ox}}}\Delta q_{\mathrm{d}}^{(0)}\big|_{\Delta v_{\mathrm{m}}=\delta_{\mathrm{mb}}}\mathrm{Re}\left(\frac{1}{1+i\omega\tau}\right) \\
&= \frac{1}{C_{\mathrm{ox}}}\Delta q_{\mathrm{d}}^{(0)}\big|_{\Delta v_{\mathrm{m}}=\delta_{\mathrm{mb}}}\cdot\frac{1}{1+(\omega\tau)^2} \\
&= \frac{c_{\mathrm{db}}^{(0)}}{1+(\omega\tau)^2}
\end{aligned}
\tag{4.88}
$$

After that, we evaluate y_{gb} from (4.16)

$$y_{\mathrm{gb}} = g_{\mathrm{gb}} + i\omega C_{\mathrm{ox}} c_{\mathrm{gb}} \tag{4.89}$$

where from (4.13) and (4.19)

$$\begin{aligned}
g_{\mathrm{gb}} &= g_{\mathrm{gb}}^{(0)} - \omega \cdot \mathrm{Im}\left(\Delta q_{\mathrm{g}}\big|_{\Delta v_{\mathrm{m}}=\delta_{\mathrm{mb}}}\right) \qquad (4.90)\\
&= g_{\mathrm{gb}}^{(0)} - \omega \cdot \mathrm{Im}\left[\frac{(1-\eta)\cdot \Delta v_{\mathrm{gb}} \cdot C_{\mathrm{ox}} - \eta \cdot \Delta q_{\mathrm{i}}}{\Delta v_{\mathrm{b}}}\right]\\
&= g_{\mathrm{gb}}^{(0)} + \omega \cdot \eta \cdot \mathrm{Im}\left(\Delta q_{\mathrm{i}}\big|_{\Delta v_{\mathrm{m}}=\delta_{\mathrm{mb}}}\right)\\
&= g_{\mathrm{gb}}^{(0)} + \omega \cdot \eta \cdot \Delta q_{\mathrm{i}}^{(0)}\big|_{\Delta v_{\mathrm{m}}=\delta_{\mathrm{mb}}} \cdot \mathrm{Im}\left(\frac{1}{1+i\omega\tau}\right)\\
&= g_{\mathrm{gb}}^{(0)} - \eta \cdot \Delta q_{\mathrm{i}}^{(0)}\big|_{\Delta v_{\mathrm{m}}=\delta_{\mathrm{mb}}} \cdot \frac{\omega^2\tau}{1+(\omega\tau)^2}\\
&= g_{\mathrm{gb}}^{(0)} - \eta \cdot c_{\mathrm{ib}}^{(0)} \cdot \frac{\omega^2\tau C_{\mathrm{ox}}}{1+(\omega\tau)^2} \qquad (4.91)
\end{aligned}$$

Recalling that

$$g_{\mathrm{gb}}^{(0)} = \frac{\partial I_{\mathrm{G}}}{\partial V_{\mathrm{B}}} = 0 \tag{4.92}$$

we find

$$g_{\mathrm{gb}} = -\eta \cdot c_{\mathrm{ib}}^{(0)} \cdot \frac{\omega^2\tau C_{\mathrm{ox}}}{1+(\omega\tau)^2} \tag{4.93}$$

From (4.4) and (4.20)

$$\begin{aligned}
c_{\mathrm{gb}} &= \frac{1}{C_{\mathrm{ox}}}\mathrm{Re}\left(\frac{\Delta q_{\mathrm{g}}}{\Delta v_{\mathrm{b}}}\right)\\
&= \frac{1}{C_{\mathrm{ox}}}\mathrm{Re}\left[\frac{(1-\eta)\cdot \Delta v_{\mathrm{gb}} \cdot C_{\mathrm{ox}} - \frac{\eta}{C_{\mathrm{ox}}} \cdot \Delta q_{\mathrm{i}}}{\Delta v_{\mathrm{b}}}\right]\\
&= -(1-\eta) - \frac{\eta}{C_{\mathrm{ox}}} \cdot \mathrm{Re}\left(\Delta q_{\mathrm{i}}\big|_{\Delta v_{\mathrm{m}}=\delta_{\mathrm{mb}}}\right)\\
&= -(1-\eta) - \frac{\eta}{C_{\mathrm{ox}}} \cdot \Delta q_{\mathrm{i}}^{(0)}\big|_{\Delta v_{\mathrm{m}}=\delta_{\mathrm{mb}}} \cdot \frac{1}{1+(\omega\tau)^2}\\
&= -(1-\eta) - \frac{\eta \cdot c_{\mathrm{ib}}^{(0)}}{1+(\omega\tau)^2} \qquad (4.94)
\end{aligned}$$

Similarly, we evaluate y_{sb} from (4.16)

$$y_{\mathrm{sb}} = g_{\mathrm{sb}} + i\omega C_{\mathrm{ox}} c_{\mathrm{sb}} \tag{4.95}$$

where from (4.4) and (4.19)

$$\begin{aligned} g_{\mathrm{sb}} &= g_{\mathrm{sb}}^{(0)} - \omega \cdot \mathrm{Im}\left(\frac{\Delta q_{\mathrm{s}}}{\Delta v_{\mathrm{b}}}\right) \\ &= g_{\mathrm{sb}}^{(0)} - \omega \cdot \Delta q_{\mathrm{s}}^{(0)}\big|_{\Delta v_{\mathrm{m}}=\delta_{\mathrm{mb}}} \cdot \mathrm{Im}\left(\frac{1}{1+i\omega\tau}\right) \\ &= g_{\mathrm{sb}}^{(0)} + \Delta q_{\mathrm{s}}^{(0)}\big|_{\Delta v_{\mathrm{m}}=\delta_{\mathrm{mb}}} \cdot \frac{\omega^2\tau}{1+(\omega\tau)^2} \\ &= g_{\mathrm{sb}}^{(0)} + c_{\mathrm{sb}}^{(0)} \cdot \frac{\omega^2\tau C_{\mathrm{ox}}}{1+(\omega\tau)^2} \end{aligned} \tag{4.96}$$

From (4.4) and (4.20)

$$\begin{aligned} c_{\mathrm{sb}} &= \frac{1}{C_{\mathrm{ox}}}\mathrm{Re}\left(\Delta q_{\mathrm{s}}\big|_{\Delta v_{\mathrm{m}}=\delta_{\mathrm{mb}}}\right) \\ &= \frac{1}{C_{\mathrm{ox}}}\Delta q_{\mathrm{s}}^{(0)}\big|_{\Delta v_{\mathrm{m}}=\delta_{\mathrm{mb}}}\mathrm{Re}\left(\frac{1}{1+i\omega\tau}\right) \\ &= \frac{1}{C_{\mathrm{ox}}}\Delta q_{\mathrm{s}}^{(0)}\big|_{\Delta v_{\mathrm{m}}=\delta_{\mathrm{mb}}} \cdot \frac{1}{1+(\omega\tau)^2} \\ &= \frac{c_{\mathrm{sb}}^{(0)}}{1+(\omega\tau)^2} \end{aligned} \tag{4.97}$$

The evaluated conductances and capacitances can be presented as

$$[g_{\mathrm{jk}}] = \begin{bmatrix} g_{\mathrm{dd}}^{(0)} & g_{\mathrm{dg}}^{(0)} & g_{\mathrm{ds}}^{(0)} & g_{\mathrm{db}}^{(0)} \\ 0 & 0 & 0 & 0 \\ g_{\mathrm{sd}}^{(0)} & g_{\mathrm{sg}}^{(0)} & g_{\mathrm{ss}}^{(0)} & g_{\mathrm{sb}}^{(0)} \\ 0 & 0 & 0 & 0 \end{bmatrix} - k_0 F_\omega \begin{bmatrix} -c_{\mathrm{dd}}^{(0)} & -c_{\mathrm{dg}}^{(0)} & -c_{\mathrm{ds}}^{(0)} & -c_{\mathrm{db}}^{(0)} \\ \eta c_{\mathrm{id}}^{(0)} & \eta c_{\mathrm{ig}}^{(0)} & \eta c_{\mathrm{is}}^{(0)} & \eta c_{\mathrm{ib}}^{(0)} \\ -c_{\mathrm{sd}}^{(0)} & -c_{\mathrm{sg}}^{(0)} & -c_{\mathrm{ss}}^{(0)} & -c_{\mathrm{sb}}^{(0)} \\ \zeta c_{\mathrm{id}}^{(0)} & \zeta c_{\mathrm{ig}}^{(0)} & \zeta c_{\mathrm{is}}^{(0)} & \zeta c_{\mathrm{ib}}^{(0)} \end{bmatrix} \tag{4.98}$$

where $k_0 = \omega^2 \tau C_{\text{ox}}$, $\zeta = 1 - \eta$, $F_\omega = \left[1 + (\omega\tau)^2\right]^{-1}$ and

$$[c_{\text{jk}}] = -F_\omega \begin{bmatrix} -c_{\text{dd}}^{(0)} & -c_{\text{dg}}^{(0)} & -c_{\text{ds}}^{(0)} & -c_{\text{db}}^{(0)} \\ \eta c_{\text{id}}^{(0)} & \eta c_{\text{ig}}^{(0)} - \zeta' & \eta c_{\text{is}}^{(0)} & \eta c_{\text{ib}}^{(0)} + \zeta' \\ -c_{\text{sd}}^{(0)} & -c_{\text{sg}}^{(0)} & -c_{\text{ss}}^{(0)} & -c_{\text{sb}}^{(0)} \\ \zeta c_{\text{id}}^{(0)} & \zeta c_{\text{ig}}^{(0)} + \zeta' & \zeta c_{\text{is}}^{(0)} & \zeta c_{\text{ib}}^{(0)} - \zeta' \end{bmatrix} \tag{4.99}$$

Here, $\zeta' = \zeta / F_\omega$. Note that we assumed negligible steady-state gate and bulk currents which lead to the vanishing elements $g_{\text{gk}}^{(0)}$ and $g_{\text{bk}}^{(0)}$.

4.1.3. Lowest-Order Corrections to the QS Small-Signal Model

To obtain the lowest-order corrections to the QS model needed for the benchmark analysis, we substitute

$$F_\omega = 1 - (\omega\tau)^2 + O(\omega^4) \tag{4.100}$$

in (4.98) and (4.99). This results in

$$[g_{\text{jk}}] = \left[g_{\text{jk}}^{(0)}\right] + \left[g_{\text{jk}}^{(1)}\right] + O(\omega^4) \tag{4.101}$$

and

$$[c_{\text{jk}}] = \left[c_{\text{jk}}^{(0)}\right] + \left[c_{\text{jk}}^{(1)}\right] + O(\omega^4) \tag{4.102}$$

where

$$\left[g_{\text{jk}}^{(0)}\right] = \begin{bmatrix} g_{\text{dd}}^{(0)} & g_{\text{dg}}^{(0)} & g_{\text{ds}}^{(0)} & g_{\text{db}}^{(0)} \\ 0 & 0 & 0 & 0 \\ g_{\text{sd}}^{(0)} & g_{\text{sg}}^{(0)} & g_{\text{ss}}^{(0)} & g_{\text{sb}}^{(0)} \\ 0 & 0 & 0 & 0 \end{bmatrix} \tag{4.103}$$

$$\left[c_{\mathrm{jk}}^{(0)}\right] = \begin{bmatrix} c_{\mathrm{dd}}^{(0)} & c_{\mathrm{dg}}^{(0)} & c_{\mathrm{ds}}^{(0)} & c_{\mathrm{db}}^{(0)} \\ -\eta \cdot c_{\mathrm{id}}^{(0)} & \zeta - \eta \cdot c_{\mathrm{ig}}^{(0)} & -\eta \cdot c_{\mathrm{is}}^{(0)} & -\zeta - \eta \cdot c_{\mathrm{ib}}^{(0)} \\ c_{\mathrm{sd}}^{(0)} & c_{\mathrm{sg}}^{(0)} & c_{\mathrm{ss}}^{(0)} & c_{\mathrm{sb}}^{(0)} \\ -\zeta \cdot c_{\mathrm{id}}^{(0)} & -\zeta \cdot \left[1 + c_{\mathrm{ig}}^{(0)}\right] & -\zeta \cdot c_{\mathrm{is}}^{(0)} & \zeta \cdot \left[1 - c_{\mathrm{ib}}^{(0)}\right] \end{bmatrix} \tag{4.104}$$

$$\left[g_{\mathrm{jk}}^{(1)}\right] = k_0 \begin{bmatrix} c_{\mathrm{dd}}^{(0)} & c_{\mathrm{dg}}^{(0)} & c_{\mathrm{ds}}^{(0)} & c_{\mathrm{db}}^{(0)} \\ -\eta \cdot c_{\mathrm{id}}^{(0)} & -\eta \cdot c_{\mathrm{ig}}^{(0)} & -\eta \cdot c_{\mathrm{is}}^{(0)} & -\eta \cdot c_{\mathrm{ib}}^{(0)} \\ c_{\mathrm{sd}}^{(0)} & c_{\mathrm{sg}}^{(0)} & c_{\mathrm{ss}}^{(0)} & c_{\mathrm{sb}}^{(0)} \\ -\zeta \cdot c_{\mathrm{id}}^{(0)} & -\zeta \cdot c_{\mathrm{ig}}^{(0)} & -\zeta \cdot c_{\mathrm{is}}^{(0)} & -\zeta \cdot c_{\mathrm{ib}}^{(0)} \end{bmatrix} \tag{4.105}$$

and

$$\left[c_{\mathrm{jk}}^{(1)}\right] = -\frac{k_0 \tau}{C_{\mathrm{ox}}} \begin{bmatrix} c_{\mathrm{dd}}^{(0)} & c_{\mathrm{dg}}^{(0)} & c_{\mathrm{ds}}^{(0)} & c_{\mathrm{db}}^{(0)} \\ -\eta \cdot c_{\mathrm{id}}^{(0)} & -\eta \cdot c_{\mathrm{ig}}^{(0)} & -\eta \cdot c_{\mathrm{is}}^{(0)} & -\eta \cdot c_{\mathrm{ib}}^{(0)} \\ c_{\mathrm{sd}}^{(0)} & c_{\mathrm{sg}}^{(0)} & c_{\mathrm{ss}}^{(0)} & c_{\mathrm{sb}}^{(0)} \\ -\zeta \cdot c_{\mathrm{id}}^{(0)} & -\zeta \cdot c_{\mathrm{ig}}^{(0)} & -\zeta \cdot c_{\mathrm{is}}^{(0)} & -\zeta \cdot c_{\mathrm{ib}}^{(0)} \end{bmatrix} \tag{4.106}$$

Note that

$$\left[c_{\mathrm{jk}}^{(1)}\right] = -\frac{\tau}{C_{\mathrm{ox}}} \cdot \left[g_{\mathrm{jk}}^{(1)}\right] \tag{4.107}$$

Physically, $\left[g_{\mathrm{jk}}^{(0)}\right]$ and $\left[c_{\mathrm{jk}}^{(0)}\right]$ are the QS conductances and capacitances matrices and $\left[g_{\mathrm{jk}}^{(1)}\right]$ and $\left[c_{\mathrm{jk}}^{(1)}\right]$ are the lowest-order corrections predicted by the new RTA model.

4.2. Benchmark Test for $V_{\mathrm{DS}} = 0$ in Strong Inversion Regime

Smit et al. [62] suggested a benchmark for NQS models based on the double transmission line representation of the MOSFET for $V_{\mathrm{DS}} = 0$ in the strong inversion

regime (when the diffusion current may be neglected.) Here, we apply their test to the new RTA model developed.

For $V_{\mathrm{DS}} = 0$ we have

$$g_{\mathrm{dg}}^{(0)} = 0 \tag{4.108}$$

$$g_{\mathrm{bg}}^{(0)} = 0 \tag{4.109}$$

$$g_{\mathrm{ds}}^{(0)} = g_{\mathrm{sd}}^{(0)} = -g_{\mathrm{dd}}^{(0)} \tag{4.110}$$

and

$$g_{\mathrm{ss}}^{(0)} = g_{\mathrm{dd}}^{(0)} \tag{4.111}$$

Hence, from (4.103)

$$\left[g_{\mathrm{jk}}^{(0)}\right] = g_{\mathrm{dd}}^{(0)} \begin{bmatrix} 1 & 0 & -1 & 0 \\ 0 & 0 & 0 & 0 \\ -1 & 0 & 1 & 0 \\ 0 & 0 & 0 & 0 \end{bmatrix} \tag{4.112}$$

while $\left[c_{\mathrm{jk}}^{(0)}\right]$, $\left[g_{\mathrm{jk}}^{(1)}\right]$, and $[c_{\mathrm{jk}}]$ are the same as (4.104), (4.105), and (4.106), respectively.

We next transform the lowest-order corrections $\left[g_{\mathrm{jk}}^{(1)}\right]$ and $\left[c_{\mathrm{jk}}^{(1)}\right]$ to facilitate the comparison of the new RTA model with the "exact" results in [62]. For $V_{\mathrm{DS}} = 0$ in a strong inversion regime, the $\left[c_{\mathrm{jk}}^{(0)}\right]$ term in (4.104) should be equivalent to the

corresponding $\left[c^{(0)}_{\mathrm{jk,TLM}}\right]$ term of (7) in [62] which is given below [1]

$$\left[c^{(0)}_{\mathrm{jk,TLM}}\right] = \frac{1}{6}\begin{bmatrix} 2\alpha & -3 & \alpha & 3-3\alpha \\ -3 & 6 & -3 & 0 \\ \alpha & -3 & 2\alpha & 3-3\alpha \\ 3-3\alpha & 0 & 3-3\alpha & 6\alpha-6 \end{bmatrix} \tag{4.113}$$

where $\alpha = 1 + \xi$.

By equating elements of (4.104) and (4.113), one finds

$$c^{(0)}_{\mathrm{dd}} = c^{(0)}_{\mathrm{ss}} = \frac{\alpha}{3} \tag{4.114}$$

$$c^{(0)}_{\mathrm{dg}} = c^{(0)}_{\mathrm{sg}} = -\frac{1}{2} \tag{4.115}$$

$$c^{(0)}_{\mathrm{ds}} = c^{(0)}_{\mathrm{sd}} = \frac{\alpha}{6} \tag{4.116}$$

$$c^{(0)}_{\mathrm{db}} = \frac{1-\alpha}{2} \tag{4.117}$$

$$c^{(0)}_{\mathrm{gd}} = -\eta \cdot c^{(0)}_{\mathrm{id}} = -\frac{1}{2} \tag{4.118}$$

$$c^{(0)}_{\mathrm{gg}} = 1 - \eta - \eta \cdot c^{(0)}_{\mathrm{ig}} = 1 \tag{4.119}$$

$$c^{(0)}_{\mathrm{gs}} = -\eta \cdot c^{(0)}_{\mathrm{is}} = -\frac{1}{2} \tag{4.120}$$

$$c^{(0)}_{\mathrm{gb}} = -\zeta - \eta \cdot c^{(0)}_{\mathrm{ib}} = 0 \tag{4.121}$$

$$c^{(0)}_{\mathrm{sb}} = \frac{1-\alpha}{2} \tag{4.122}$$

[1] The $c^{(0)}_{\mathrm{jk,TLM}}$ of (7) in [62] is a 3x3 matrix. The fourth column and fourth row in this thesis are evaluated by applying the rule that the sum of the matrix elements in each column or row should be zero.

which yields

$$c_{\mathrm{dd}}^{(0)} = \frac{\alpha}{3} \tag{4.123}$$

$$c_{\mathrm{dg}}^{(0)} = -\frac{1}{2} \tag{4.124}$$

$$c_{\mathrm{ds}}^{(0)} = \frac{\alpha}{6} \tag{4.125}$$

$$c_{\mathrm{db}}^{(0)} = \frac{1-\alpha}{2} \tag{4.126}$$

$$c_{\mathrm{id}}^{(0)} = \frac{1}{2\eta} = \frac{\alpha}{2} \tag{4.127}$$

$$c_{\mathrm{ig}}^{(0)} = -1 \tag{4.128}$$

$$c_{\mathrm{is}}^{(0)} = \frac{1}{2\eta} = \frac{\alpha}{2} \tag{4.129}$$

$$c_{\mathrm{ib}}^{(0)} = 1-\alpha \tag{4.130}$$

$$c_{\mathrm{sd}}^{(0)} = \frac{\alpha}{6} \tag{4.131}$$

$$c_{\mathrm{sg}}^{(0)} = -\frac{1}{2} \tag{4.132}$$

$$c_{\mathrm{ss}}^{(0)} = \frac{\alpha}{3} \tag{4.133}$$

$$c_{\mathrm{sb}}^{(0)} = \frac{1-\alpha}{2} \tag{4.134}$$

Inserting (4.123)-(4.134) into (4.105) and (4.106), one finds that, when $V_{\mathrm{DS}} = 0$ in a strong inversion regime

$$\left[g_{\mathrm{jk}}^{(1)}\right] = k_0 \begin{bmatrix} \alpha/3 & -1/2 & \alpha/6 & (1-\alpha)/2 \\ -1/2 & 1/\alpha & -1/2 & (\alpha-1)/\alpha \\ \alpha/3 & -1/2 & \alpha/6 & (1-\alpha)/2 \\ (1-\alpha)/2 & (\alpha-1)/\alpha & (1-\alpha)/2 & (\alpha-1)^2/\alpha \end{bmatrix} \tag{4.135}$$

and

$$\left[c_{\mathrm{jk}}^{(1)}\right] = -\frac{k_0 \cdot \tau}{C_{\mathrm{ox}}} \begin{bmatrix} \alpha/3 & -1/2 & \alpha/6 & (1-\alpha)/2 \\ -1/2 & 1/\alpha & -1/2 & (\alpha-1)/\alpha \\ \alpha/3 & -1/2 & \alpha/6 & (1-\alpha)/2 \\ (1-\alpha)/2 & (\alpha-1)/\alpha & (1-\alpha)/2 & (\alpha-1)^2/\alpha \end{bmatrix} \tag{4.136}$$

The lowest order NQS corrections to the QS y-matrix are given by

$$\left[g_{\mathrm{jk,TLM}}^{(1)}\right] = k_1 \begin{bmatrix} 8\alpha^2 & -15\alpha & 7\alpha^2 & -15\alpha\xi \\ -15\alpha & 30 & -15\alpha & 30\xi \\ 7\alpha^2 & -15\alpha & 8\alpha^2 & -15\alpha\xi \\ -15\alpha\xi & 30\xi & -15\alpha\xi & 30\xi^2 \end{bmatrix} \tag{4.137}$$

and

$$\left[c_{\mathrm{jk,TLM}}^{(1)}\right] = k_2 \begin{bmatrix} -32\alpha & 63 & -31\alpha & 63\xi \\ 63 & -\frac{126}{\alpha} & 63 & -126\frac{\xi}{\alpha} \\ -31\alpha & 63 & -32\alpha & 63\xi \\ 63\xi & -126\frac{\xi}{\alpha} & 63\xi & 126\frac{\xi^2}{\alpha} \end{bmatrix} \tag{4.138}$$

where

$$k_1 = \omega^2 C_{\mathrm{ox}}^2 / \left[360 g_{\mathrm{dd}}^{(0)}\right] \tag{4.139}$$

and

$$k_2 = \omega^2 C_{\mathrm{ox}}^2 \alpha^2 / \left\{15120 \left[g_{\mathrm{dd}}^{(0)}\right]^2\right\} \tag{4.140}$$

To obtain the lowest order NQS corrections to the y-matrix for the present model, we use expansions (4.101) and (4.102) for the small-signal version of the

model developed in (4.98) and (4.99). In the strong inversion regime for $V_{\mathrm{DS}} = 0$

$$\left[g_{\mathrm{jk}}^{(1)}\right] = k_\tau k_1 \begin{bmatrix} 10\alpha^2 & -15\alpha & 5\alpha^2 & -15\alpha\xi \\ -15\alpha & 30 & -15\alpha & 30\xi \\ 5\alpha^2 & -15\alpha & 10\alpha^2 & -15\alpha\xi \\ -15\alpha\xi & 30\xi & -15\alpha\xi & 30\xi^2 \end{bmatrix} \tag{4.141}$$

and

$$\left[c_{\mathrm{jk}}^{(1)}\right] = \frac{5k_\tau^2 k_2}{6} \begin{bmatrix} -42\alpha & 63 & -21\alpha & 63\xi \\ 63 & -\frac{126}{\alpha} & 63 & -126\frac{\xi}{\alpha} \\ -21\alpha & 63 & -42\alpha & 63\xi \\ 63\xi & -126\frac{\xi}{\alpha} & 63\xi & 126\frac{\xi^2}{\alpha} \end{bmatrix} \tag{4.142}$$

where

$$k_\tau = \frac{12\tau g_{\mathrm{dd}}^{(0)}}{\alpha C_{\mathrm{ox}}} \tag{4.143}$$

is a dimensionless coefficient close to 1. For the purpose of this study, we select

$$\tau = \frac{\sqrt{30}\alpha C_{\mathrm{ox}}}{60\tau g_{\mathrm{dd}}^{(0)}} \tag{4.144}$$

which is equivalent to setting $k_\tau = \sqrt{30}/5 \approx 1.095$. This choice makes $\left[c_{\mathrm{jk}}^{(1)}\right]$ close to the ideal value $\left[c_{\mathrm{jk,TLM}}^{(1)}\right]$ given by (4.138). To facilitate the comparison of (4.141), (4.142) with (4.137), (4.138), we introduce the "ratio matrices" $R_{\mathrm{jk}}^{(g)} = g_{\mathrm{jk}}^{(1)}/g_{\mathrm{jk,TLM}}^{(1)}$ and $R_{\mathrm{jk}}^{(c)} = c_{\mathrm{jk}}^{(1)}/c_{\mathrm{jk,TLM}}^{(1)}$. From (4.137), (4.138), (4.141), and (4.142),

$$\left[R_{\mathrm{jk}}^{(g)}\right] = \begin{bmatrix} 1.37 & 1.10 & 0.78 & 1.10 \\ 1.10 & 1.10 & 1.10 & 1.10 \\ 0.78 & 1.10 & 1.37 & 1.10 \\ 1.10 & 1.10 & 1.10 & 1.10 \end{bmatrix} \tag{4.145}$$

$$\left[R_{\mathrm{jk}}^{(c)}\right] = \begin{bmatrix} 1.31 & 1 & 0.68 & 1 \\ 1 & 1 & 1 & 1 \\ 0.68 & 1 & 1.35 & 1 \\ 1 & 1 & 1 & 1 \end{bmatrix} \tag{4.146}$$

Since ideally all elements of these matrices are equal to one, the new RTA model satisfies the benchmark test only approximately. This inherent limitation of the RTA approach can be regarded as the price that is paid for model speed and simplicity.

CHAPTER 5

Bulk Resistance Effect on MOSFET Gate Capacitance

5.1. Introduction

The gate capacitance, C_{gg}, of MOS transistors and capacitors is frequency dependent in all regions of operation. However, different physical mechanisms control the frequency dependence in different regions of operation.

In strong inversion, the electron concentration (here, we assume a p-bulk structure) in the channel can lag in time (i.e. have inertia) with respect to changes in gate voltage; for rapidly changing gate bias, the channel charge does not have time to equilibrate to a value consistent with the instantaneous values of the terminal biases. The delay in establishment of the channel charge is in MOS transistors due to the finite transit time of electrons from the source and drain into the channel, and in MOS capacitors due to finite recombination and generation lifetimes for electrons. In both cases, the qualitative effect, but not details of the frequency dependence, is similar: as frequency increases C_{gg} in inversion decreases. This is the so-called NQS behavior.

In accumulation operation, C_{gg} also decreases as frequency increases. In at least one compact MOS transistor model, this has been attributed to inertia in the formation of bulk charge. Actually, the physical cause of this behavior is different; for the p-bulk MOS structure in accumulation, there is a plethora of holes available in the bulk immediately adjacent to the surface, so there should be negligible delay in the re-equilibration of the accumulation charge following a change in gate voltage and therefore, no inertia effect on MOS capacitance in accumulation.

In this chapter, we present TCAD simulations and derive a new analytic model for the frequency dependence of C_{gg} in accumulation and depletion that accounts for the series resistance R_{bulk} of the bulk, to show that the variation of MOS device C_{gg} with frequency in accumulation does not arise from charge inertia effects but rather, is due to the influence of R_{bulk}. We then show that the frequency dependence of C_{gg} for MOS transistors for all biases can be accurately modeled using the PSP-RTA-NQS MOSFET compact model and present measured data, along with simulations from PSP-RTA-NQS, to show that the series resistance R_{gate} of the gate needs to be included to accurately model the frequency dependence of C_{gg} from accumulation through strong inversion.

The gate capacitance normalized by the oxide capacitance C_{ox} will be denoted in lower case, i.e. $c_{\mathrm{gg}} = C_{\mathrm{gg}}/C_{\mathrm{ox}}$ (see (4.17)). In this work, it was not found necessary to include the effect of gate leakage current on the frequency dependence of C_{gg}. Generally speaking, this is another source of dispersion in advanced MOS structures [112].

5.2. TCAD and PSP-RTA-NQS Modeling

Fig. 5.1 shows TCAD simulations [149] of MOSFET gate capacitance, for $V_{\mathrm{DS}} = V_{\mathrm{BS}} = 0$ over gate voltage V_{GS} and frequency f, along with simulations from the QS version of the PSP model [53] with no R_{bulk}. The TCAD simulations were performed with an ideal contact at the top of the gate dielectric and so include no parasitic gate resistance; R_{gate} was therefore set to zero in PSP for all comparisons to TCAD simulations.

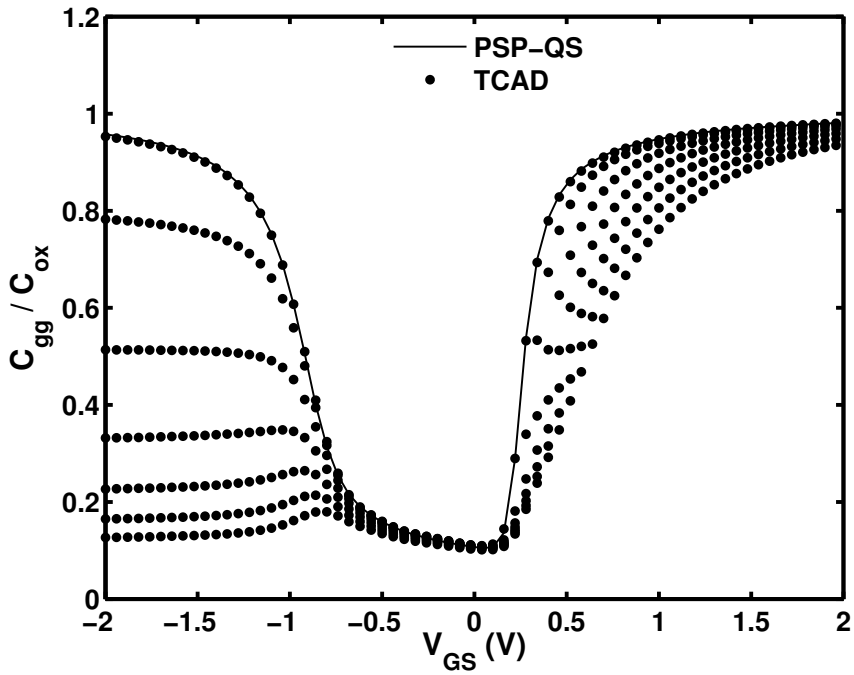

Fig. 5.1. TCAD and PSP-QS models of normalized $C_{\rm gg}$, with $R_{\rm bulk} = 0$ for PSP-QS. $W/L = 1.0\mu$m/5.0μm, $t_{\rm ox} = 2.0$nm, $N_{\rm bulk} = 3.0 \times 10^{17}$cm^{-3} ($p$-type), frequencies are 0, $0.25f_{\rm T}$, $0.5f_{\rm T}$, $0.75f_{\rm T}$, $f_{\rm T}$, $1.25f_{\rm T}$ and $1.5f_{\rm T}$(top to bottom). Here $f_{\rm T} = 1.6$ GHz and substrate thickness $t_{\rm bulk} = 30$ μm.

The TCAD simulations clearly show the decrease in $C_{\rm gg}$ with increasing frequency, both in accumulation and inversion regions of operation. (The decrease is also apparent in depletion, but is less pronounced.) The PSP-QS model show ideal MOS transistor capacitance behavior irrespective of frequency. Note the qualitative difference in the shape of the $C_{\rm gg}(V_{\rm GS})$ curves over frequency between accumulation and strong inversion. In accumulation, the curves are almost horizontal and move down by approximately the same amount as frequency increases. In strong inversion, the amount of reduction in $C_{\rm gg}$ decreases as $V_{\rm GS}$ increases for a given frequency, i.e. there is a slope introduced into the $C_{\rm gg}(V_{\rm GS})$ characteristics.

If the frequency dependence of $C_{\rm gg}$ is due to the inertia in formation of the in-

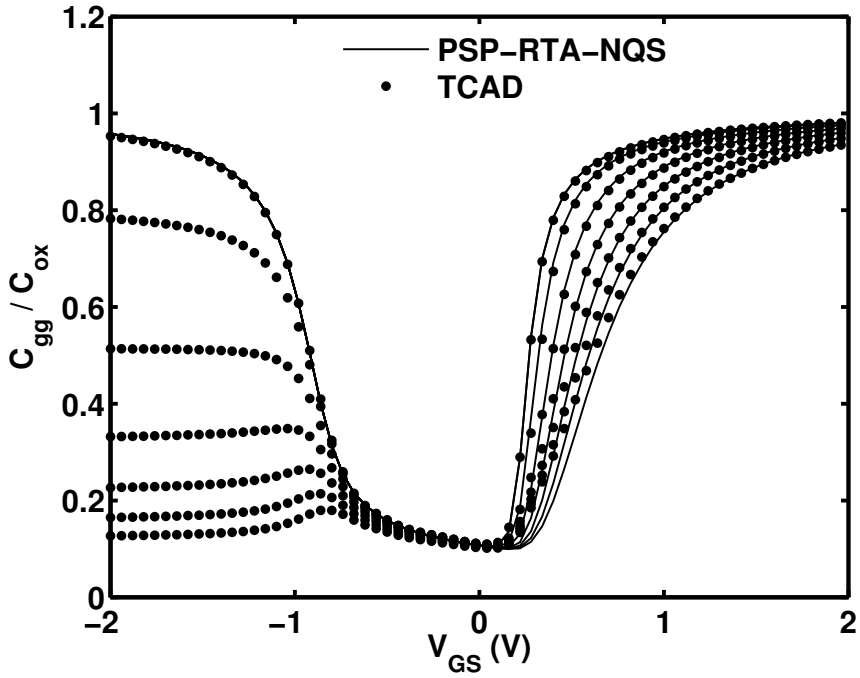

Fig. 5.2. Effect of accounting for NQS behavior – TCAD and PSP-RTA-NQS models of normalized C_{gg}, with $R_{\mathrm{bulk}} = 0$ for PSP-RTA-NQS. Same device parameters and frequencies as Fig. 5.1.

version layer, then this should be able to be modeled by the PSP-RTA-NQS model; Fig. 5.2 shows the results of such simulations. The improvement in accuracy of the compact model, which is based on RTA and depends on two adjustable model parameters, is apparent in strong inversion, but there is no improvement in accumulation or depletion where the inversion charge is negligible.

Due to the fact that in accumulation and depletion there is, from the bulk p-type doping, an excess of mobile holes (i.e. majority carriers) readily available, there should be negligible inertia in the change in bulk charge with respect to a change in terminal voltages. The frequency dependence of C_{gg} out of inversion, therefore, should not be due to an NQS effect; most likely, it could be from series re-

sistance. Given that $R_{\text{gate}} = 0$ in the TCAD simulations, the cause of the frequency dependence of C_{gg} in accumulation and depletion in Fig. 5.2 should be R_{bulk}, which should appear in series with the intrinsic MOS capacitance.

To provide an explanation of the difference in qualitative behavior of the TCAD simulations between accumulation and strong inversion, and support for the statements in the two preceding paragraphs, we will use simplified models that are applicable only to each of these individual regions of operation; neither is a general model that is appropriate for all operating regions.

First, in strong inversion, the effective gate capacitance of a MOS transistor, at an angular frequency ω for $V_{\text{DS}} = 0$, using a first order expansion in $i\omega$ of an NQS analysis based on the continuity equation in the channel [1], is

$$C_{\text{gg}}(\omega) = \frac{C_{\text{gg}}^{(0)}}{1 + \left[\dfrac{\omega L^2}{12\mu(V_{\text{GS}} - V_{\text{T}})}\right]^2} \tag{5.1}$$

where V_{T} is the threshold voltage. This indicates that at a given frequency, as V_{GS} increases in strong inversion, $C_{\text{gg}}(\omega)$ should increase and asymptotically approach $C_{\text{gg}}^{(0)}$ for large $V_{\text{GS}} - V_{\text{T}}$. This is precisely the qualitative behavior seen in strong inversion in Fig. 5.2, both for the TCAD simulations and for the PSP-RTA-NQS model.

Second, consider operation in accumulation. If the device is modeled as R_{bulk} in series with $C_{\text{gg}}^{(0)}$, then

$$C_{\text{gg}}(\omega) = \frac{C_{\text{gg}}^{(0)}}{1 + \left[\omega R_{\text{bulk}} C_{\text{gg}}^{(0)}\right]^2}\,. \tag{5.2}$$

If the frequency dependence in accumulation in Fig. 5.2 is due to series resistance, then from (5.2) a plot of $C_{\text{gg}}^{(0)}/C_{\text{gg}}$ vs. ω^2 should be a straight line with slope

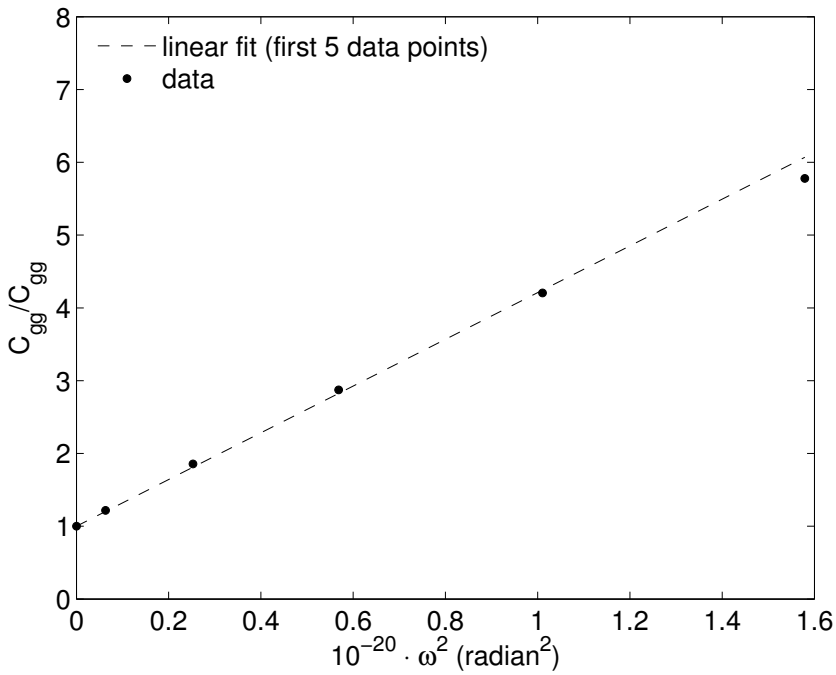

Fig. 5.3. $C_{\mathrm{gg}}^{(0)}/C_{\mathrm{gg}}$ vs. ω^2 from TCAD simulations at $V_{\mathrm{GS}} = -2$.

$\left[R_{\mathrm{bulk}}C_{\mathrm{gg}}^{(0)}\right]^2$. Fig. 5.3 shows this plot from the TCAD simulations for frequencies up to $1.25f_{\mathrm{T}}$ (at f_{T} there is some deviation from the linear trend predicted by (5.2), which is only a first-order approximation.) This supports the hypothesis that the frequency dependence of C_{gg} in accumulation is from series resistance. Further, (5.2) indicates that the decrease in C_{gg} with frequency should, for a fixed series resistance, be smaller if the low frequency capacitance is smaller; the simple series $R_{\mathrm{bulk}}C_{\mathrm{gg}}^{(0)}$ model (5.2), therefore, also explains the reduced frequency dependence in depletion, where the low frequency capacitance is significantly smaller than in accumulation, but R_{bulk} is essentially unchanged. The rapid increase in $C_{\mathrm{gg}}^{(0)}$ as V_{GS} decreases is the cause of the peak in C_{gg} around flatband at high frequencies.

We stress that the models (5.1) and (5.2) used for the above analyses are not

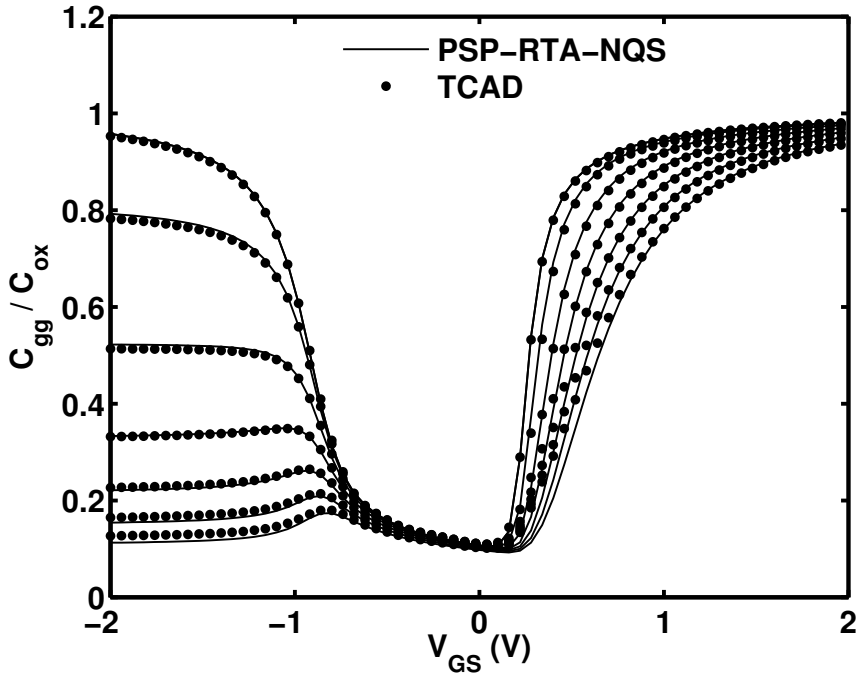

Fig. 5.4. Effect of accounting for both R_{bulk} and NQS behavior – TCAD and PSP-RTA-NQS models of C_{gg} with $R_{\text{bulk}} = 2.2$ kΩ included for PSP-RTA-NQS. Same device parameters and frequencies as Fig. 5.1.

general and are only approximate even in the regions of operation they are targeted to model. We now present further PSP-RTA-NQS and TCAD simulation results that verify that the frequency dependence of C_{gg} is due to R_{bulk} in accumulation and is due to inversion charge inertia in strong inversion.

Fig. 5.4 shows PSP-RTA-NQS simulations that include R_{bulk}; there is a significant improvement in compact modeling accuracy in accumulation and depletion cf. Fig. 5.2, and in particular, the peaks in C_{gg} in the vicinity of flatband at the higher frequencies are captured. The value of R_{bulk} determined from optimization to fit the TCAD simulations is 2.20 kΩ; this compares well with the values of 2.23 and 2.17 kΩ determined from the slope of a linear regression using the first 3 and

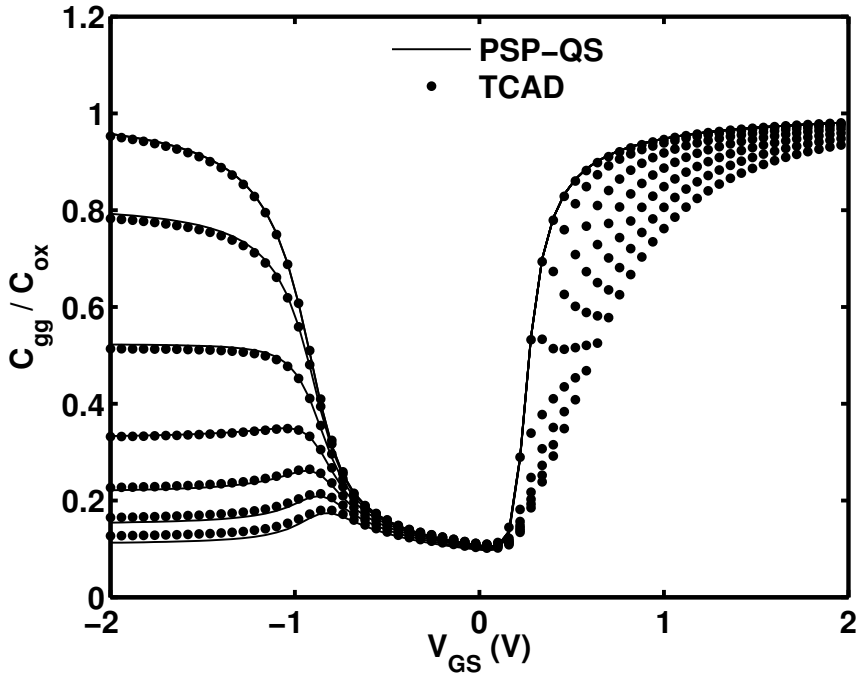

Fig. 5.5. Effect of accounting for R_{bulk} – TCAD and PSP-QS models of C_{gg} with $R_{\text{bulk}} = 2.2$ kΩ included for PSP-QS. Same device parameters and frequencies as Fig. 5.1.

the first 5 points of the plot of Fig. 5.3, respectively. As further verification that the frequency dependence of C_{gg} in accumulation is a bulk resistance effect, and not an NQS effect, Fig. 5.5 shows simulations with R_{bulk} included but using the PSP-QS model; there is no change in the accuracy of fit of C_{gg} in accumulation and depletion cf. Fig. 5.4.

Fig. 5.6 shows results, at $f = f_{\text{T}}$, with the body thickness in the TCAD simulations varied from 20 μm to 40 μm. Increasing the body thickness should not alter the inertia of holes at the surface, but increases R_{bulk} and therefore, decreases the apparent C_{gg} at high frequency; this is exactly what is observed in Fig. 5.6. R_{bulk} was adjusted in PSP-RTA-NQS for each case for good fitting of the TCAD

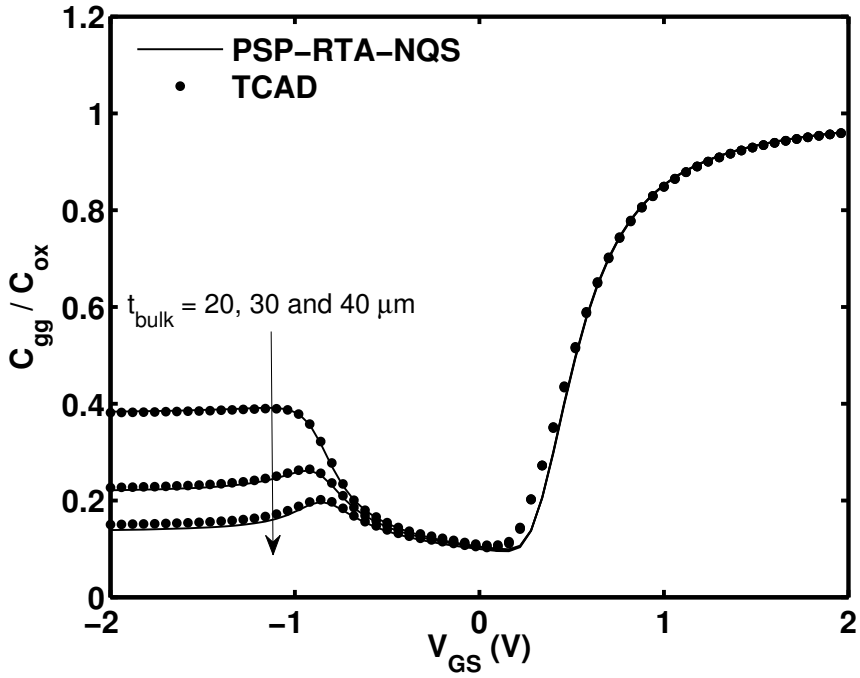

Fig. 5.6. Effect of variation of bulk thickness, $f = f_{\mathrm{T}} = 1.6$ GHz. PSP-RTA-NQS model parameter $R_{\mathrm{bulk}} = 2/3R_{\mathrm{bulk0}}$, R_{bulk0} and $4/3R_{\mathrm{bulk0}}$ for $t_{\mathrm{bulk}} = 2/3t_{\mathrm{bulk0}}$, t_{bulk0} and $4/3t_{\mathrm{bulk0}}$, respectively. Here $R_{\mathrm{bulk0}} = 2.2$ kΩ and $t_{\mathrm{bulk0}} = 30$ μm.

simulations, and the ratio of R_{bulk} to the body thickness varied by less than 10% over the body thickness values that were simulated.

The frequency dependence of C_{gg} in accumulation and depletion is thus not an NQS effect for the body charge, but is due to the resistance of the bulk (and, as we will see below, also depends on gate resistance, although to a lesser extent); inclusion of series resistance is therefore necessary to model properly C_{gg} over frequency.

5.3. Analytic Expression for C_{gg} in the Presence of Bulk Resistance

The simple series $R_{\mathrm{bulk}}C_{\mathrm{gg}}^{(0)}$ analysis result (5.2) does not take into account details of the operation of MOS devices. In particular, it fails to predict that R_{bulk} does not affect C_{gg} in strong inversion, see Fig. 5.5. Physically, this is due to the

fact that in strong inversion, the incremental change in inversion charge with bias flows from the source and drain regions and not from the bulk of the device. To make this clear, we now develop an analytic expression for the effect of R_{bulk} while neglecting, for simplicity, inertia in the formation of the inversion charge.

We adopt the notation

$$v_{\mathrm{G}}(t) = V_{\mathrm{G}} + \mathrm{Re}\left(\Delta v_{\mathrm{g}} \cdot e^{i\omega t}\right) \tag{5.3}$$

where $v_{\mathrm{G}}(t)$ is the instantaneous value of the gate bias, V_{G} is its quiescent value, and Δv_{g} is the phasor representing the small harmonic component with the angular frequency ω. Another example, the phasors for the substrate displacement current and charge are related by

$$\Delta i_{\mathrm{b}} = i\omega \Delta q_{\mathrm{b}} \ . \tag{5.4}$$

Inclusion of the voltage drop in the bulk in the surface potential equation gives

$$v_{\mathrm{GB}}(t) - V_{\mathrm{FB}} - \psi_{\mathrm{S}}(t) - i_{\mathrm{b}}(t) R_{\mathrm{bulk}} = -q_{\mathrm{I}}(t) - q_{\mathrm{B}}(t) \tag{5.5}$$

where ψ_{S}, q_{I}, and q_{B} are following the same definitions we used in the previous chapters. It is also assumed that the quiescent substrate current is negligible

$$i_{\mathrm{B}} = i_{\mathrm{b}} \tag{5.6}$$

With reference to (5.4), the phasor form of this equation becomes

$$\Delta v_{\mathrm{g}} = [1 + (1 + i\omega T_{\mathrm{B}})\xi]\Delta\psi_{\mathrm{s}} - \Delta q_{\mathrm{i}} \tag{5.7}$$

where $T_{\mathrm{B}} = R_{\mathrm{bulk}} C_{\mathrm{ox}}$ and $\xi = -dq_{\mathrm{B}}/d\psi_{\mathrm{S}}/C_{\mathrm{ox}}$, see (4.8). In the QS approximation (neglecting the inertia of the inversion layer formation, cf. [58, 60])

$$\Delta q_{\mathrm{g}}/C_{\mathrm{ox}} = F \Delta\psi_{\mathrm{s}} \tag{5.8}$$

$$\Delta q_{\mathrm{i}}/C_{\mathrm{ox}} = (F - \xi)\Delta\psi_{\mathrm{s}} \tag{5.9}$$

and

$$F = dv_{\mathrm{G}}/d\psi_{\mathrm{S}} - 1\,. \tag{5.10}$$

Then, from (5.7)

$$\Delta v_{\mathrm{g}} = (1 + F + i\omega T_{\mathrm{B}}\xi)\,\Delta\psi_{\mathrm{s}} \tag{5.11}$$

$$= (1 + F)(1 + i\omega T_{\mathrm{B}} c_{42})\Delta\psi_{\mathrm{s}} \tag{5.12}$$

where

$$c_{42} = \frac{\xi}{1 + F} = \frac{1}{C_{\mathrm{ox}}}\frac{dq_{\mathrm{B}}}{dv_{\mathrm{G}}}\,. \tag{5.13}$$

Using (5.8) once more yields

$$\frac{\Delta q_{\mathrm{g}}}{\Delta v_{\mathrm{g}}} = \frac{\Delta q_{\mathrm{g}}/\Delta\psi_{\mathrm{s}}}{\Delta v_{\mathrm{g}}/\Delta\psi_{\mathrm{s}}} \tag{5.14}$$

$$= \frac{1}{C_{\mathrm{ox}}}\frac{F}{(1 + F)(1 + i\omega T_{\mathrm{B}} c_{42})} \tag{5.15}$$

and including the quasi-equilibrium value

$$C_{\mathrm{gg}}^{(0)} = F/(1 + F) \tag{5.16}$$

of c_{gg} for $R_{\mathrm{bulk}} = 0$ gives

$$c_{\mathrm{gg}} = \frac{1}{C_{\mathrm{ox}}}\Re\left(\Delta q_{\mathrm{g}}/\Delta v_{\mathrm{g}}\right) \tag{5.17}$$

$$= \frac{C_{\mathrm{gg}}^{(0)}}{1 + (\omega T_{\mathrm{B}} c_{42})^2} \tag{5.18}$$

In non-normalized form, this is

$$C_{\mathrm{gg}} = \frac{C_{\mathrm{gg}}^{(0)}}{1 + (\omega R_{\mathrm{bulk}} C_{\mathrm{bg}})^2} \tag{5.19}$$

The non-trivial aspect of this analysis is that different capacitances appear in the numerator and denominator of (5.18) and (5.19); this does not follow from the simple $R_{\mathrm{bulk}} C_{\mathrm{gg}}^{(0)}$ analysis of (5.2). In strong inversion, C_{bg} is negligible and the effect of R_{bulk} disappears, as explained above. In accumulation, $C_{\mathrm{bg}} = C_{\mathrm{gg}}^{(0)}$, so (5.19) reduces to (5.2).

Comparison with the results of TCAD simulations, see Fig. 5.7, shows that (5.18) accurately describes the effects of series resistance, including the peak of C_{gg} near flatband. This further confirms that NQS effects are not involved in the frequency dependence of C_{gg} in the accumulation and depletion regions.

5.4. Experimental Data

To further investigate the frequency dependence of MOSFET gate capacitance, we measured s-parameters over gate bias and frequency, with $V_{\mathrm{DS}} = V_{\mathrm{BS}} = 0$, of a PMOS transistor in a 90nm RF CMOS process.

Fig. 5.8 shows measured data from the device, along with simulation results from the PSP-RTA-NQS model. R_{bulk} and R_{gate} were adjusted to provide a least squares fit to the data. The peak in the $C_{\mathrm{gg}}(V_{\mathrm{G}})$ characteristic near flatband seen in the TCAD simulations and predicted by our analytic expression (5.18) are also observed in the measured data and are able to be modeled by PSP-RTA-NQS.

Unlike the TCAD simulations, the measured device does not have an ideal gate contact but includes some nonzero R_{gate}. Fig. 5.9 shows the measured data along

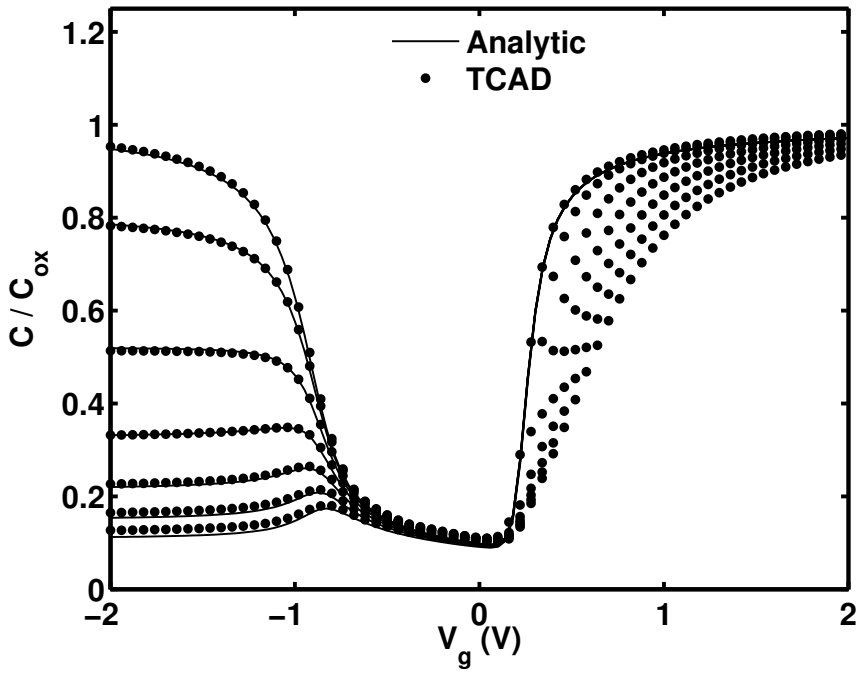

Fig. 5.7. TCAD and analytic models, R_{bulk} effect only (no NQS) in the analytic model. Same device parameters and frequencies as Fig. 5.1.

with PSP-RTA-NQS simulations with all parameters kept at the same values as those used for Fig. 5.8 with the exception of R_{gate}, which was set to zero. The gate resistance has some effect on the PSP-RTA-NQS simulation results, especially at higher frequencies in strong inversion. This is where it would be expected to have the greatest influence: in strong inversion, the gate charging current is predominantly gate-to-channel. Hence, it should be affected by R_{gate} but not by R_{bulk}. There is some influence of R_{gate} in accumulation, as well; however, as Fig. 5.10 shows, if R_{bulk} is set to zero instead of R_{gate}, the change in behavior in accumulation is significantly greater, and there is only a very small change in the modeled characteristics in strong inversion. This is also expected as, in general, the gate is made from much lower resistivity material than the bulk, therefore, R_{bulk} should be greater than R_{gate}; they

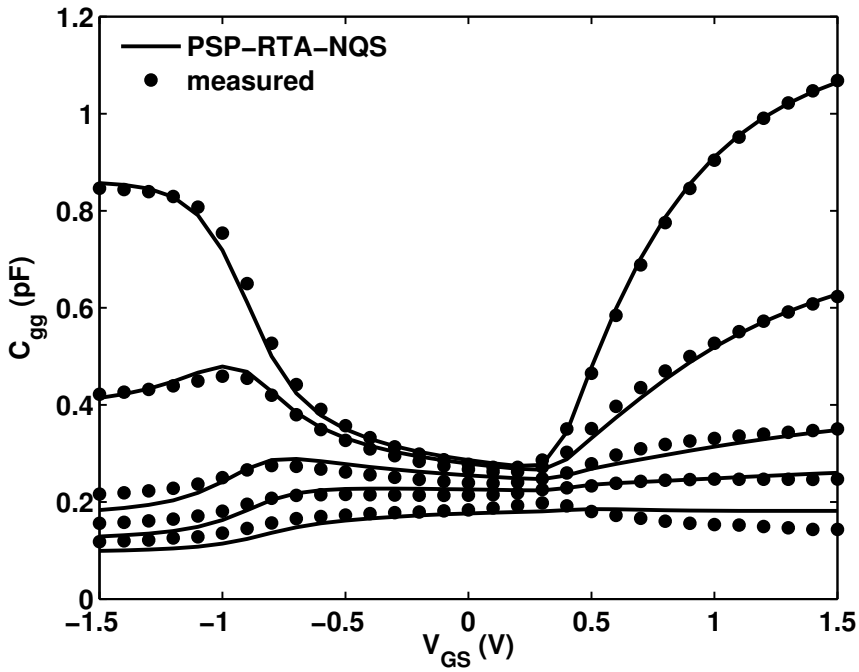

Fig. 5.8. Measured PMOS data and PSP-RTA-NQS model with both R_{bulk} and R_{gate} included. $W/L = 10.0\mu\text{m}/1.2\mu\text{m}$, frequencies are 5, 10, 20, 30, and 50 GHz (top to bottom). $f_{\text{T}} = 0.71\text{GHz}$.

essentially appear in series in accumulation, hence, R_{bulk} should have the dominant effect on device behavior.

As one final option, Fig. 5.11 shows the measured data along with PSP-RTA-NQS simulations with all parameters kept at the same values as those used for Fig. 5.8, but with the QS, rather than RTA-NQS, version of PSP selected. Compared with Fig. 5.8, clearly, the behavior at the lower frequencies in strong inversion is dominated by NQS effects; however, a comparison of Figs. 5.9 and 5.11 shows that at higher frequencies, the influence of the gate resistance is more pronounced than the contribution of NQS effects. To model accurately, the high frequency behavior of MOS capacitance over all regions of operation, it is, therefore, necessary to account

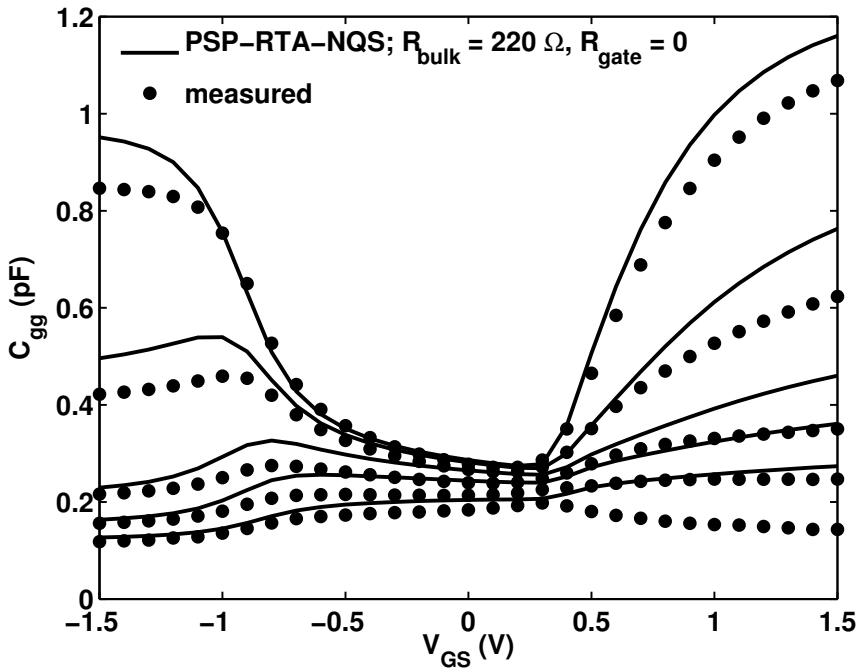

Fig. 5.9. Effect of not accounting for R_{gate} – measured PMOS data and PSP-RTA-NQS model with only R_{bulk} included. Same device and frequencies as Fig. 5.8.

for all of R_{bulk}, R_{gate}, and NQS effects.

5.5. Summary

In this chapter, we present an analytic solution for and measurements, TCAD simulations, and PSP-RTA-NQS model simulations of the frequency dependence of MOSFET gate capacitance. We clearly demonstrate that the frequency dependency of C_{gg} in accumulation and depletion is from R_{bulk} and, to a lesser extent, R_{gate} and not, as has been claimed previously, from NQS effects.

In inversion, R_{bulk} has a significantly smaller effect than in accumulation, but we show that it is important to account both for R_{gate} and for NQS effects to be able to model accurately the frequency dependency of C_{gg} in strong inversion.

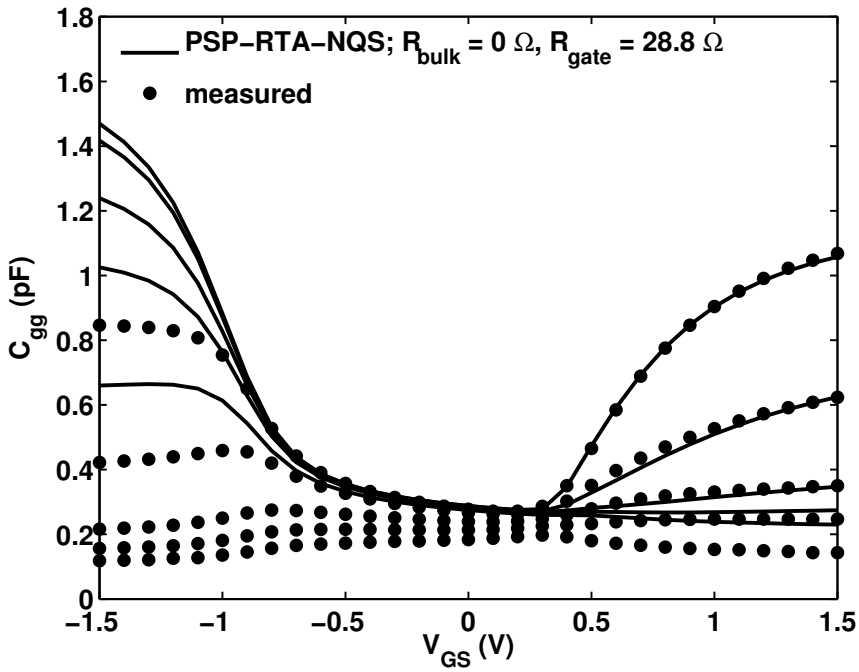

Fig. 5.10. Effect of not accounting for R_{bulk} – measured PMOS data and PSP-RTA-NQS model with only R_{gate} included. Same device and frequencies as Fig. 5.8.

Figs. 5.4 and 5.8 show the capability of PSP-RTA-NQS to fit TCAD simulations and measured data, respectively, when R_{bulk}, R_{gate}, and NQS effects are all taken into account.

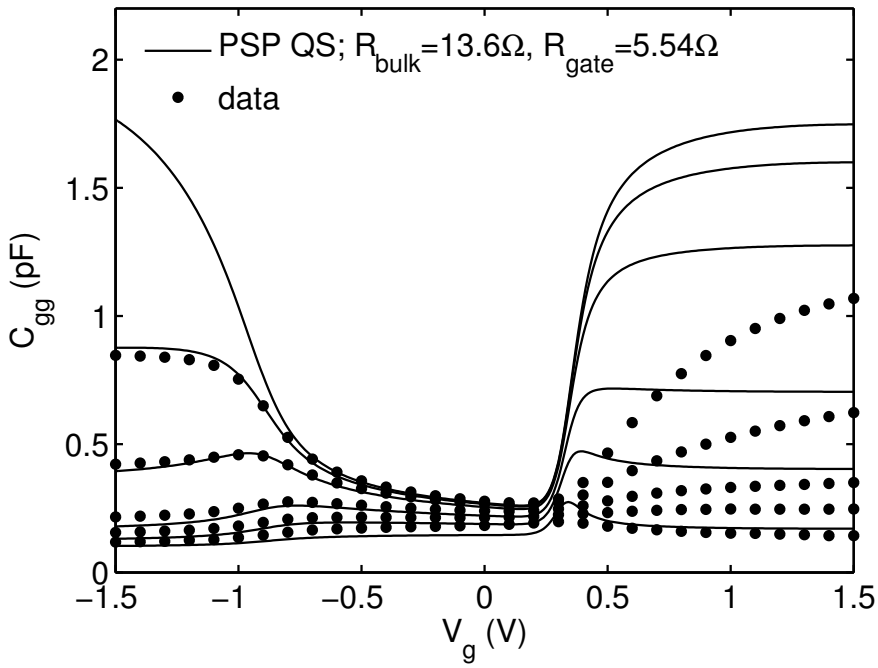

Fig. 5.11. Effect of not accounting for NQS effects – measured PMOS data and PSP-QS model with R_{bulk} and R_{gate} included. Same device as Fig. 5.8. In addition to the same frequencies as in Fig. 5.8, the curve for $f \ll f_{\text{T}}$ is included as well.

CHAPTER 6

Conclusions

6.1. Conclusion

It is possible to improve on the traditional form of the RTA NQS model by not using the RTA for the bulk and gate charges. The new formulation retains the speed and simplicity of the original RTA NQS approach but improves the accuracy of the model, especially for the gate and bulk currents. The PSP-based formulation of the improved RTA NQS model is verified by comparison with TCAD simulations and experimental data. The new model is coded in verilog-A and several circuit applications are performed to illustrate the new approach and to demonstrate its convergence properties. In addition, a new and simple technique to characterize NQS and gate resistance, R_{g}, MOS model parameters from measured data has been presented.

The effects of bulk resistance on the MOSFET gate capacitance is investigated both theoretically and experimentally to separate it from the NQS effects.

REFERENCES

[1] Y. Tsividis and C. McAndrew, *Operation and Modeling of the MOS Transistor, 3rd Ed.*, Oxford University Press, Oxford, New York, 2011.

[2] J.-M. Sallese, M. Bucher, and C. Lallement, "Improved analytical modeling of polysilicon depletion in MOSFETs for circuit simulation," *Solid-State Electronics*, vol. 44, pp. 905–912, 2000.

[3] A. S. Porret and J. M. Sallese, "A compact non-quasi-static extension of a charge-based MOS model," *Solid-State Electronics*, vol. 48, pp. 1647–1654, 2001.

[4] A. C. T. Aarts, G. D. J. Smit, A. J. Scholten, and D. B. M. Klaassen, "A PSP-based small-signal MOSFET model for both quasi-static and nonquasi-static operations," *IEEE Trans. Electron Devices*, vol. 55, pp. 1424–1432, 2008.

[5] Z. Zhu, G. Gildenblat, C. C. McAndrew, and I.-S. Lim, "Modeling the frequency dependence of MOSFET gate capacitance," in *IEEE International Conf. on Microelectronic Test Structures*, 2011, pp. 13–18.

[6] H. Johnson, "A high-frequency representation of the MOS transistor," in *Proc. of the IEEE*, 1966, pp. 1970–1971.

[7] D. H. Treleaven and F. N. Trofimenkoff, "MOS FET equivalent circuit at pinchoff," in *Proc. of the IEEE*, 1966, pp. 1223–1224.

[8] H. C. de Graaff, "High frequency measurements of thin-film transistors," *Solid-State Electronics*, vol. 10, pp. 51–56, 1967.

[9] M. B. Das, "Generalized high-frequency network theory of field-effect transistors," in *IEE Proceedings*, 1967, pp. 50–59.

[10] E. M. Cherry, "Small-signal high-frequency response of the insulated gate field-effect transistor," *IEEE Trans. Electron Devices*, vol. ED-17, pp. 569–577, 1970.

[11] M. V. Balakirev and V. M. Bogachev, "Frequency and transient characteristics of metal oxide semiconductor transistors and synthesis of their equivalent circuits," in *Radio Engineering and Electronics Physics*, 1971, pp. 1884–1897.

[12] M. Reiser, "A two-dimensional numerical FET model for dc, ac and large-signal analysis," *IEEE Trans. Electron Devices*, vol. ED-20, pp. 35–45, 1976.

[13] U. Kumar and S. C. Dutta Roy, "A simple small-signal two-part MOST model for the pre-pinchoff region," *Solid-State Electronics*, vol. 20, pp. 1021–1022, 1977.

[14] U. Kumar, "A simple two-part model of the metal oxide semiconductor transistor," *Microelectronics Journal*, vol. 10, pp. 50–53, 1978.

[15] J. I. Arreola, *Equivalent circuit modeling of the large signal transient response of four-terminal MOS field-effect transistors*, Ph.D. thesis, University of Florida, 1978.

[16] J. A. Robinson, Y. A. El-Mansy, and A. R. Boothroyd, "A general four-terminal charging-current model for the insulated-gate field effect transistor," *Solid-State Electronics*, vol. 23, pp. 405–414, 1980.

[17] S. Y. Oh, "A simplified two-dimensional numerical analysis of MOS devices including transient phenomena," Tech. Rep., Integrated Circuits Laboratory, Stanford Univerisy, Stanford, Calif., 1981.

[18] R. Conilogue and C. Viswanathan, "A complete large and small signal charge model for a MOS transistor," in *IEEE IEDM Tech. Digest*, 1982, pp. 654–657.

[19] K. Y. Tong, "AC model for MOS transistors from transient-current computations," *IEE Proceedings*, vol. 130, pp. 33–36, 1983.

[20] C. Turchetti, G. Masetti, and Y. P. Tsividis, "On the small-signal behavior of the MOS transistor in quasi-static operation," *Solid-State Electronics*, vol. 26, pp. 941–949, 1983.

[21] J. J. Paulos, *Measurement and modeling of small-geometry MOS transistor capacitances*, Ph.D. thesis, Massachusetts Institute of Technology, Cambridge, 1984.

[22] C. Turchetti and G. Masetti, "A CAD-oriented analytical MOSFET model for high-accuracy applications," *IEEE Trans. Comput.-Aid. Des.*, vol. 3, pp. 117–122, 1984.

[23] K.-W. Chai and J. J. Paulos, "Comparison of quasi-static and non-quasi-static capacitance models for the four-terminal MOSFET," *IEEE Electron Device Lett.*, vol. EDL-8, pp. 377–379, 1987.

[24] U. Kumar, "Modified charge-control model for MOS transistors in pre-saturation region," *Solid-State Electronics*, vol. 31, pp. 377–379, 1988.

[25] T. Smedes and F. M. Klaassen, "An analytical model for the non-quasi-static small-signal behavior of submicron MOSFETs," *Solid-State Electronics*, vol. 38, pp. 121–130, 1995.

[26] J. Katzenelson and A. Unikovski, "A network charge-oriented MOS transistor model," *International Journal of High Speed Electronics and Systems*, vol. 6, pp. 285–316, 1995.

[27] V. I. Kol'dyaev, A. Clerix, and L. Deferm, "Closed-form frequency dependent gate-to-channel capacitance model for submicron MOSFET's," in *Proceedings of the 36th European Solid-State Device Research Conference*, 1996, pp. 679–682.

[28] Y. Niitsu, "Simple small-signal model for 3-port MOS transistors," *IEICE Trans. Electron.*, vol. E79-C, pp. 1950–1960, 2000.

[29] M. Chan, K. Y. Hui, C.-M. Hu, and P. K. Ko, "A robust and physical BSIM3 non-quasi-static transient and ac small-signal model for circuit cimulation," *IEEE Trans. Electron Devices*, vol. 45, pp. 834–841, 1998.

[30] X. Jin, K. Cao, J.-J. Ou, W. Liu, Y. Cheng, M. Matloubian, and C. Hu, "An accurate non-quasistatic MOSFET model for simulation of RF and high speed circuits," in *2000 Symposium on VLSI technology*, 2000, pp. 196–197.

[31] A. J. Scholten, L. F. Tiemeijer, P. W. H. de Vreede, and D. B. M. Klaassen, "A large signal non-quasi-static MOS model for RF circuit simulation," in *IEEE IEDM Tech. Digest*, 1999, pp. 163–166.

[32] H. Wang, T.-L. Chen, and G. Gildenblat, "Quasi-static and nonquasi-static compact MOSFET models based on symmetric linearization of the bulk and inversion charges," *IEEE Trans. Electron Devices*, vol. 50, pp. 2262–2272, 2003.

[33] H. Wang, X. Li, G. Gildenblat, R. van Langevelde, G. D. J. Smit, A. J. Scholten, and D. B. M. Klaassen, "A unified nonquasi-static MOSFET model

for large-signal and small-signal simulation," *IEEE Trans. Electron Devices*, vol. 53, pp. 2035–2043, 2006.

[34] D. Navarro, Y. Takeda, M. Miyake, N. Nakayama, K. Machida, T. Ezaki, H. J. Mattausch, and M. Miura-Mattausch, "A carrier-transit-delay-based nonquasi-static MOSFET model for circuit simulation and its application to harmonic distortion analysis," *IEEE Trans. Electron Devices*, vol. 53, pp. 2025–2034, 2006.

[35] M. Bagheri and Y. Tsividis, "A small-signal dc-to-high-frequency nonquasi-static model for the four-terminal MOSFET valid in all regions of operation," *IEEE Trans. Electron Devices*, vol. ED-32, pp. 2383–2391, 1985.

[36] P. J. V. Vandeloo and W. M. C. Sansen, "Modeling of the MOS transistor for high frequency analog design," *IEEE Trans. Comput.-Aid. Des.*, vol. 8, pp. 713–723, 1989.

[37] L.-J. Pu and Y. P. Tsividis, "Harmonic distortion of the four-terminal MOSFET in non-quasistatic operation," *IEE Proceedings*, vol. 137, pp. 325–332, 1990.

[38] L.-J. Pu and Y. P. Tsividis, "Small-signal parameters and thermal noise of the four-terminal MOSFET design," *Solid-State Electronics*, vol. 33, pp. 713–723, 1990.

[39] K. A. Sakallah, Y.-T. Yen, and S. S. Greenberg, "A first-order charge conserving MOS capacitance model," *IEEE Trans. on Computer-Aided Design*, vol. 9, pp. 99–108, 1990.

[40] P. Roblin, S. C. Kang, and W.-R. Liou, "Improved small-signal equivalent circuit model and large-signal state equations for the MOSFET/MODFET wave equation," *IEEE Trans. Electron Devices*, vol. 38, pp. 1706–1718, 1991.

[41] H. J. Park, K. Y. Hui, P. K. Ko, and C.-M. Hu, "A non-quasi-static MOSFET model for SPICE-AC analysis," *IEEE Trans. on Computer-Aided Design*, vol. 11, pp. 1247–1257, 1992.

[42] S. C. Kang and P. Roblin, "Optimal second-order small-signal model for long- and short-channel three-terminal MOSFET/MODFET wave equation," *IEEE Trans. Electron Devices*, vol. 39, pp. 1909–1915, 1992.

[43] R. Singh, A. Juge, R. Joly, and G. Mortin, "An investigation into the non-quasistatic effects in MOS devices with on-wafter S-parameter techniques," in *IEEE International Conf. on Microelectronic Test Structures*, 1993, pp. 21–25.

[44] J. M. Sallese and A. S. Porret, "A novel approach to charge-based non-quasi-static model of the MOS transistor valid in all modes of operation," *Solid-State Electronics*, vol. 44, pp. 887–894, 2000.

[45] Y. Niitsu, "Non-quasi-static small signal model of four-terminal MOS transistors," *IEICE Trans. Electron.*, vol. E83-C, pp. 1950–1960, 2000.

[46] S. Lee and H. K. Yu, "Determining non-quasi-static small-signal equivalent circuit of a RF silicon MOSFET," *Solid-State Electronics*, vol. 45, pp. 359–364, 2001.

[47] R. van Longevelde, A. J. Scholten, L. F. Tiemerjer, R. J. Havens, and D. B. M. Klaassen, "RF applications of MOS model 11," in *in 2002 International Conference on Modeling and Simulation of Microsystems*, 2002.

[48] A. S. Roy, J. M. Vasi, and M. B. Patil, "A new approach to model nonquasi-static (NQS) effects for MOSFETs - part I: Large-signal analysis," *IEEE Trans. Electron Devices*, vol. 50, pp. 2393–2400, 2003.

[49] A. S. Roy, J. M. Vasi, and M. B. Patil, "A new approach to model nonquasi-static (NQS) effects for MOSFETs–Part II: Small-signal analysis," *IEEE Trans. Electron Devices*, vol. 50, pp. 2401–2407, 2003.

[50] A. S. Roy, C. C. Enz, and J.-M. Sallese, "Compact modeling of anomalous high-frequency behavior of MOSFET's small-signal NQS parameter in presence of velocity saturation," *IEEE Trans. Electron Devices*, vol. 53, pp. 2044–2050, 2006.

[51] A. B. Bhattacharyya, *Compact MOSFET Models for VLSI Design*, Wiley, John & Sons (Asia), Singapore, 2009.

[52] G. Gildenblat, X. Li, W. Wu, H. Wang, A. Jha, R. van Langevelde, G. D. J. Smit, A. J. Scholten, and D. B. M. Klaassen, "PSP: An advanced surface-potential-based MOSFET model for circuit simulation," *IEEE Trans. Electron Devices*, vol. 53, pp. 1979–1993, 2006.

[53] G. Gildenblat, W. Wu, X. Li, R. V. Langevelde, A. J. Scholten, G.-J. Smit, and D. B. M. Klaassen, "Surface-potential-based compact model of bulk

MOSFET," in *Compact Modeling: Principles, Techniques and Applications*, G Gildenblat, Ed., chapter 1. Springer, New York, 2010.

[54] K.-W. Chai and J. J. Paulos, "Unified nonquasi-static modeling of the long-channel four-terminal MOSFET for large- and small-signal analyses in all operating regimes," *IEEE Trans. Electron Devices*, vol. 36, pp. 2513–2520, 1989.

[55] W. C. Stiebler, "A non-quasi-static relaxation-time small-signal HEMT model compatible with large-signal modeling," in *Proceeding of European Microwave Integrated Circuit Conference*, 2006, pp. 387–390.

[56] M. Miura-Mattausch, H. J. Mattausch, and Ezaki T., *The physics and Modeling of MOSFETs*, World Scientific, 2008.

[57] W. Liu, *MOSFET Models for SPICE Simulation Including BSIM3v3 and BSIM4*, Wiley, New York, 2001.

[58] J. Victory, C. C. McAndrew, and K. Gullapalli, "A time-dependent, surface-potential based compact model for MOS capacitors," *IEEE Electron Device Lett.*, vol. 22, pp. 245–247, 2001.

[59] J. Victory, Z. X. Yan, G. Gildenblat, C. C. McAndrew, and J. Zheng, "A physically based, scalable MOS varactor model and extraction methodology for RF applications," *IEEE Trans. Electron Devices*, vol. 52, pp. 1343–1353, 2005.

[60] G. Gildenblat, Z. Zhu, and W. Wu, "Analytical expression for the bias and frequency-dependent capacitance of MOS varactors," *IEEE Trans. Electron Devices*, vol. 54, pp. 3107–3108, 2007.

[61] Z. Zhu, G. Gildenblat, J. Victory, and C. C. McAndrew, "Surface-potential-based MOS varactor model," in *Compact Modeling: Principles, Techniques and Applications*, G Gildenblat, Ed., chapter 11. Springer, New York, 2010.

[62] G. D. J. Smit, A. J. Scholten, and D. B. M. Klaassen, "RF benchmark tests for compact MOS models," in *IEEE Radio Frequency Integrated Circuits Symposium*, 2010, pp. 593–596.

[63] D. P. Foty, *MOSFET Modeling with SPICE: Principles and Practice*, Pretice Hall PTR, Upper Saddle River, New Jersey, 1997.

[64] Y. Cheng and C. Hu, *MOSFET modeling and BSIM3 user's guide*, Kluwer Academic Publishers, Boston MA, 1999.

[65] "BSIM3 model website," *http://www-device.eecs.berkley.edu/∼bsim3 /latenews.html*, Accessed Aug. 2011.

[66] "BSIM4 model website," *http://www-device.eecs.berkley.edu/∼bsim3 /bsim4.html*, Accessed Aug. 2011.

[67] M. Miura-Mattausch, H. Ueno, H. J. Mattausch, S. Kumashiro, T. Yamaguchi, K. Yamashita, and N. Nakayama, "HISIM: Self-consistent surface-potential MOS-model valid down to sub-100nm technologies," in *2002 International Conference on Modeling and Simulation of Microsystems*, 2002, pp. 678–681.

[68] M. Miura-Mattausch, H. Ueno, M. Tanaka, H. J. Mattausch, S. Kumashiro, T. Yamaguchi, K. Yamashita, and N. Nakayama, "HiSIM: A MOSFET model for circuit simulation connecting circuit performance with technology," in *IEEE IEDM Tech. Digest*, 2002, pp. 109–112.

[69] J. A. Geurst, "Calculation of high-frequency characteristics of thin-film transistors," *Solid-State Electronics*, vol. 8, pp. 88–90, 1965.

[70] D. B. Candler and A. G. Jordan, "Small-signal, high-frequency analysis of insulated-gate field-effect transistor," *Int. J. Electron.*, vol. 19, pp. 181–196, 1965.

[71] J. R. Hauser, "Small-signal properties of field-effect devices," *IEEE Trans. Electron Devices*, vol. ED-12, pp. 605–618, 1965.

[72] M. H. White and R. C. Gallagher, "Metal-oxide-semiconductor (MOS) small signal equivalent circuit," in *Proc. of the IEEE*, 1965, pp. 314–315.

[73] W. Fischer, "Equivalent circuit and gain of MOS field-effect transistor," *Solid-State Electronics*, vol. 9, pp. 71–81, 1966.

[74] J. R. Burns, "High-frequency characteristics of insulated-gate field-effect transistor," *RCA Review*, vol. 28, pp. 385–418, 1967.

[75] J. A. van Nielen, "A simple and accurate approximation to the high-frequency characteristics of insulated-gate field-effect transistors," *Solid-State Electronics*, vol. 12, pp. 826–829, 1969.

[76] J. W. Haslett and F. N. Trofimenkoff, "Small-signal, high-frequency equivalent circuit for the metal-oxide-semiconductor field-effect transistor," *IEE Proceedings*, vol. 116, pp. 699–702, 1969.

[77] R. S. C. Cobbold, *Theory and Applications of Field-Effect Transistors*, Wiley-Interscience, New York, 1970.

[78] J. J. Paulos and D. A. Antoniadis, "Limitations of quasi-static capacitance models for the MOS transistor," *IEEE Electron Device Lett.*, vol. EDL-4, pp. 221–224, 1983.

[79] R. M. D. A. Velghe, D. B. M. Klaassen, and F. M. Klaassen, "Compact MOS modeling for analog circuit simulation," in *IEEE IEDM Tech. Digest*, 1993, pp. 485–488.

[80] "MOS model 11," *http://www.nxp.com/models/mos_models/model11/index.html*, Accessed Aug. 2011.

[81] P. Bendix, "Detailed Comparison of the SP2001, EKV, and BSIM3 Models," in *International Conference on Modeling and Simulation of Microsystems*, 2002, pp. 649 – 652.

[82] G. Gildenblat and T.-L. Chen, "Overview of an Advanced Surface-Potential-Based MOSFET Model (SP)," in *Tech. Proc. of the 5th International Conference on Modeling and Simulation of Microsystems (ICMSM'02)*, 2002, pp. 657–661.

[83] G. Gildenblat, T.-L. Chen, X. Gu, H. Wang, and X. Cai, "SP: An advanced surface-potential-based compact MOSFET model," in *Proc. IEEE Custom Integrated Circuit Conference*, 2003, pp. 233–240.

[84] G. Gildenblat, X. Cai, T.-L. Chen, X. Gu, and H. Wang, "Reemergence of the surface-potential-based compact MOSFET models (invited)," in *IEEE IEDM Tech. Digest*, 2003, pp. 863–866.

[85] G. Gildenblat, H. Wang, T.-L. Chen, X. Gu, and X. Cai, "SP: An advanced surface-potential-based compact MOSFET model," *IEEE J. Solid-State Circuits*, vol. 39, pp. 1394–1406, 2004.

[86] P. Bendix, P. Rakers, P. Wagh, L. Lemaitre, W. Grabinski, C. C. McAndrew, X. Gu, and G. Gildenblat, "RF distortion analysis with compact MOSFET models," in *Proc. IEEE Custom Integrated Circuit Conference*, 2004, pp. 9–12.

[87] G. Gildenblat, X. Li, H. Wang, W. Wu, R. van Langevelde, A. J. Scholten, G. D. J. Smit, and D. B. M. Klaassen, "Introduction to PSP MOSFET model," in *Technical Proceedings of the 2005 Workshop on Compact Modeling*, 2005, pp. 19–24.

[88] "PSP model website," *http://pspmodel.asu.edu/*, Accessed Aug. 2011.

[89] C. A. Desoer and E. S. Kuh, *Basic Circuit Theory*, McGraw-Hill, New York, 1969.

[90] W. H. Kim and H. E. Meadows Jr, *Modern Network Analysis*, John Wiley, New York, 1971.

[91] W. H. Hayt and J. E. Kemmerly, *Engineering Circuit Analysis*, McGraw-Hill, New York, 1993.

[92] M. Bagheri, "Improving the non-quasi-static weak-to-strong inversion four-terminal MOSFET model," *IEEE Trans. Electron Devices*, vol. ED-34, pp. 2558–2560, 1987.

[93] J. J. Paulos, D. A. Antoniadis, and Y. P. Tsividis, "Measurement of intrinsic capacitances of MOS transistors," in *IEEE J. Solid-State Circuits*, 1982, pp. 238–239.

[94] C. C. Enz, F. Krummernacher, and E. A. Vittoz, "An analytical MOS transistor model valid in all regions of operation and dedicated to low-voltage and low-current applications," *Analog Integr. Circuits and Signal Process.*, vol. 8, pp. 83–114, 1995.

[95] C. Enz, "MOS transistor modeling for RF integrated circuit design," in *Proc. IEEE Custom Integrated Circuit Conference*, 2000, pp. 189–196.

[96] C. Enz and Y. Cheng, "MOS transistor modeling for RF IC design," *IEEE J. Solid-State Circuits*, vol. 35, pp. 186–201, 2000.

[97] C. Enz, "An MOS transistor model for RF IC design valid in all regions of operation," *IEEE Trans. Microw. Theory Tech.*, vol. 50, pp. 342–359, 2002.

[98] C. Enz, M. Bucher, A.-S. Porret, J.-M. Sallese, and F. Krummenacher, "The foundations of the EKV MOS transistor charge-based model," in *The Fifth International Conference on Modeling and Simulation of Microsystems*, 2002, pp. 666–669.

[99] D. E. Ward and R. W. Dutton, "A charge-oriented model for MOS transistor capacitances," *IEEE J. Solid-State Circuits*, vol. SC-13, pp. 703–708, 1978.

[100] S. Y. Oh, D. E. Ward, and R. W. Dutton, "Transient analysis of MOS transistors," *IEEE J. Solid-State Circuits*, vol. SC-15, pp. 636–643, 1980.

[101] W. Liu, *Fundamentals of III-V Devices: HBTs, MESFETs, and HFETs/HEMTs*, John Wiley & Sons, Oxford, New York, 1999.

[102] C. H. Oxley and M. J. Uren, "Measurements of unity gain cutoff frequency and saturation velocity of a GaN HEMT transistor," *IEEE Trans. Electron Devices*, vol. 52, pp. 165–169, 2005.

[103] M. Bucher, C. Lallement, C. Enz, and F. Krummenacher, "Accurate MOS Modelling for Analog Circuit Simulation Using the EKV Model," in *IEEE International Symposium on Circuits and Systems*, 1996, vol. 4, pp. 703–706.

[104] Q. Huang, F. Piazza, P. Orsatti, and T. Ohguro, "The impact of scaling down to deep submicron on CMOS RF circuits," *IEEE J. Solid-State Circuits*, vol. 33, pp. 1023–1036, 1998.

[105] L. F. Tiemeijer and D. B. M. Klaassen, "Geometry scaling of the substrate loss of RF MOSFETs," in *Proc. Eur. Solid-State Dev. Res. Conf.*, 1998, pp. 481–483.

[106] B. Razavi, *RF Microelectronics*, Prentice Hall, Upper Saddle River, New Jewsy, 1998.

[107] T. H. Lee, "CMOS RF:(still) no longer an oxymoron," in *IEEE Radio Frequency Integrated Circuits Symposium*, 1999, pp. 3–6.

[108] Y. H. Wu, A. Chin, C. S. Liang, and C. C. Wu, "The performance limiting factors as rf mosfets scale down," in *IEEE Radio Frequency Integrated Circuits Symposium*, 2000, pp. 151–155.

[109] L. F. Tiemeijer, H. M. J. Boots, R. J. Havens, A. J. Scholten, P. W. H. de Vreede, P. H. Woerlee, A. Heringa, and D. B. M. Klaassen, "A record high 150GHz f_{max} realized at $0.18\mu m$ gate length in an industrial RF-CMOS technology," in *IEEE IEDM Tech. Digest*, 2001, pp. 223–226.

[110] J. Everard, *Fundamentals of RF Circuit Design with Low Noise Oscillators*, John Wiley and Sons, West Susses, England, 2001.

[111] P. H. Woerlee, M. J. Knitel, R. van Langevelde, D. B. M. Klaassen, L. F. Tiemeijer, A. J. Scholten, and A. T. A. Zegers van Duijnhoven, "RF-CMOS performance trends," *IEEE Trans. Electron Devices*, vol. 48, pp. 1776–1782, 2001.

[112] J. Schmitz, F. N. Cubaynes, R. J. Havens, R. de Kort, A. J. Scholten, and L. F. Tiemeijer, "Rf capacitance-voltage characterization of mosfets with high leakage dielectrics," *IEEE Electron Device Lett.*, vol. 24, pp. 37–39, 2003.

[113] R. Srinivasan and N. Bhat, "Effect of scaling on the non-quasi-static behaviour of the mosfet for rf ics," in *Proc. 16th Int VLSI Design Conf*, 2003, pp. 105–109.

[114] R. van Langevelde, J. C. J. Paasschens, A. J. Scholten, R. J. Havens, L. F. Tiemeijer, and D. B. M. Klaassen, "New compact model for induced gate current noise," in *IEEE IEDM Tech. Digest*, 2003, pp. 867–870.

[115] W.-K. Shih, S. Mudanai, R. Rios, P. Packan, D. Becher, R. Basco, C. Hung, and U. Jalan, "Predictive compact modeling of NQS effects and thermal noise in 90nm mixed signal/RF CMOS technology," in *IEEE IEDM Tech. Digest*, 2004, pp. 747–750.

[116] D. B. M. Klaassen, R. Langevelde, and A. J. Scholten, "Compact CMOS modelling for advanced analogue and RF applications," *IEICE transactions on electronics*, vol. 87, no. 6, pp. 854–866, 2004.

[117] I. Gutiérrez, J. Meléndez, and E. Hernández, *Design and Characterization of Integrated Varactors for RF Applications*, Wiley, John & Sons, England, 2006.

[118] C. C. Enz and E. A. Vittoz, *Charge-Based MOS Transistor Modeling: The EKV Model for Low-Power and RF IC Design*, John Wiley & Sons Ltd, 2006.

[119] A. J. Scholten, G. D. J. Smit, B. A. De Vries, L. F. Tiemeijer, J. A. Croon, D. B. M. Klaassen, R. van Langevelde, Xin Li, Weimin Wu, and G. Gildenblat, "The new CMC standard compact MOS model PSP: Advantages for RF applications," *IEEE J. Solid-State Circuits*, vol. 44, pp. 1415–1424, 2009.

[120] T.-L. Chen and G. Gildenblat, "Symmetric bulk charge linearization in charge-sheet MOSFET model," *IEE Electron. Lett.*, vol. 37, pp. 791–793, 2001.

[121] L. Lemaitre, C. McAndrew, and S. Hamm, "ADMS-automatic device model synthesizer," in *Proc. IEEE Custom Integrated Circuit Conference*, 2002, pp. 27–30.

[122] C.-L. Huang and N. D. Arora, "Measurements and modeling of mosfet i-v characteristics with polysilicon depletion effect," *IEEE Trans. Electron Devices*, vol. 40, pp. 2330–2337, 1993.

[123] R. Rios, N. D. Arora, and C.-L. Huang, "An analytic polysilicon depletion effect model for mosfets," *IEEE Electron Device Lett.*, vol. 15, pp. 129–131, 1994.

[124] G. Gildenblat, T.-L. Chen, and P. Bendix, "Analytic approximation for pertubation of MOSFET surface potential by polysilicon depletion layer," *IEE Electron. Lett.*, vol. 35, pp. 1974–1976, 1999.

[125] J. M. Sallese, M. Bucher, and C. Lallement, "Improved analysical modeling of polysilicon depletion in MOSFETs for circuit simulation," *Solid-State Electronics*, vol. 44, pp. 905–912, 2000.

[126] F. Stern, "Quantum properties of surface space-charge layers," *CRC Crit. Rev. Solid State Sci.*, pp. 499–514, 1974.

[127] R. Rios and N. D. Arora, "Determination of ultra-thin gate oxide thicknesses for CMOS," in *IEEE IEDM Tech. Digest*, 1994, pp. 613–616.

[128] M. J. van Dort, P. H. Woerlee, and A. J. Walker, "A simple model for quantisation effect in heavily-doped MOSFETs at inversion conditions," *Solid-State Electronics*, vol. 37, pp. 411–414, 1994.

[129] X. Gu and G. Gildenblat, "Charge-Sheet MOSFET model with surface degeneracy and freezeout," in *International Semiconductor Device Research Symposium*, 2001, p. 102.

[130] Xiaodong Jin, Jia-Jiunn Ou, Chih-Hung Chen, Weidong Liu, M. J. Deen, P. R. Gray, and Chenming Hu, "An effective gate resistance model for CMOS RF and noise modeling," in *IEEE IEDM Tech. Digest*, 1998, pp. 961–964.

[131] Y. Cheng and M. Matloubian, "Frequency-dependent resistive and capacitive components in RF MOSFETs," *IEEE Electron Device Lett.*, vol. 22, pp. 333–335, 2001.

[132] R. T. Chang, M.-T. Yang, P. P. C. Ho, Y.-J. Wang, Y.-T. Chia, B.-K. Liew, C. P. Yue, and S. S. Wong, "Modeling and optimization of substrate resistance for RF-CMOS," *IEEE Trans. Electron Devices*, vol. 51, pp. 421–426, 2004.

[133] D. B. Leeson, "A simple model of feedback oscillator noise spectrum," in *Proc. of the IEEE*, 1966, vol. 54, pp. 329–330.

[134] M. Shoji, "Analysis of high-frequency thermal noise of enhancement mode mos field-effect transistors," *IEEE Trans. Electron Devices*, vol. ED-13, pp. 520–524, 1966.

[135] F. M. Klaassen and J. Prins, "Thermal noise of MOS transistors," *Philips Res. Reports*, vol. 22, pp. 505–514, 1967.

[136] H. E. Halladay and A. Van Der Ziel, "On the high frequency excess noise and equivalent circuit representation of the mos-fet with n-type channel," *Solid-State Electronics*, vol. 12, pp. 161–176, 1969.

[137] F. M. Klaassen and J. Prins, "Noise of field-effect transistors at very high frequencies," *IEEE Trans. Electron Devices*, vol. ED-16, pp. 952–957, 1969.

[138] P. S. Rao and A. van Der Ziel, "Noise and y-parameters in mos fet's," *Solid-State Electronics*, vol. 14, pp. 939–944, 1971.

[139] E. W. Kirk and A. van Der Ziel, "Induced gate noise in mos fet's," *Solid-State Electronics*, vol. 14, pp. 945–948, 1971.

[140] A. Ambrozy, *Electronic Noise*, McGraw-Hill, New York, 1982.

[141] A. van Der Ziel, *Noise in Solid-State Devices and Circuits*, Wiley, New York, 1986.

[142] D. P. Triantis, A. N. Birbas, and D. Kondis, "Thermal noise modeling for short-channel MOSFET's," *IEEE Trans. Electron Devices*, vol. 43, pp. 1950–1955, 1996.

[143] A. J. Scholten, L. F. Tiemeijer, R. van Langevelde, R. J. Havens, A. T. A. Z. Duijnhoven, and V. C. Venezia, "PSP: Noise modeling for RF CMOS circuit simulation," *IEEE Trans. Electron Devices*, vol. 50, pp. 618–632, 2001.

[144] C.-H. Chen, M. J. Deen, Y. Cheng, and M. Matloubian, "Extraction of the induced gate noise, channel noise, and their correlation in submicron MOSFETs from RF noise measurements," *IEEE Trans. Electron Devices*, vol. 48, pp. 2884–2892, 2001.

[145] A. J. Scholten, L. F. Tiemeijer, R. van Langevelde, R. J. Havens, A. T. A. Zegers van Duijnhoven, and V. C. Venezia, "Noise modeling for RF CMOS circuit simulation," *IEEE Trans. Electron Devices*, vol. 50, pp. 618–632, 2003.

[146] A. J. Scholten, L. F. Tiemeijer, A. T. A. Zegers van Duijnhoven, R. J. Havens, R. de Kort, R. van Langevelde, D. B. M. Klaassen, W. Jeamsaksiri, and R. M. D. A. Velghe, "Modeling and characterization of noise in 90-nm RF CMOS technology," in *18th International Conference on Noise and Fluctuations - ICNF2005*, 2005, pp. 735–740.

[147] A. S. Roy and C. C. Enz, "Compact modeling of thermal noise in the MOS transistor," *IEEE Trans. Electron Devices*, vol. 52, pp. 611–614, 2005.

[148] C. McAndrew, G. Coram, A. Blaum, and O. Pilloud, "Correlated noise modeling and simulation," in *Technical Proceedings of the 2005 Workshop on Compact Modeling*, 2005, pp. 40–45.

[149] "Taurus medici user's guide, version y-2006.06," 2006.

[150] M. C. A. M. Koolen, J. A. M. Geelen, and M. P. J. G. Versleijen, "An improved de-embedding technique for on-wafer high-frequency characterization," in *Proc. IEEE Bipolar BiCMOS Circuits and Technology Meeting*, 1991, pp. 188–191.

[151] E. S. Kuh and R. A. Rohrer, *Thoery of Linear Active Networks*, Holden-Day, Inc., 500 Sansome Street, San Francisco, California, 1967.

APPENDIX A

ADDITIONAL RESULTS FOR MODEL VALIDATION

Model validation against the experimental data was done over a wide range of gate biases, drain biases, and frequencies. These data can be generally categorized into two groups, i.e. those for $V_{\mathrm{DS}} = 0$ and those for $V_{\mathrm{DS}} \neq 0$. Because of limited space, only representative part of the validation results were presented in Chapter 3 which are for $V_{\mathrm{DS}} \neq 0$. Here, additional results for model validation including $V_{\mathrm{DS}} = 0$ are provided in Fig. A.1 - A.16. In these cases, the data are presented for swept gate biases from -1.5 to 1.5V with multiple frequencies up to roughly $3f_{\mathrm{T}}$. In the first section, results for $V_{\mathrm{DS}} = 0$ are presented.

A.1. $V_{\mathrm{DS}} = 0$ V

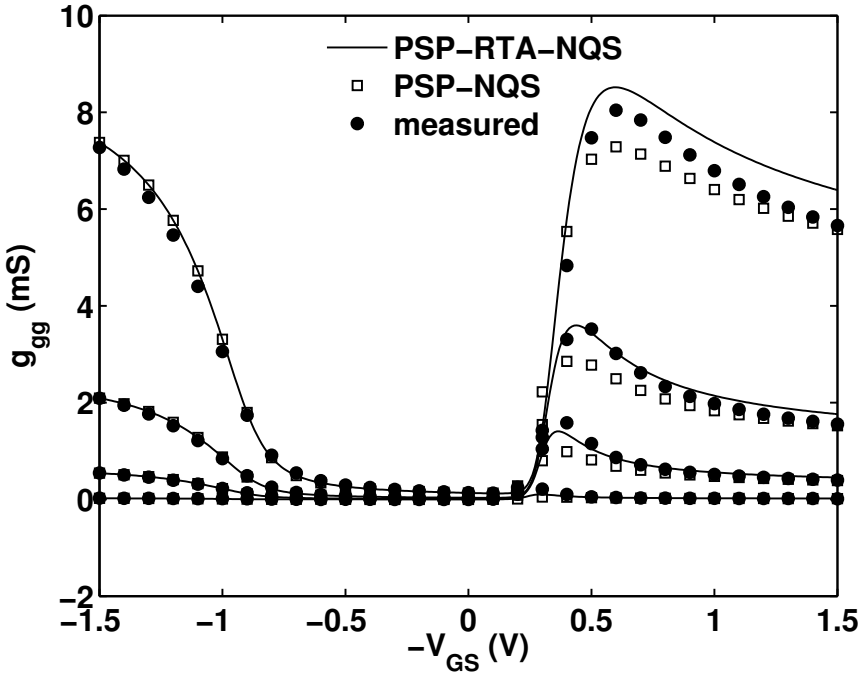

Fig. A.1. Comparison of model and measured data for a PMOS g_{gg} when $V_{\mathrm{DS}} =$ 0 V. Frequencies are 0.1, 0.5, 1 and 2 GHz where $f_{\mathrm{T}} = 0.71$ GHz. $L = 1.2$ μm, W $= 10$ μm.

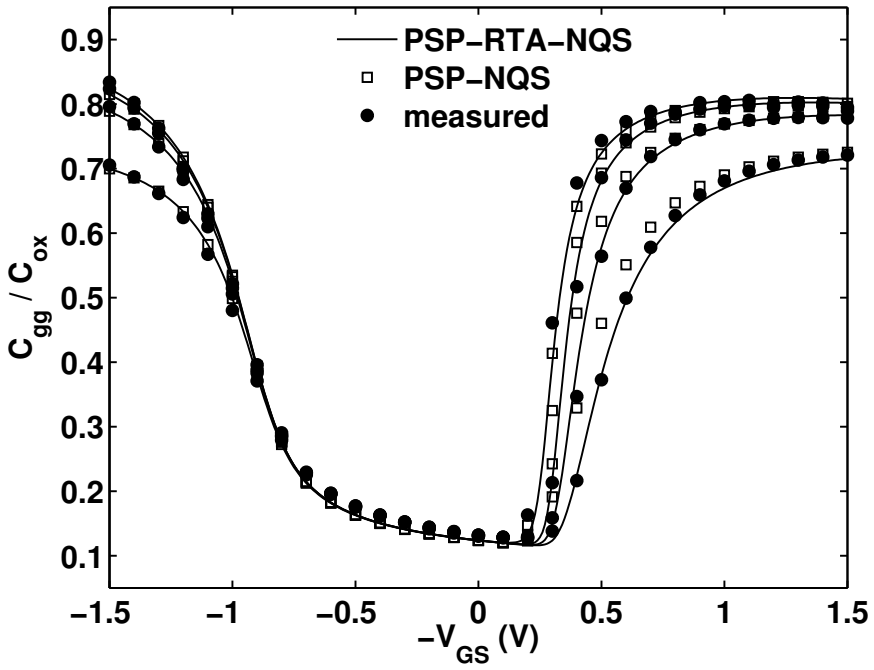

Fig. A.2. Comparison of model and measured data for a PMOS C_{gg} when $V_{\mathrm{DS}} =$ 0 V. Frequencies are 0.1, 0.5, 1 and 2 GHz where $f_{\mathrm{T}} = 0.71$ GHz. $L = 1.2$ μm, W $= 10$ μm.

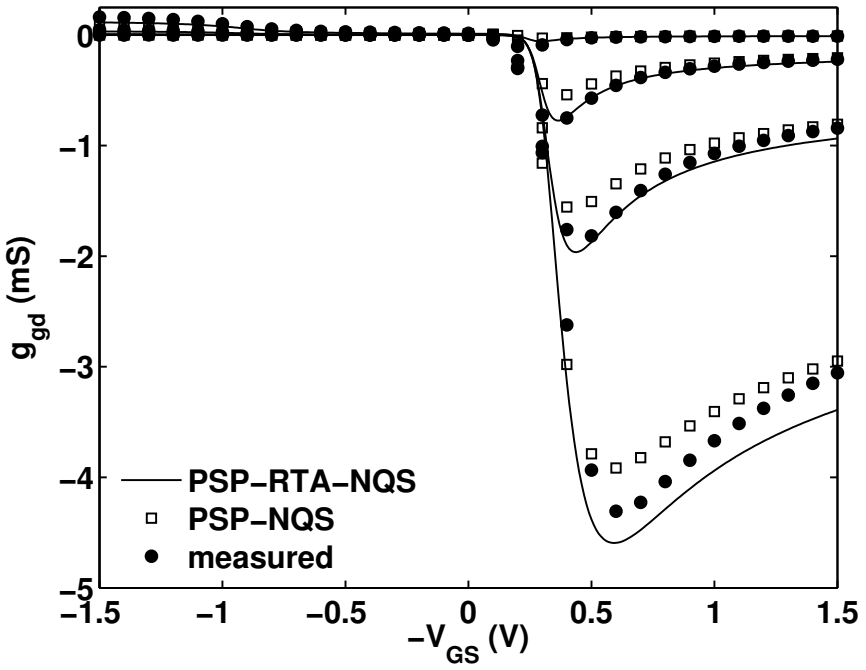

Fig. A.3. Comparison of model and measured data for a PMOS g_{gd} when $V_{\mathrm{DS}} =$ 0 V. Frequencies are 0.1, 0.5, 1 and 2 GHz where $f_{\mathrm{T}} = 0.71$ GHz. $L = 1.2$ μm, W $= 10$ μm.

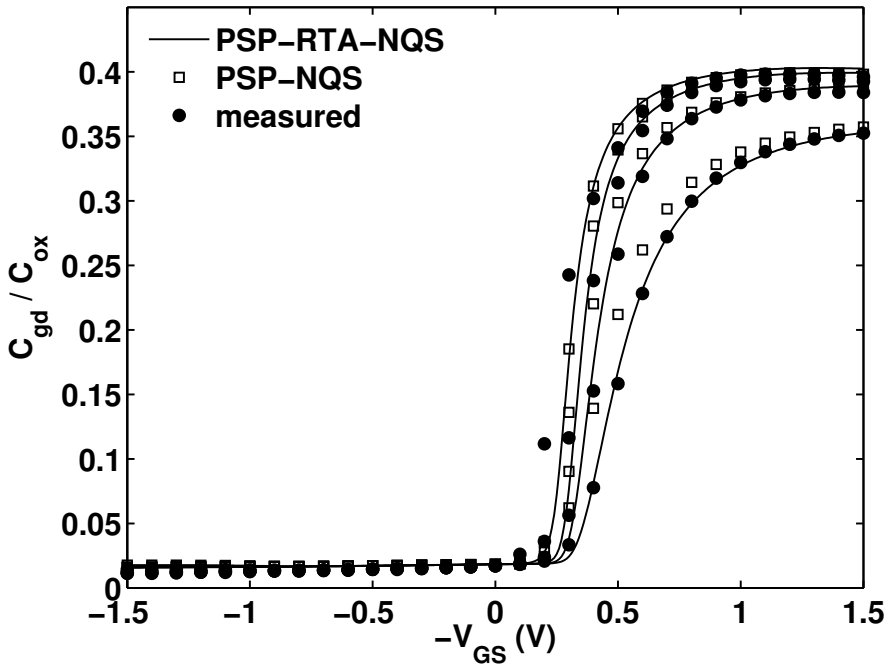

Fig. A.4. Comparison of model and measured data for a PMOS C_{gd} when $V_{\mathrm{DS}} =$ 0 V. Frequencies are 0.1, 0.5, 1 and 2 GHz where $f_{\mathrm{T}} = 0.71$ GHz. $L = 1.2$ μm, W $= 10$ μm.

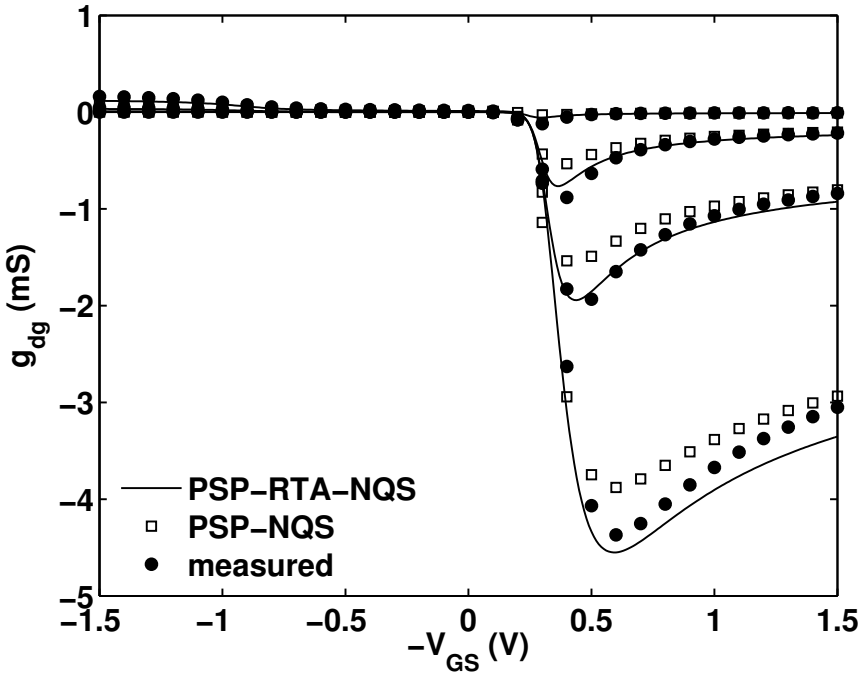

Fig. A.5. Comparison of model and measured data for a PMOS g_{dg} when $V_{\mathrm{DS}} =$ 0 V. Frequencies are 0.1, 0.5, 1 and 2 GHz where $f_{\mathrm{T}} = 0.71$ GHz. $L = 1.2$ μm, W $= 10$ μm.

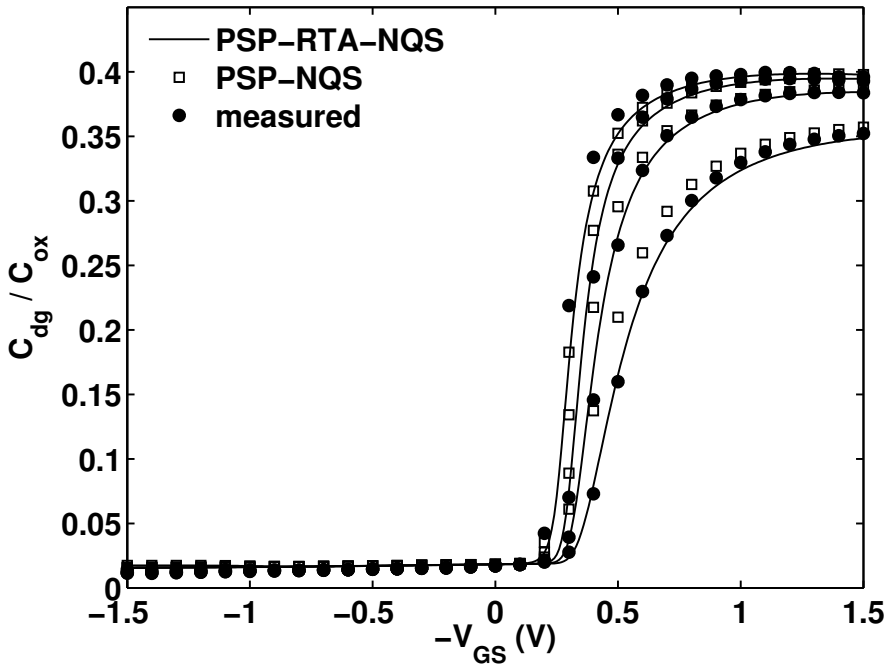

Fig. A.6. Comparison of model and measured data for a PMOS C_{dg} when $V_{\mathrm{DS}} =$ 0 V. Frequencies are 0.1, 0.5, 1 and 2 GHz where $f_{\mathrm{T}} = 0.71$ GHz. $L = 1.2$ μm, W $= 10$ μm.

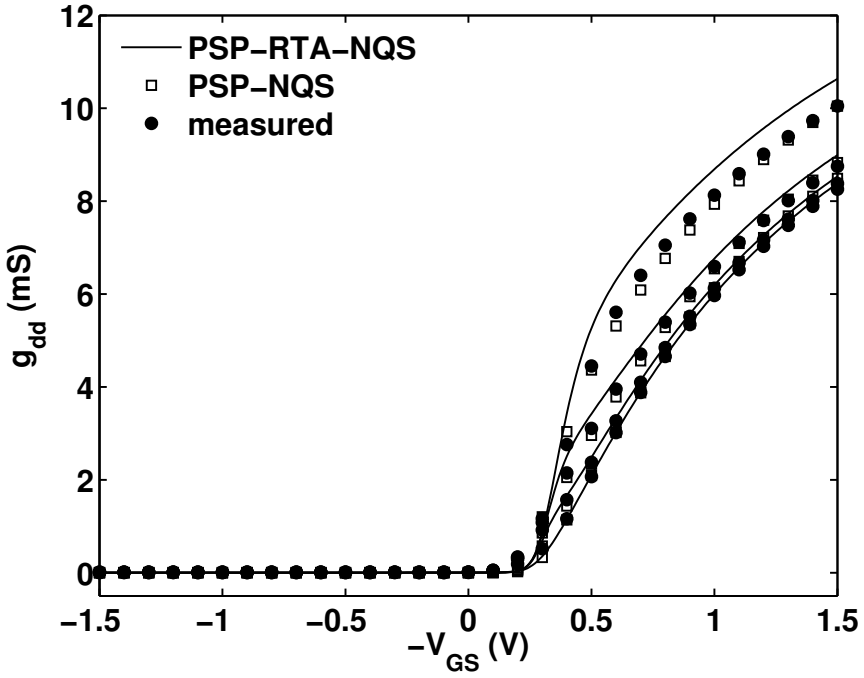

Fig. A.7. Comparison of model and measured data for a PMOS g_{dd} when $V_{\mathrm{DS}} = 0$ V. Frequencies are 0.1, 0.5, 1 and 2 GHz where $f_{\mathrm{T}} = 0.71$ GHz. $L = 1.2$ μm, $W = 10$ μm.

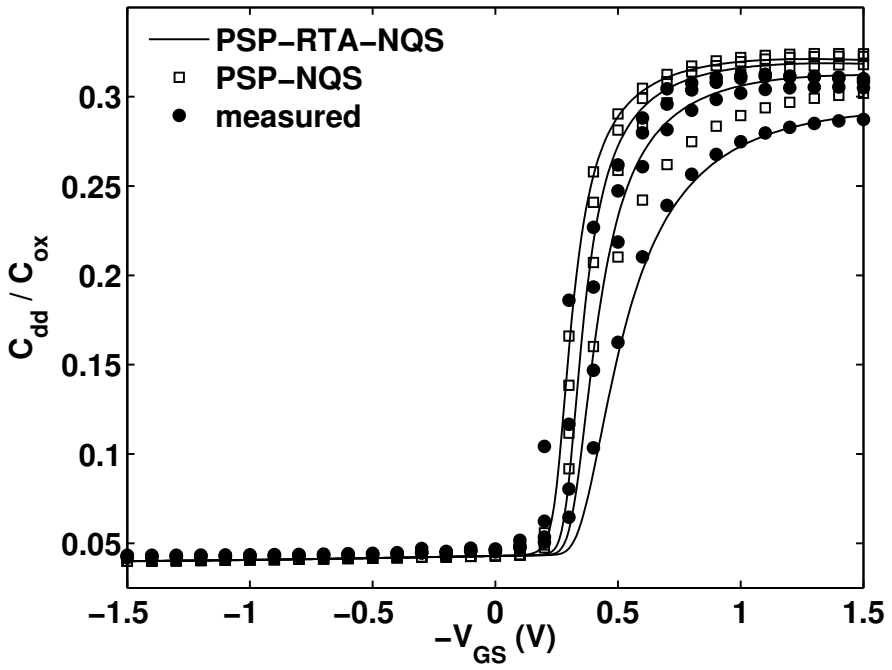

Fig. A.8. Comparison of model and measured data for a PMOS C_{dd} when $V_{\mathrm{DS}} =$ 0 V. Frequencies are 0.1, 0.5, 1 and 2 GHz where $f_{\mathrm{T}} = 0.71$ GHz. $L = 1.2$ μm, W $= 10$ μm.

In the next section, results for $V_{\mathrm{DS}} = -0.3$V are presented.

A.2. $V_{\mathrm{DS}} = -0.3$ V

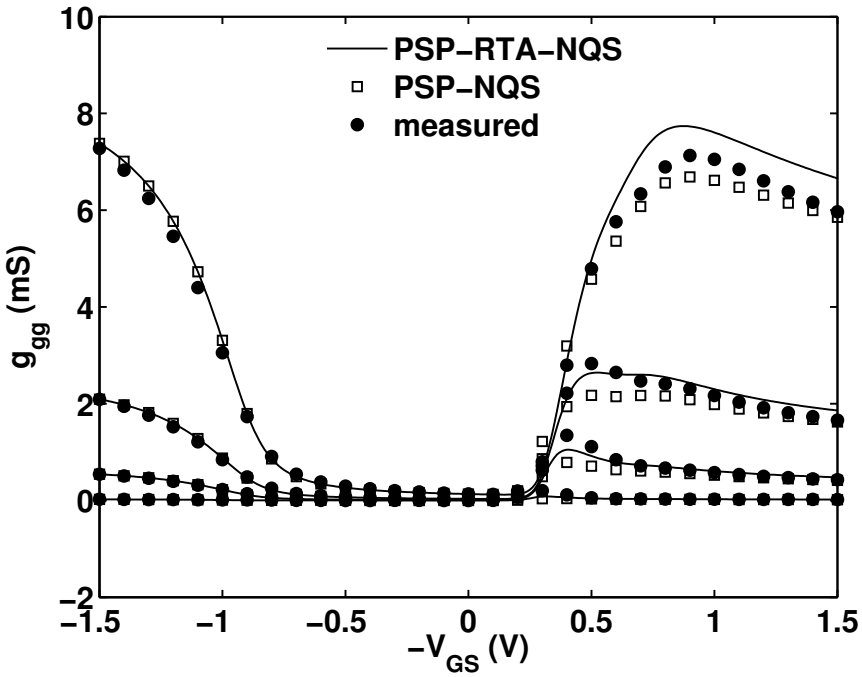

Fig. A.9. Comparison of model and measured data for a PMOS g_{gg} when $V_{\mathrm{DS}} =$ -0.3 V. Frequencies are 0.1, 0.5, 1 and 2 GHz where $f_{\mathrm{T}} = 0.71$ GHz. $L = 1.2$ μm, $W = 10$ μm.

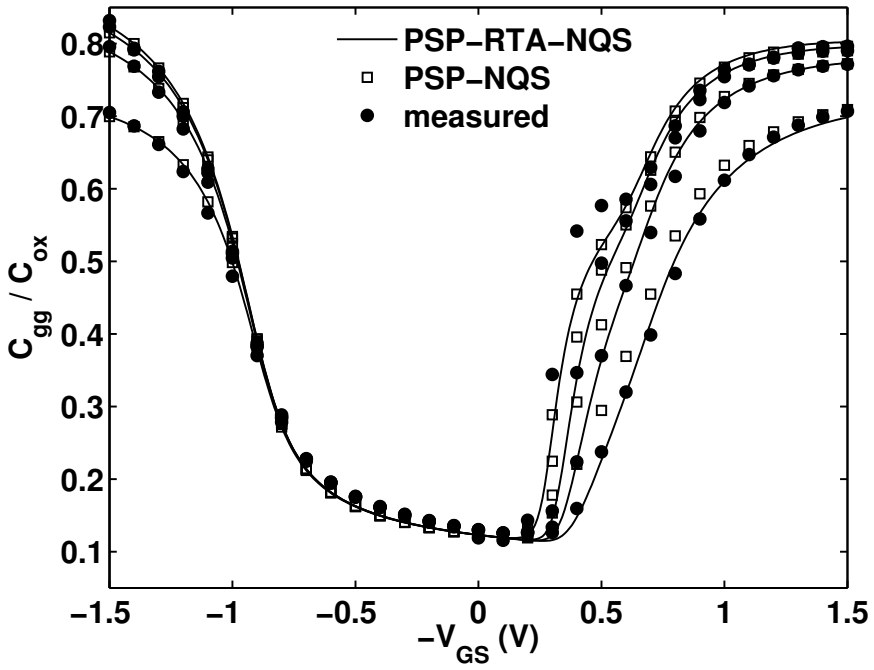

Fig. A.10. Comparison of model and measured data for a PMOS C_{gg} when V_{DS} = -0.3 V. Frequencies are 0.1, 0.5, 1 and 2 GHz where $f_{\mathrm{T}} = 0.71$ GHz. $L = 1.2$ μm, $W = 10$ μm.

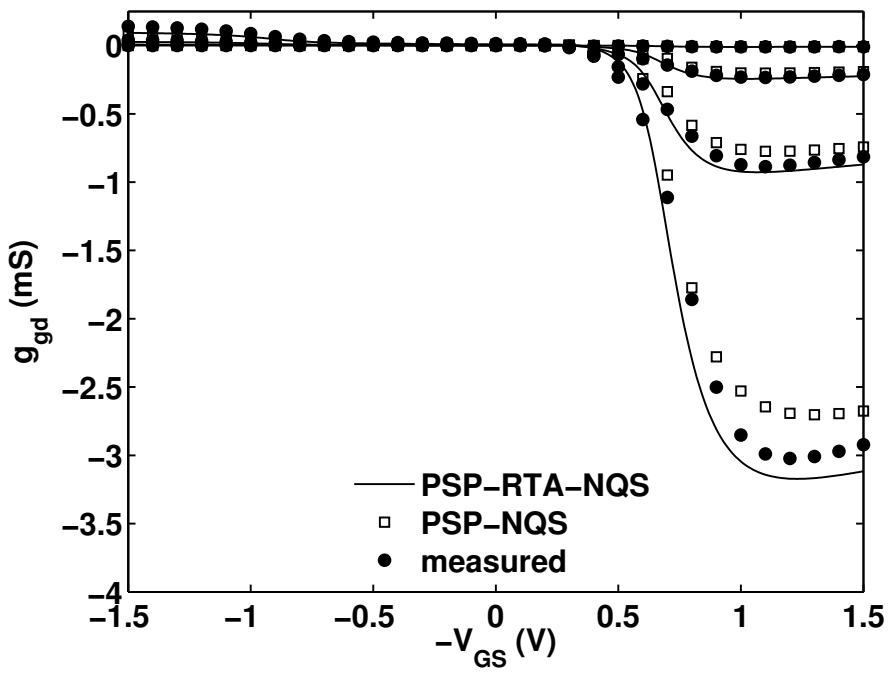

Fig. A.11. Comparison of model and measured data for a PMOS g_{gd} when V_{DS} = -0.3 V. Frequencies are 0.1, 0.5, 1 and 2 GHz where $f_{\mathrm{T}} = 0.71$ GHz. $L = 1.2$ μm, $W = 10$ μm.

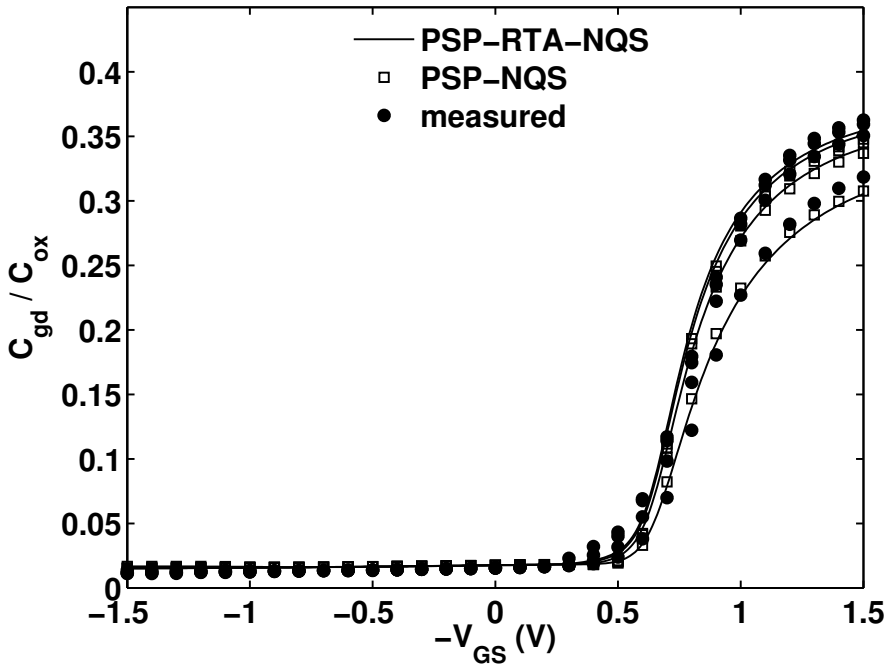

Fig. A.12. Comparison of model and measured data for a PMOS C_{gd} when V_{DS} = -0.3 V. Frequencies are 0.1, 0.5, 1 and 2 GHz where $f_{\mathrm{T}} = 0.71$ GHz. $L = 1.2$ μm, $W = 10$ μm.

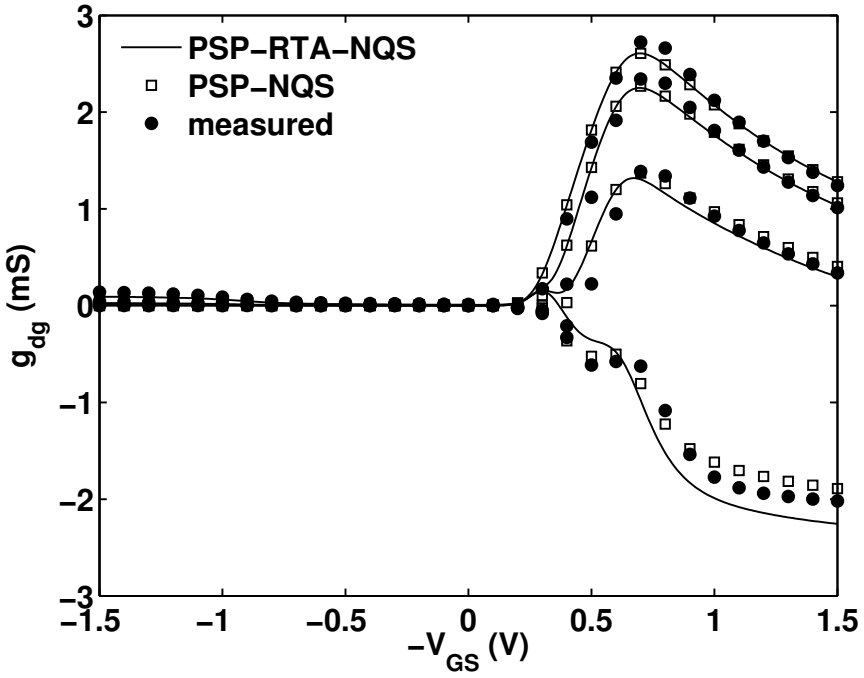

Fig. A.13. Comparison of model and measured data for a PMOS g_{dg} when V_{DS} = -0.3 V. Frequencies are 0.1, 0.5, 1 and 2 GHz where $f_{\mathrm{T}} = 0.71$ GHz. $L = 1.2$ μm, $W = 10$ μm.

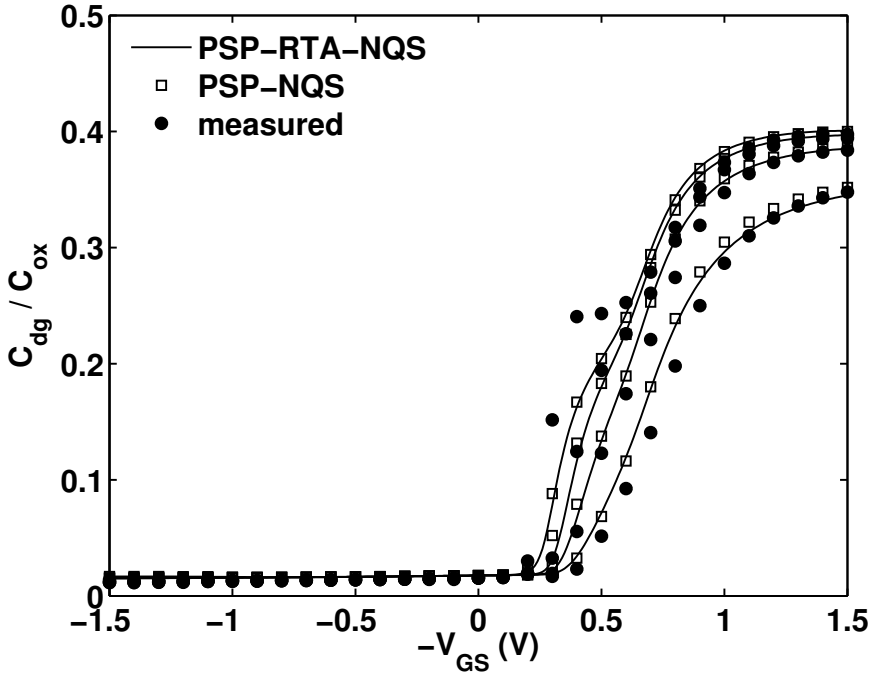

Fig. A.14. Comparison of model and measured data for a PMOS C_{dg} when V_{DS} = -0.3 V. Frequencies are 0.1, 0.5, 1 and 2 GHz where $f_{\mathrm{T}} = 0.71$ GHz. $L = 1.2$ μm, $W = 10$ μm.

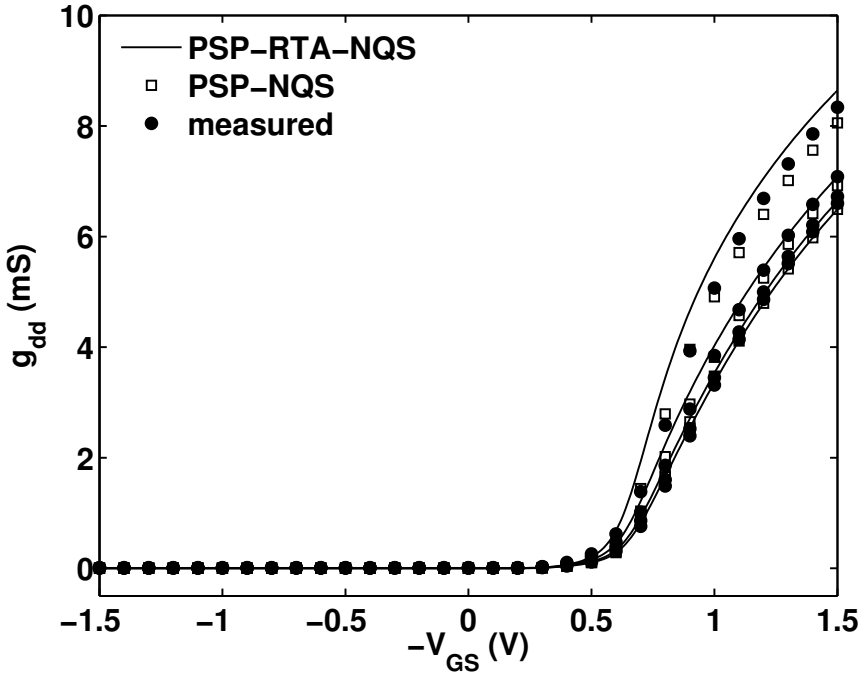

Fig. A.15. Comparison of model and measured data for a PMOS g_{dd} when V_{DS} = -0.3 V. Frequencies are 0.1, 0.5, 1 and 2 GHz where $f_{\mathrm{T}} = 0.71$ GHz. $L = 1.2$ μm, $W = 10$ μm.

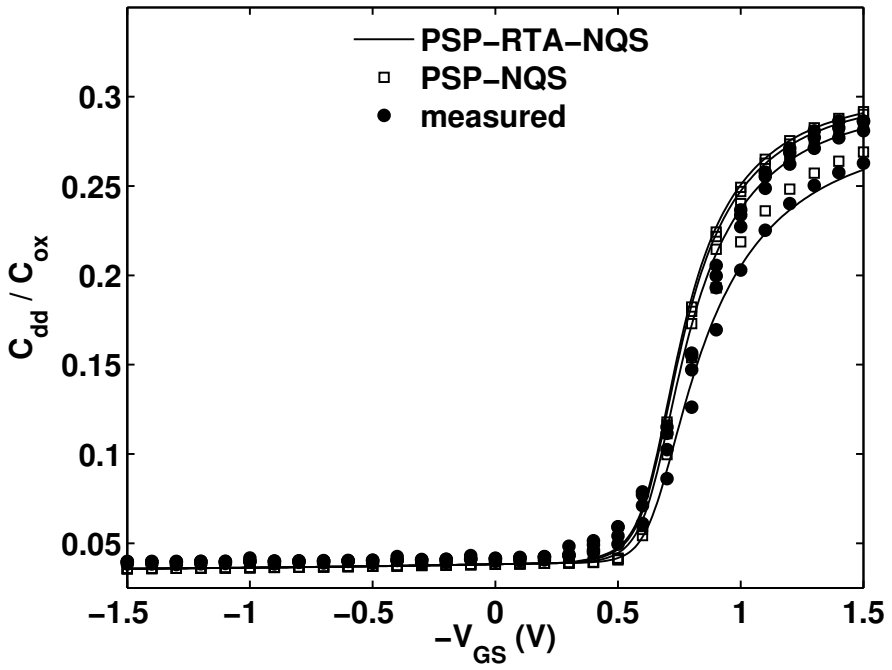

Fig. A.16. Comparison of model and measured data for a PMOS C_{dd} when V_{DS} = -0.3 V. Frequencies are 0.1, 0.5, 1 and 2 GHz where $f_{\mathrm{T}} = 0.71$ GHz. $L = 1.2$ μm, $W = 10$ μm.

BIOGRAPHICAL SKETCH

Zeqin Zhu received the BS degree in physics from University of Science and Technology of China, Heifei, China, in 2002, and the MSEE from University of Houston, Houston, TX in Dec, 2004. He began doctorate study in electrical engineering at Arizona State University, Tempe, Arizona in September, 2005. He started to work with the PSP modeling group since Jan, 2007. He was an intern with TowerJazz, Newport Beach, CA in summer 2007 and 2008, respectively. He was one of the developers of the industry standard varactor model MOSVAR.

Book chapter:

Z. Zhu, G. Gildenblat, J. Victory, and C.C. McAndrew, "Surface-Potential-Based MOS Varactor Model," in Compact Modeling: Principles, Techniques and Applications, G. Gildenblat ed., Springer, 2010.

Journals:

1. Z. Zhu, A. Kathuria, S.G. Krishna, M. Mojarradi, B. Jalali-Farahani, H. Barnaby, W. Wu, and G. Gildenblat, "Design applications of compact MOSFET model for the extended temperature range (60-400K)," Electronics Letters, Vol. 47, No. 2, 2011, pp. 141–142.
2. Z. Zhu, G. Gildenblat, "Symmetrically linearised charge-sheet model for extended temperature range," Electronics Letters, 45 (2009), 346–348.
3. G. Gildenblat, Z. Zhu, C.C. McAndrew, "Surface potential equation for bulk MOSFET," Solid-State Electronics, 53 (2009) 11-13.
4. G. Gildenblat, Z. Zhu, and W. Wu, "Analytical Expression for the Bias and Frequency-Dependant Capacitance of MOS Varactors," IEEE Trans. Electron Devices, Vol. 54, 2007, pp. 3107–3108.

Conferences:

1. Z. Zhu, C. C. McAndrew, I.-S. Lim, and G. Gildenblat, "Parameter Extraction for Relaxation-Time Based Non-Quasi-Static MOSFET Models," 2012 IEEE Conference on Microelectronic Test Structures, accepted.
2. Z. Zhu, G. Gildenblat, C. C. McAndrew, and I.-S. Lim, "Modeling the Frequency Dependence of MOSFET Gate Capacitance," 2011 IEEE Conference on Microelectronic Test Structures, April 4-7, Amsterdam, The Netherlands, pp. 13–18.
3. Z. Zhu, J. Victory, S. Chaudhry, L. Dong, Z. Yan, J. Zheng, W. Wu, X. Li, Q. Zhou, P. Kolev, Z. Yan, C.C. McAndrew, G. Gildenblat, "Improved Parameter Extraction Procedure for PSP-Based MOS Varactor Model ," Proc. IEEE ICMTS, March 2009, pp. 148–153 5.
4. G. Gildenblat, W. Wu, X. Li, Z. Zhu, G.D.J. Smit, A.J. Scholten, D.B.M. Klaassen, "Surface-potential-based MOSFET models with introduction to PSP (invited)," Wireless and Microwave Technology Conference, IEEE 10th Annual, 2009 , pp. 1-2.
5. Q. Zhou, W. Yao, W. Wu, X. Li, Z. Zhu and G. Gildenblat, "Parameter extraction for the PSP MOSFET model by the combination of genetic

and Levenberg-Marquardt algorithms," Proc. IEEE ICMTS, March 2009, pp. 137–142.
6. J. Victory, Z. Zhu, Q. Zhou, W. Wu, G. Gildenblat, Z. Yan, J. Cordovez, C. McAndrew, F. Anderson, J.C.J. Paasschens, R. van Langevelde, P. Kolev, R. Cherne and C. Yao, "PSP-Based Scalable MOS Varactor Model," IEEE 2007 Custom Integrated Circuits Conference, pp. 495–502.